NASA Technical Paper 3598

A Computational and Experimental Study of Nonlinear Aspects of Induced Drag

1996

Stephen C. Smith, *Ames Research Center, Moffett Field, California*

National Aeronautics and Space Administration

Ames Research Center
Moffett Field, California 94035-1000

NASA
Technical
Paper
3598

A Computational and Experimental Study of Nonlinear Aspects of Induced Drag

February 1996

Stephen C. Smith

National Aeronautics and
Space Administration

TABLE OF CONTENTS

LIST OF TABLES

LIST OF FIGURES

NOMENCLATURE

A	axial force
AR	aspect ratio
b	span
c	chord
C_D	wing drag coefficient
C_{D_i}	wing induced drag coefficient
C_{D_o}	wing drag coefficient at zero lift
C_{D_p}	wing viscous drag coefficient
C_d	sectio drag coefficient
C_ℓ	rolling moment coefficient
C_L	wing lift coefficient
C_l	section lift coefficient
C_r	root chord
C_t	tip chord
D'	drag per unit span
D_i	induced drag
D_w	wave drag
dl	infinitesimal length
ds	infinitesimal area
dv	infinitesimal volume
e	inviscid span efficiency, $\frac{C_L^2}{\pi AR C_{D_i}}$
e_o	Oswald's efficiency factor, $C_D = C_{D_o} + \frac{C_L^2}{\pi AR e_o}$
$\mathbf{F}$	force
F	function
$\bar{F}$	mean-value of function F
h	height, perpendicular distance
$\overline{h}$	amplitude of plunging motion
i	streamwise panel index
j	spanwise panel index
k_o	reduced frequency, $\frac{\omega c}{2U_\infty}$
L'	lift per unit span
N	normal force
Nc	number of panels in chordwise direction
Ns	number of panels in spanwise direction
$\hat{\mathbf{n}}$	unit normal vector

$\overline{P}_{AR}(k_o)$	unsteady lift function
$\mathbf{r}$	radius vector
r	radial distance
$\mathbf{P}$	momentum
p	pressure
S	surface
t	time
$\hat{\mathbf{t}}$	unit tangential vector
$\bar{U}$	x-component velocity
u	x-component perturbation velocity
$\mathbf{V}$	velocity
v	y-component perturbation velocity
w	z-component perturbation velocity
X_t	x-coordinate of wingtip
x	streamwise coordinate direction, wind axes
y	spanwise coordinate direction, wind axes
z	vertical coordinate direction, wind axes
α	angle of attack
$\overline{\alpha}$	amplitude of pitching motion
$\mathbf{\Gamma}$	circulation
γ	ratio of specific heats, vorticity
η	span fraction, 2y/b
λ	sweep angle
μ	doublet strength
ν	viscocity
Φ	velocity potential
ϕ	perturbation velocity potential
ρ	density
ρ'	perturbation density

Subscripts

P	partition surface
SP	computed by surface pressure integration
TR	computed by Trefftz-plane integration
x,y,z	component in coordinate direction
1–11	control-volume surfaces
∞	freestream conditions

A COMPUTATIONAL AND EXPERIMENTAL STUDY OF NONLINEAR ASPECTS OF INDUCED DRAG

Stephen C. Smith
Ames Research Center

SUMMARY

Despite the 80-year history of classical wing theory, considerable research in recent years has been directed toward the study of planform and wake effects on induced drag. Nonlinear interactions between the trailing wake and the wing offer the possibility of reducing drag. The nonlinear effect of compressibility on induced drag characteristics, beyond that predicted by the linear Prandtl-Glauert equation may also influence the wing design process. This study deals with the prediction of these nonlinear aspects of induced drag and ways by which they may be exploited. Although the potential benefit is perhaps only a few percent of the drag, this represents a large fuel savings for the world's commercial transport fleet.

Computational methods must be applied carefully to obtain accurate induced drag predictions. Surface pressure integration is too sensitive to modeling details to achieve the required accuracy. Trefftz-plane drag integration is far more reliable, but is very sensitive to the accuracy of the force-free wake model.

The practical use of Trefftz-plane drag integration was extended to transonic flow with the Tranair full-potential code. The induced drag characteristics of a typical transonic transport wing were studied with both Tranair and A502, a high-order linear panel method to investigate changes in spanwise lift distribution and span efficiency beyond those predicted by the Prandtl-Glauert equation.

The true force-free wake shape is dependent on the flow solution, so modeling of the force-free wake becomes a nonlinear problem, even when the flow governing equation is linear. A novel method was developed for computing the force-free wake shape. This hybrid wake-relaxation scheme couples the well-behaved nature of the discrete vortex wake with viscous-core modeling and the high-accuracy velocity prediction of the high-order panel method. The hybrid scheme provided converged wake shapes that allowed accurate Trefftz-plane integration. An unusual split-tip wing concept was studied for exploiting nonlinear wake interaction to reduce induced drag. This design exhibits significant nonlinear interactions between the trailing and bound vortex systems that produced up to 12 percent reduction in induced drag compared to an elliptically loaded wing of the same span and total lift.

The performance of the split-tip wing was also investigated by careful wind tunnel experiments. Induced drag was determined from the force measurements by subtracting an estimate of the viscous drag, and from an analytical drag-decomposition method using wake survey results. The experimental results confirm the computational prediction—the split-tip wing has about 12 percent lower induced drag than the elliptical wing at a lift coefficient of 0.7. This work was originally published as a Ph.D dissertation at Stanford University in June 1995.

1 INTRODUCTION

1.1 Motivation and Objectives

The classical wing theory describing the induced drag of finite wings is almost 80 years old, yet considerable research in recent years has been directed toward the understanding of planform and wake effects on induced drag (refs. 1–7). The "lifting line" model indicates that only the spanwise lift distribution and the "spanwise camber" (a term used by Cone (ref. 8) to describe the shape of nonplanar wings) determine the induced drag. However, more refined aerodynamic models allow for nonlinear effects that offer the possibility of reducing induced drag below the minimum value predicted by the lifting line theory.

Although the potential benefit of exploiting these effects is perhaps only a few percent of the induced drag, this still represents large fuel savings for the world's commercial transport fleet. The Aeronautical Research Council estimated in 1991 that a 1 percent reduction in cruise drag for the U.S. commercial fleet alone would save $100 million annually (ref. 9). Induced drag represents about 40–50 percent of the cruise drag, but it plays a broader role in aircraft performance. About 85 percent of drag at takeoff and initial climb is induced drag. The requirement for safe takeoff and climb following an engine failure often demands higher installed thrust capability and larger wingspan than would be required for a cruise-optimized design. A reduction of induced drag at high lift coefficients would therefore allow a better cruise design, improving the fuel economy by more than simply the reduction in induced drag at cruise.

Traditionally, the barriers to studying these nonlinear effects have been the determination of the correct force-free wake shape and and computation of induced drag with sufficient accuracy to resolve small performance improvements while avoiding numerical artifacts. Many wake relaxation schemes are not robust enough to converge, and are often iterated only three or four times to obtain an approximation to the true wake shape (ref. 10). Pressure integration has been proven a poor method of determining induced drag, exhibiting planform-dependent errors (refs. 4, 5, 11, and 12). Trefftz-plane integration is a suitable method of obtaining the induced drag, but it requires that the wake shape be force-free, or at least drag free. Even small errors in wake shape can influence the drag computed in the Trefftz plane (ref. 7). One of the primary goals of this dissertation is to explore the potential for induced drag savings produced by favorable wake interaction.

Since most commercial air travel occurs at transonic speeds, the influence of compressibility on spanwise lift distribution and induced drag must be included during wing design. The nonlinear effects of compressibility, beyond the effects predicted by the linear Prandtl-Glauert equation, on induced drag, are also studied.

1.2 Historical Background

The concept of induced drag arose from the search for an explanation to D'Alembert's paradox at the beginning of the twentieth century. With the introduction of circulation, Kutta and Joukowski demonstrated that lift force could be generated in an ideal potential flow. But the paradox remained that there was no apparent mechanism within potential flow to explain the drag that was obviously present in physical observations. In 1907, Lanchester described a conceptual model of the finite wing and its consequences that continues to be accepted today (ref. 13). Lanchester recognized that the bound vorticity associated with the wing's lift could not terminate at the wingtip since this would violate Helmholtz's theorem that a vortex cannot begin or end in the flow. He hypothesized a trailing wake vortex extending downstream from the wingtips. His famous drawing, figure 1 illustrates the realization that the circulation is shed from the trailing edge as a distribution of free vorticity. This system of free vorticity produces an induced velocity field that persists in the flow downstream of the wing. Lanchester was the first to observe that the kinetic energy associated with this flowfield represents the work required to produce lift. No such work is required if the wing span is infinite. The kinetic energy added to the wake per unit distance traveled by the finite wing is called induced drag.

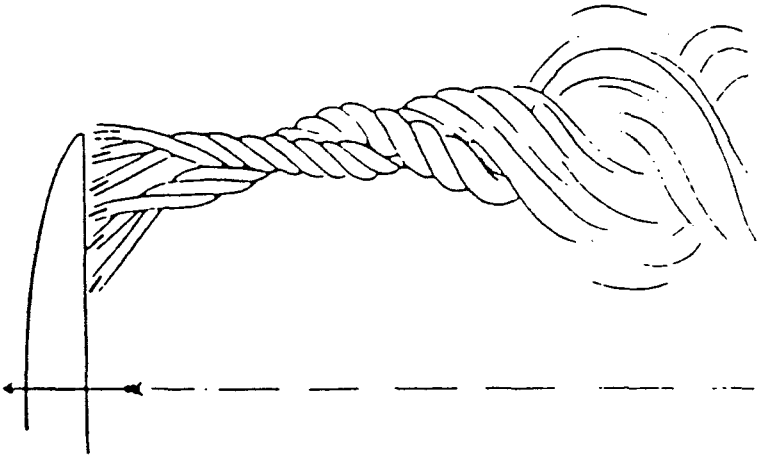

Figure 1. Lanchester's concept of trailing vortex wake.

While Lanchester was the first to propose a conceptual model of the free vortex wake and its role in producing drag, Prandtl assimilated this concept into a complete mathematical model. This "lifting line theory," and its many profound consequences, were published extensively by the early 1920s (refs. 14–16). Although the theory is universally known as "Prandtl's lifting line theory," important contributions were made by several of his students, notably Munk and Betz. Prandtl's lifting line theory represents a finite wing as a concentrated lifting "bound" vortex, with trailing wake vortices extending to infinity in the downstream direction, as shown in figure 2. For a prescribed distribution of

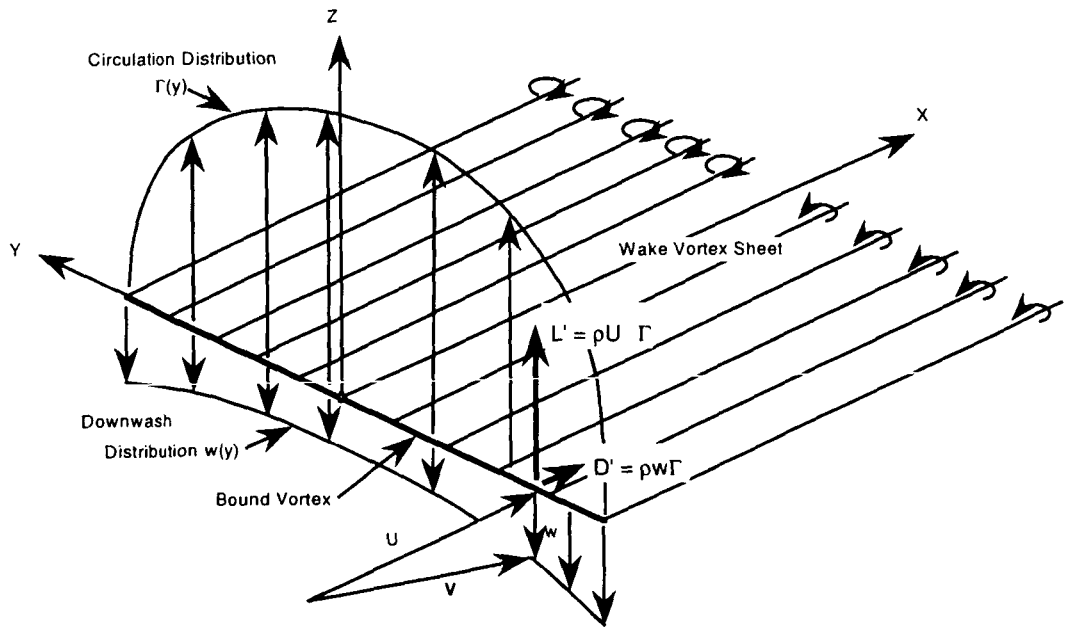

Figure 2. Prandtl's lifting line model.

bound circulation, $\mathbf{\Gamma}(y)$, the local wake vorticity equals the local change in circulation, $\gamma_{wake} = d\mathbf{\Gamma}/dy$. Based on the assumption of potential flow, the downwash velocity induced on the lifting line from each infinitesimal portion of vorticity is computed from the Biot-Savart law:

$$d\mathbf{V} = \frac{d\mathbf{\Gamma} \times \mathbf{r}}{4\pi r^3} \tag{1}$$

where $d\mathbf{\Gamma} = \gamma_{wake} dy$. The total downwash is computed by integration over all the wake vorticity. The same aerodynamic mechanism that produces lift on the wing also produces the induced drag. The Kutta-Joukowski theorem indicates that a force is produced when there is a flow over a bound vortex, given by $\mathbf{F} = \rho \mathbf{V} \times \mathbf{\Gamma}$. The lift and drag distributions along the span are then $L'(y) = \rho V_\infty \Gamma(y)$ and $D_i'(y) = \rho w \Gamma(y)$. Of course, on a real wing, the bound vorticity that produces the lift and induced drag is distributed over the surface within the boundary layer, and the lift and induced drag are the resultants of the surface pressure distribution over the wing.

In Prandtl's inviscid potential flow model, the vortex wake extends to infinity. In a real, viscous flow, the vortex wake eventually breaks down, and the kinetic energy is transferred to heat through viscous dissipation. However, this viscous breakdown takes place so far downstream that the infinite-wake model is useful. Coherent wake vortices are often observed 5–7 miles downstream of commercial aircraft. This corresponds to more than 200 wing spans! The remarkable success of this simple model in predicting the performance of finite wings confirms that the model represents the most relevant flow phenomena. A few of the consequences of the lifting-line theory bear mentioning here.

The most immediate result was that for a planar wing, the minimum induced drag occurs when the downwash distribution along the span is uniform, and is produced by an elliptical distribution

of circulation. This requirement was generalized for nonplanar wings, so that the "normalwash" is proportional to the cosine of the local dihedral angle, $\mathbf{V} \cdot \hat{\mathbf{n}} = w_o \cos\beta$ (ref. 16).

The mutual interference between lifting elements, particularly with longitudinal stagger, was carefully studied. It was shown that the total induced drag of a system of lifting elements is independent of their relative longitudinal positions, as long as the circulation on each element is fixed. Of course, the individual contributions to the total drag are dependent on the stagger, but the interference is reciprocal. Although proven by Prandtl and Munk in different ways, this "stagger theorem" is most easily confirmed by considering the energy left in the wakes of the lifting elements far downstream, already observed to be the source of the induced drag. Trefftz reasoned that far downstream, the influence of the bound vortex would die out, and the wake could be treated as two-dimensional (infinite). He solved a two dimensional potential formulation in a transverse plane far downstream to calculate the lift and induced drag (ref. 17). Only the shape of the wake, and the circulation distribution in the wake, affect the induced drag. Since the projection of the lifting system onto the plane is unaffected by any change in stagger, and the circulation strengths are also unchanged, the velocity distribution in this plane and the drag are unchanged.

The general problem of how to solve for the circulation distribution produced by an arbitrary wing planform was not addressed by Prandtl. In fact, a peculiarity of the circulation distribution was a source of frustration to Prandtl for some time. He found that only certain analytical distributions, of the form $(1-\eta^2)^{\frac{n}{2}}$ in particular, produced finite downwash at the tip. Here η is the spanwise coordinate, $2y/b$, and n is any positive integer. One such distribution was the well known elliptical distribution. Trefftz, and later Glauert, approximated arbitrary distributions with a Fourier series, essentially harmonics of the elliptical distribution (refs. 16 and 18) for an arbitrary circulation distribution. Glauert integrated the induced velocities on the lifting line to find the effective angle of attack. The lift and induced drag distributions from the Kutta-Joukowski law were integrated to obtain the total lift and drag. The wing planform shape and/or twist required to produce a particular lift distribution was inferred by assuming that the flow over any section is nearly two dimensional so the section lift curve slope was known.

Generalization of the lifting line model to nonplanar lifting systems was studied by Cone (ref. 8). He found optimal load distributions for a variety of shapes, including elliptical "spanwise camber," simple dihedral, winglets, and fully closed ring-wings.

All these analyses relied on the circulation being concentrated on the "lifting line." Based on Munk's stagger theorem, this model should be adequate for studies of induced drag. However, the issue of how to build a real wing to produce the desired loading, was not addressed. The most obvious difficulty here is that the downwash on the actual surface varies somewhat from the value computed on the lifting line. This influence is most dramatic near the wingtip, where the three-dimensional flow makes the load distribution depart from that predicted by Glauert's method. Later work by Weissinger and others addressed the problem of loading on a general lifting surface by numerically solving a collocation problem that represents the kinematic boundary conditions on the mean surface

of the wing. This approach has evolved into the discrete vortex-lattice and high-order panel methods in wide use today (ref. 19).

The classical wing theory described to this point requires that the wake shape be prescribed. The streamwise wake model, consisting of straight vortex filaments leaving the trailing edge in the freestream direction, is the most widely used. Prandtl's justification for this model was that although the true force-free wake may be considerably deformed in the far-field, this "roll-up" occurs slowly so that the near-field portions of the wake, which have the most dominant influence, are not significantly altered from their initial shape.

Von Karman developed the far-field approach for determining induced drag from properties in a transverse plane far downstream of the wing (ref. 20). It is interesting to note that this procedure has become known as "Trefftz plane" drag integration, since Trefftz employed the far-field plane in connection with a slightly different problem. Von Karman equated the work expended in overcoming the induced drag to the kinetic energy left behind in the trailing wake. It has become more customary to equate the induced drag to the x-momentum flux through the Trefftz plane (ref. 21). Further developments of the far-field technique for drag determination, particularly for experimental drag decomposition, have been made by Maskell (ref. 22), Wu, Hackett, and Lilley (ref. 23), and Shoemaker (ref. 24).

With the development of this far-field drag computation technique, there was heightened interest in attempting to model the force-free wake shape. While Prandtl's argument was widely accepted (and still is) as adequate for predicting the performance of finite wings, there was still the question of what influence, however small, the force-free wake shape would have. In addition, there were practical issues such as computing the true downwash on the horizontal tail. Betz developed a variety of theorems concerning the motions of systems of infinite vortices (ref. 25). Spreiter applied Betz's rules, with some three-dimensional considerations, to allow an approximation of the three-dimensional rolled-up wake trailing from finite wings (ref. 26). Since then, a variety of computational techniques have been employed for iteratively relaxing the trailing wake to the force-free shape. Representative examples are the unsteady vortex-lattice method of Mittelman (ref. 27) and Quackenbush (ref. 28).

Discrete vortex wake models require a viscous-core model to modify the velocities induced very close to the vortex singularity. Lamb's core model is widely used to prevent erratic behavior of the vortex filaments as they pass near each other (ref. 29). An analogy to the viscous core model applied to distributed vorticity wake models is described by Ramachandran (ref. 30) applied to the finite-difference solution of the full potential equation. This finite-vorticity model has not been implemented into any panel methods. A distributed-vorticity wake relaxation developed by Nagati uses a smoothing function to determine the trajectory of the wake edge, ignoring the extreme velocities produced by the edge singularity (ref. 31). Finally, the vortex-in-cell method of Ribeiro is a recent and novel method to relax the wake shape (ref. 32).

More recent studies of induced drag characteristics of finite wings have been done using the modern lifting surface computational methods. Zimmer concentrated on wingtip treatments while Lowson reevaluated much of Cone's work, both with the goal of exploiting the drag reduction associated with nonplanar wings (refs. 1 and 2).

The relative induced drag of different configurations has been expressed in several ways. One method is to define the span efficiency, e, as the ratio of the induced drag of an elliptically loaded wing to the induced drag of a particular wing with the same span and total lift, $e = C_L^2/\pi AR C_{D_i}$. Based on Munk's result that the elliptically loaded wing achieves the minimum induced drag for a given span, span efficiencies greater than 1.0 are not expected, except for nonplanar wings. However, Munk's result was based on a streamwise wake model. Van Dam raised the possibility of achieving higher span efficiency on planar wings than that predicted by the classical theory (ref. 3). He suggested that nonlinear interaction of the rolled-up wake was responsible for drag savings of about 8 percent on a crescent-shaped wing. It has since been shown that most of Van Dam's apparent drag saving was an artifact of inadequate panel density in the spanwise direction (refs. 4 and 5). A small benefit of the crescent wing over the traditional elliptical wing was associated with a more-nearly elliptical span-load distribution. Although the 8 percent drag savings claimed by Van Dam are unlikely, the possibility remains that nonlinear wake interactions may modify the induced drag somewhat from the value expected from classical theory.

1.3 Present Work

The specific objectives of this Dissertation are to 1) develop and demonstrate techniques for accurate induced drag computation, 2) determine criteria for the necessity and extent of the force-free wake model, 3) design planar wings which exhibit beneficial nonlinear wake interactions, and 4) extend accurate induced drag computation to transonic flow conditions and investigate compressibility effects on optimal span loading. The remaining seven sections of this Dissertation are organized as follows:

Section 2 describes the inviscid governing flow equations used to model and predict induced drag. Computational methods for solving these equations are described, as well as error sources from the discretized computational model.

Section 3 derives the far-field drag computation method, with attention to the influence of wake modeling. The Trefftz-plane contour integral is derived, valid for subsonic and transonic potential flow. The influence of wake shape on far-field drag prediction is included. The minimum requirement on wake shape is that the wake must be drag free. The criteria for when modeling the force-free wake is required is illustrated by introducing a near-field analog to the Trefftz plane.

Section 4 illustrates practical application of computational methods for determining induced drag. For subsonic flow, a high-order panel method is used. Surface-pressure integration is shown to be

strongly dependent on panel density, and drag values do not converge for practical problem size. Trefftz-plane integration is shown to be a reliable method for computing induced drag that is insensitive to panel density and numerical roundoff. For transonic flow, a finite-element full-potential method is used. The influence of Mach number on span efficiency and spanwise lift distribution is investigated for an unswept wing.

Section 5 explores the nonlinear transonic influence of Mach number on the induced drag of a typical transport wing. The influence on span loading predicted by the full-potential equation, over and above the influence predicted by the linear Prandtl-Glauert equation indicates the loss of span efficiency associated with using panel methods to determine optimal wing twist.

Section 6 addresses the task of creating a computational model of the force-free wake. A traditional vortex-lattice wake relaxation scheme created a rolled-up wake with insufficient accuracy for far-field drag computation. A novel hybrid wake-relaxation scheme is developed which combines the greater accuracy of the high-order panel method with the robustness of the discrete-vortex wake model. The technique is applied to two elliptical wing planforms to demonstrate accurate drag computation on force-free wakes.

Section 7 studies two different approaches to exploiting nonlinear wake interactions on planar wings. The first concept involves modeling of wingtip side edge separation to shed a highly nonplanar wake that interacts closely with the wing planform. A small induced drag benefit is achieved when the span loading is optimized, but the interaction with the wake makes this load distribution practically unachievable. The second concept uses a planar "split tip" geometry. This planform also sheds a highly nonplanar wake that interacts closely with the wing surface, but the span loading is controlled independently from the wake interaction. A significant drag reduction is demonstrated for this wing.

Section 8 presents an experimental evaluation of the split-tip planform. The drag savings of the split tip configuration is validated with careful wind tunnel experiments. Induced drag is inferred from the experiments in two ways. The first method subtracts an estimate of the viscous drag from the force-balance measurements. The second method uses a high-resolution wake survey and an analytical drag decomposition process.

Section 9 presents a summary of the key results of this study, conclusions, and suggestions for future work.

2 COMPUTATIONAL METHODS FOR PREDICTION OF INDUCED DRAG

A study of nonlinear aspects of induced drag requires that the induced drag be predicted with high accuracy so that a small drag increment is clearly due to physical effects rather than artifacts of the numerical solutions. Modern panel methods that model the inviscid potential flow over lifting surfaces adequately represent the physical phenomena that create induced drag. For transonic speeds, solutions of the nonlinear full-potential equation are required. Although application of these methods for routine engineering analysis is well established, special care and techniques are required to achieve the high accuracy required to study more detailed aspects of induced drag. The Boeing A502 panel method and the Tranair full-potential code are used to predict induced drag in this study. This section describes the details of these computational methods and specific issues that influence the accuracy of drag prediction.

2.1 Linear Potential Flow—Governing Equations

The lifting-line vortex model developed by Prandtl was motivated by its representation of physical observations, reinforced by the lift-producing mechanism expressed by the Kutta-Joukowski theorem. At the time, potential flow was the only theoretical flow model which could be solved for many problems of practical interest. Because of its close analog in electromagnetics, solution methods for potential flow were well developed, particularly for two dimensional cases. The superposition of vortex elements to represent the wing and wake, and the use of the Biot-Savart law, implicitly represents a solution to the potential-flow governing equation, known as Laplace's equation.

$$\nabla^2\Phi = \frac{\partial^2\Phi}{\partial x^2} + \frac{\partial^2\Phi}{\partial y^2} + \frac{\partial^2\Phi}{\partial z^2} = 0 \tag{2}$$

where

$$\nabla\Phi = \mathbf{V} \tag{3}$$

This equation expresses the conservation of mass for an incompressible, irrotational flow. The extension of the linear potential equation to subsonic compressible flow with small perturbations from the freestream is known as the Prandtl-Glauert equation,

$$(1 - M_\infty^2)\frac{\partial^2\Phi}{\partial x^2} + \frac{\partial^2\Phi}{\partial y^2} + \frac{\partial^2\Phi}{\partial z^2} = 0 \tag{4}$$

Modern methods for solving the Prandtl-Glauert equation still involve superposition of singularities similar to the potential vortex to represent the inviscid flow about wings and bodies. Geometric panels covered with distributed singularities are arranged to represent the surface of the physical geometry. The singularity distributions represented by the panels are solutions to the linear potential equation by construction. The role of viscosity in producing the bound circulation is modeled by imposing the

Kutta condition at the trailing edge, which prevents a nonphysical velocity singularity at the trailing edge. Numerical implementation of this panel method is discussed in section 2.3.

2.2 The High-Order Panel Method—A502

The physical surface geometry of a wing, or a mean-surface approximation or it, can be modeled by a collection of panels which represent distributions of unknown singularities. The singularities are chosen to satisfy the linear potential equation. A linear system of aerodynamic influences (AIC's) is solved to determine the strengths of the singularities. A number of references thoroughly describe the development and numerical implementation of vortex-lattice and panel methods (refs. 19, and 33–38). A panel method is referred to as a high-order method when the singularity distribution varies over the panel according to a polynomial function. A low-order panel method uses a constant strength singularity distribution over each panel. A high-order method is especially desirable for this study, because it eliminates strong velocity singularities on the wing and wake. This makes integration of velocities in the Trefftz plane more accurate, and enables more accurate determination of the force-free wake shape.

The panel method used for computation of induced drag in this study is the Boeing A502 high-order panel code (refs. 37 and 38). The A502 code subdivides each quadrilateral panel into eight triangular sub-panels. Each sub-panel has a bi-quadratic distribution of doublet strength and a bi-linear distribution of source strength. One aerodynamic collocation (control) point is located at the center of each panel, and additional control points are used to match doublet and source strength across sub-panel and panel boundaries.

The A502 code models the flow over surfaces with an implicit Dirichlet form of impermeable surface boundary condition attributed to Morino. Details of the Morino boundary condition is illustrated in figure 3. For this boundary condition, two boundary conditions are required for each aerodynamic collocation point. The source strength is prescribed to locally cancel the component of freestream normal to the surface. The boundary condition for the unknown doublet strengths is chosen to be $\phi = 0$ on the interior of the geometry, where ϕ is the perturbation potential due to all the singularities in the system. By forcing $\phi = 0$ throughout the interior surface, $\partial\phi/\partial\hat{n}$ is implicitly zero. This boundary condition has several computational advantages. This boundary condition does have the drawback that it requires the interior solution domain to be completely isolated from the exterior. Any "leak" in the geometry corrupts the solution. Since the source strengths are known based on the geometry, the order of the linear system is reduced and the source influences are moved to the right-hand side vector. The Kutta condition is enforced by matching the wake doublet strength to the difference of the upper and lower surface doublet strengths at the trailing edge, as shown in figure 3,

$$\mu_{wake} = (\mu_{upper} - \mu_{lower})_{T.E.} \tag{5}$$

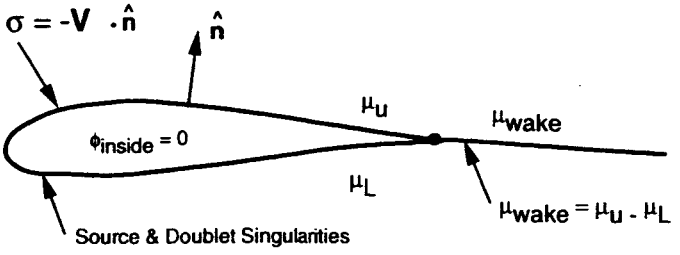

Figure 3. Morino boundary condition and Kutta condition for panel method.

so the doublet strength on the wake panels vary quadratically along the trailing edge where the wake panels abut the wing panels. The doublet strength is constant on the wake panels in the nominal streamwise direction. A second, higher-order condition is also enforced that requires that the doublet gradient on the wing trailing edge in the direction of the wake panels be zero. This forces the vorticity to leave the trailing edge not only in the plane of the wake but also in the direction of the wake panel edges.

To enable panel methods to solve large problems within practical computer time, certain approximations are often made in the computation of the AIC's. Program developers respond to the needs of the engineering community for rapid analysis of complex configurations. The influence of panels "far away" are approximated by the influence of simpler analytical singularities, such as dipoles. The Boeing A502 high-order panel code makes two levels of approximation at mid-field and far-field distances (ref. 38). Boeing program developers established the accuracy criteria used to determine the distances at which these approximations are invoked; they are not accessible as user inputs. Since these distances are nondimensionalized as multiples of the local panel diagonal dimension, a change of panel density on a fixed physical geometry changes the physical distance where the approximation is made. As the panel density is increased, the distance where approximate AIC's are used moves closer to the control points. This unfortunately interferes with the convergence of the solution to a particular geometry as the panel density is increased. The pressure-integrated drag may not converge with increased panel density for a given geometry. Presumably, the predicted difference in drag between two planforms with the same panel distribution would not be affected by this approximation.

2.3 Wake Modeling with Linear Panel Methods

The panel method produces a linear system of equations that can be solved when the wake location is prescribed as part of the geometry. Of course, this places the burden on the user to make an intelligent choice for the wake location. Traditionally, the wake has been placed so that the panel edges project straight downstream, parallel to U_∞. While this choice is usually made because of its simplicity, it also has merit for accurate far-field drag integration, as will be discussed in section 3. Other choices of wake shape may produce well-posed boundary-value problems for the panel method, but may deviate considerably from the desired goal of representing the flow about finite wings. The most realistic

wake model represents the true force-free wake. But this shape is not known a-priori. If the unknown position of the wake is made part of the problem formulation, the problem becomes nonlinear because the wake's aerodynamic influence depends on it's location. A variety of methods have been developed for iteratively computing the equilibrium location of the wake. For panel methods that use an iterative solver, there is little added conceptual complexity to incorporate the wake relaxation directly into the panel method (refs. 35 and 36). For panel methods that use a direct solver, an external relaxation scheme is required that iteratively adjusts the wake location. In either case, the wake position is adjusted to be locally tangent to the flow, based on velocities induced by the collection of singularities representing the wing.

Although the panel method requires the user to prescribe the wake shape, it also has the advantage of conserving the shed vorticity within the wake. The presence of the wake singularity allows evaluation of the perturbation velocities induced by the wake far downstream of the wing. This enables far-field evaluation of the induced drag. The far-field method for computing induced drag will be described in section 3.

2.4 Role of Viscosity in Induced Drag

The continued use of the linear potential equation for study of induced drag, rather than a more complete model of the flow, is based on the observation that the mechanism for producing induced drag is the influence of the trailing wake vorticity on the wing, a fundamentally inviscid mechanism.

Although viscosity is required to produce circulation, the magnitude of the circulation is essentially independent of the coefficient of viscosity as long as the no-slip condition is maintained. The viscous drag on a wing may be lift dependent, since changes in the surface pressure distribution as lift increases lead to changes in the boundary layer. However, this viscous drag is independent from the drag produced by the influence of the trailing wake. One widely-used approximation for the drag characteristics of an aircraft is

$$C_D = C_{D_o} + \frac{C_L^2}{\pi A R e_o} \tag{6}$$

where e_o here is the so-called Oswald's efficiency factor, and C_{D_o} is the drag at zero lift. While the drag at zero lift is primarily viscous, it may contain induced drag due to twist; twist may produce a spanwise distribution of lift that produces induced drag while the net lift is zero. At the same time, Oswald's efficiency factor combines the induced drag and the lift-dependent viscous drag. The value of e_o is usually found by fitting a parabola to the drag polar for the aircraft. Therefore, Oswald's efficiency factor is not strictly a measure of the relative induced drag. In this study, only the inviscid drag produced by the wake is considered induced drag.

There are circumstances where viscosity may influence the induced drag by modifying the spanwise lift distribution. An important example of this might be at the wingtip, where tangential velocities are very high around the side edge of the wingtip. Even with a fully rounded wingtip, at some point

along the side edge, the radius of curvature is small enough that separation is inevitable. The vorticity shed from the side-edge separation forms the initial wake roll-up above the aft corner of the wingtip, carrying the tip vortex inward somewhat compared with an ideal flow where the side-edge flow would stay attached and all the vorticity would shed from the trailing edge. Viscosity has modified the characteristics of the trailing vortex wake, and therefore modified the induced velocities, the bound vorticity, and the surface pressure distribution. The change in drag associated with this separation will be partly pressure drag from the separated-flow region, but also partly a true induced drag, since the trailing vortex field has been modified.

Once it is accepted that there may be viscous influences on induced drag, a case must be remade for using inviscid flow predictions to study induced drag. The traditional argument for this is that on a well-designed wing, there is very little separation. While this is largely true, the wingtip side-edge separation described above may be inevitable. Traditionally, for engineering estimates of wing performance, this effect has been ignored. The induced drag has been predicted based on the assumption that the circulation is entirely shed from the sharp trailing edge. Any influence on the induced drag from the modification of this circulation distribution in a viscous flow is lumped into the lift-dependent viscous drag. Although the nature of this research involves much more detailed study of induced drag than is typical for engineering applications, this viscous effect, whether favorable or adverse, is not directly included. To the extent that this viscous modification of the circulation distribution can be modeled by positioning of a wake sheet based on experimental or other computational observations, its influence can be indirectly included in the inviscid analysis. One example of this that attempts to exploit the side-edge separation to reduce induced drag is presented in section 7.

2.5 Full-Potential Flow—Governing Equations

Modern commercial transports fly at Mach numbers high enough that local acceleration over airfoils produces regions of supersonic flow. These airplanes are carefully designed to minimize the "wave" drag associated with transonic flight, but induced drag is just as important for these aircraft as it is for low speed airplanes. It is desirable to accurately analyze the induced drag of wings under transonic flow conditions that violate the assumptions of the Prandtl-Glauert equation. When shocks are weak enough to be considered isentropic, the velocity field may still be described as the gradient of a scalar potential. The full-potential equation for steady flow, expressed in conservative form, is:

$$\nabla \cdot \rho \nabla \Phi = 0 \tag{7}$$

where the density is given by

$$\rho = \rho_\infty \left[1 + \frac{(\gamma - 1)}{2} M_\infty^2 (1 - \frac{V^2}{V_\infty^2}) \right]^{\frac{1}{(\gamma-1)}} \tag{8}$$

This equation expresses the conservation of mass for an irrotational flow, with no "small perturbation" assumption. The only limitation on the applicability of the full-potential equation is that the flow is

isentropic. This implies that the normal Mach number component upstream of shocks must be less than about 1.3, so that the shocks are weak enough to be approximated as isentropic waves. The expression for the density makes the full-potential equation nonlinear, eliminating the use of solution methods based on superposition.

2.6 Full Potential Flow Solver—Tranair

Traditionally, the full potential equation has been solved by finite difference methods, using body-fitted computational grids. Creation of computational grids for full aircraft configurations has proven very difficult. An alternative solution method that allows arbitrary, complex configurations is embodied by the Boeing Tranair program (refs. 39 and 40). Tranair solves the full-potential equation by a finite element method on a Cartesian grid, as shown in figure 4. Surface boundary conditions are imposed by modifying the finite element basis functions on grid cells which are intersected by boundary surfaces. Tranair includes an automated, solution-adaptive grid refinement scheme that subdivides grid cells, enabling improved resolution of high-gradient regions of the flow such as leading edge regions and shocks. The user specifies the minimum and maximum levels of grid refinement, and may specify specific regions of emphasis for increased grid refinement. The geometry input for Tranair is the same surface panel definition used by the Boeing A502 panel method. A thorough discussion of the theory and implementation of the Tranair program is presented in references 39 and 40. The output features of Tranair used in this study are similar to those of A502.

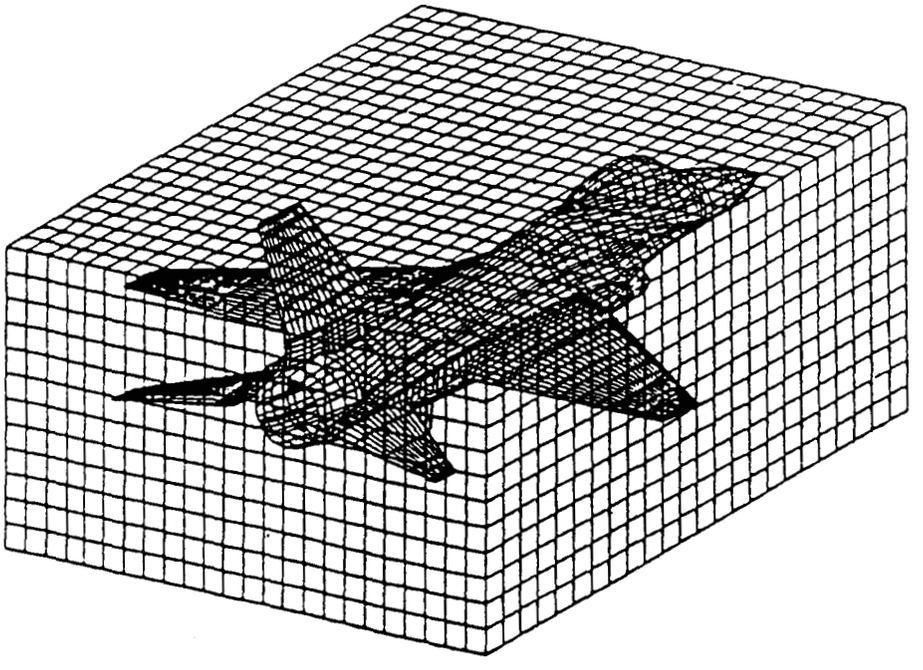

Figure 4. Cartesian grid for Tranair.

Tranair imposes a Kutta condition by forcing a discontinuity in the potential across a wake modeled similarly to the wake in a panel method. Unlike a panel method, the size of the computational box used in Tranair limits the downstream extent of the wake. The boundary conditions imposed on the outer boundary of the computational box include the effect of a semi-infinite wake extending through the downstream boundary.

2.7 Accuracy of Computational Results

Aircraft performance prediction involves estimation of drag and weight from available methods. Engineers may draw on theoretical models such as lifting line theory, experimental data such as flat plate skin friction measurement, and empirical correlations with other similar aircraft to estimate effects of rivets, control surface gaps, antennae (ref. 41). The uncertainty of the overall drag prediction is dominated by the uncertainty in estimating the viscous drag. The customary approach of induced drag prediction, using surface pressure integration of panel-method results with a streamwise wake model, is well established for these purposes. Of course, care must be taken to adequately resolve the surface pressure distribution to obtain meaningful results.

For detailed studies of the relative induced drag of different wings, where a 1–2 percent increment in drag may be considered significant, more careful methods must be used. Of course, the inviscid potential flow model used to study induced drag is hypothetical; there is no way to verify the flow predictions of a potential flow solver in an absolute sense. For example, the wingtip side-edge flow produced by a correct potential flow simulation will not agree with the viscous flow pattern observed in a wind tunnel test. Induced drag cannot be directly measured in the wind tunnel. Techniques exist for separating wind tunnel drag measurements into viscous and induced drag components, as discussed in section 7. Unfortunately, the experimental uncertainty of these methods is rather high. Therefore, the accuracy of a potential flow computation must be inferred from consistency with other results. Three bases for accuracy assessment may be considered.

First, although somewhat subjective, is that the geometry and boundary conditions must represent a realistic model of the particular problem. For the purposes of this research, a panel representation of a wing with a trailing wake is a well-posed potential-flow model that will exhibit the physical phenomenon under study—in this case, induced drag.

Second, the solution must be insensitive to changes in user-input parameters, such as panel density, grid clustering, or convergence tolerance. Unfortunately, computational resources pose practical limits to the degree of panel or grid refinement that can be evaluated. This in turn may establish the limit of expected accuracy.

Third, results should agree with other prediction methods, accounting for differences in underlying assumptions, modeling, or discretization. Check-cases may be sought that have established or accepted

results. In this study, the elliptical wing is used as a reference case since classical theory indicates that a span efficiency very close to 1.0 is expected.

2.8 Surface Pressure Integration

Surface pressure integration is provided as an output feature of the A502 code. The program uses the singularity strengths to determine the velocity at each control point. Pressures are then computed using a second-order approximation of the compressible Bernoulli equation. The pressure distribution over each panel is determined from linear interpolation of the control-point pressures. The pressure distribution is then numerically integrated along streamwise columns of panels and finally over all the panels. The results of the complete pressure integration are provided as force coefficients in the body axis system as well as lift and drag coefficients. The panel-column integrations are used to determine the spanwise distributions of lift and drag.

It is well known that numerical integration of surface pressure is a poor method of drag prediction (refs. 11 and 12). The aft-facing surfaces of the wing have a shallow slope, so that only a small component of the pressure acts in the freestream direction. The forward-facing surfaces have larger slopes, but the pressure distribution has large gradients in the vicinity of the leading edge, making it difficult to accurately resolve the drag component of the pressure distribution. Figure 5 shows results from reference 12, illustrating the effect of leading edge panel density on the resolution of the pressure distribution. To further aggravate the problem, the contributions from the fore- and aft-facing surfaces largely cancel, leaving only a small value of drag, which is vulnerable to numerical error. These errors

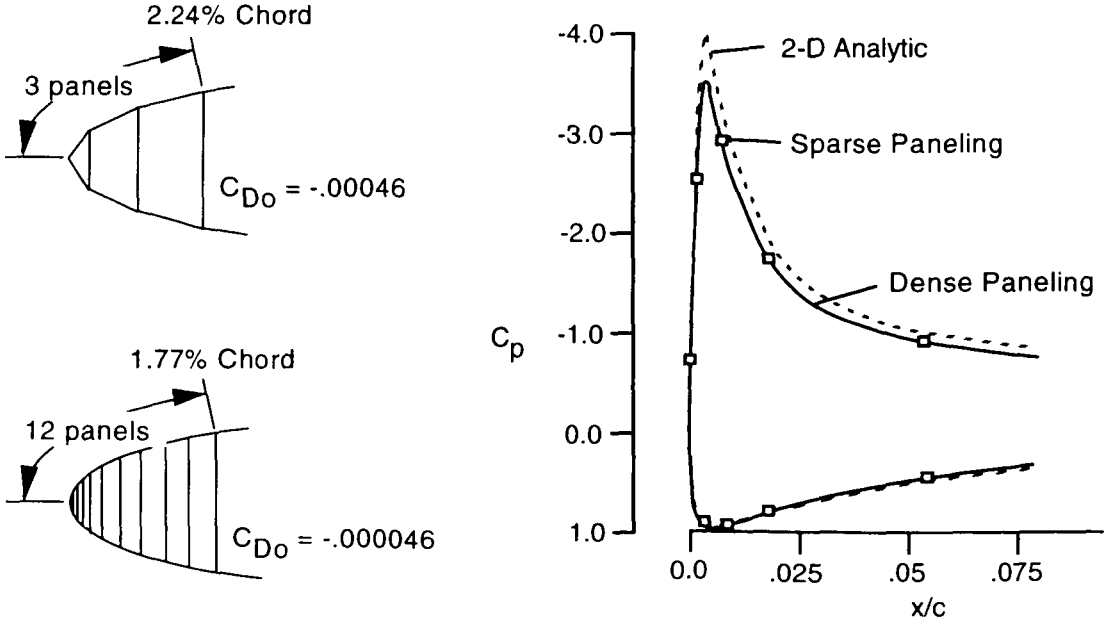

Figure 5. Effect of leading edge panel density on pressure integration.

may vary systematically with wing planform shape, since, for example, local leading-edge sweep causes a reduction in attachment-line pressure and/or a more pronounced suction peak that may not be resolved as well.

There is some temptation to evaluate the pressure-integrated drag at zero lift, where the inviscid drag is exactly zero (for an uncambered, untwisted wing), to form a "drag tare" to be used to adjust pressure-integrated drag results at other angles of attack. While this may be effective in correcting for errors in integrating the thickness-dependent pressure distribution, it cannot correct for the error in resolving the pressure distribution due to angle of attack. The local surface slope and panel density at the location of the suction peak and the stagnation point change with angle of attack, so the "tare" is not representative of the pressure integration error, even at small angles of attack. No adjustment of surface-pressure integrated results are made in this study.

An alternative method for determining induced drag from computational results is the far-field integration method presented in section 3. The application of both these methods for induced drag determination are evaluated for two elliptical wing geometries is presented in section 4.

3 FAR-FIELD DRAG COMPUTATION AND THE INFLUENCE OF WAKE MODELING

Evidence that the accuracy of surface pressure integration is insufficient for a careful study of induced drag indicates that alternate techniques are required. This section develops the far-field method for determining induced drag in the Trefftz plane without restriction to subsonic flow. Care is taken to preserve u-perturbation terms that arise from the force-free wake, often neglected in traditional developments (ref. 21). Wake survey results from computational methods may be numerically integrated to obtain the induced drag. The influence of wake shape on the Trefftz-plane integration is discussed, and a criterion is established for assessing the extent of force-free wake modeling required to capture the interaction of the wake with the wing.

3.1 Far-Field Drag Computation

Von Karman suggested that conservation principles could be applied to a control volume surrounding a finite wing to determine the induced drag, based on the residual flow perturbations exiting the volume in the vicinity of the wake.[1] In the following development, an expression for the induced drag is derived from momentum conservation. The control volume is taken as fixed in the inertial reference frame of the wing, moving at the constant velocity, U_∞ with respect to the undisturbed fluid. The control volume and relevant nomenclature are shown in figure 6. The lateral, top, and bottom surfaces of the volume are aligned parallel to the flight path, and the fore and aft surfaces are aligned perpendicular to the flight path. Additional bounding surfaces are coincident with the wing surface and the upper and lower surfaces of the trailing wake discontinuity. Surface unit-normal vectors are positive outward. For a finite wing, the interior volume is simply connected.

In the absence of any forces, an expression for conservation of momentum in this volume is given by:

$$\frac{D\mathbf{P}}{Dt} = -\frac{d}{dt}\iiint \rho\mathbf{V}\,dv - \iint \rho\mathbf{V}(\mathbf{V}\cdot\hat{\mathbf{n}})\,ds = 0 \tag{9}$$

It is important to note here that the development of this Eulerian expression for momentum conservation requires that the velocity field be continuous. When any forces are present, Newton's second law requires

$$\mathbf{F} = \frac{D\mathbf{P}}{Dt} = -\frac{d}{dt}\iiint \rho\mathbf{V}\,dv - \iint \rho\mathbf{V}(\mathbf{V}\cdot\hat{\mathbf{n}})\,ds \tag{10}$$

[1] In fact, Von Karman's analysis was incorrect. He chose a steady reference frame fixed to the wing. In this frame, there is no work done on the wing, since it doesn't move. The kinetic energy, $E = 1/2\rho\iint(u^2+v^2+w^2)\,ds$ simply balances the work done on the flow by the pressure on the boundaries. Von Karman's result matches the now-accepted expression for the drag only at the point of neglecting the longitudinal perturbation velocity. An energy balance in an unsteady, ground-fixed reference frame does produce an expression for the induced drag, but special care must be taken to correctly account for the unsteady potential terms. Shoemaker showed that this analysis leads to the same result as the more customary momentum balance in the steady reference frame: $D = 1/2\rho\iint(v^2+w^2-u^2)\,ds$ (ref. 24).

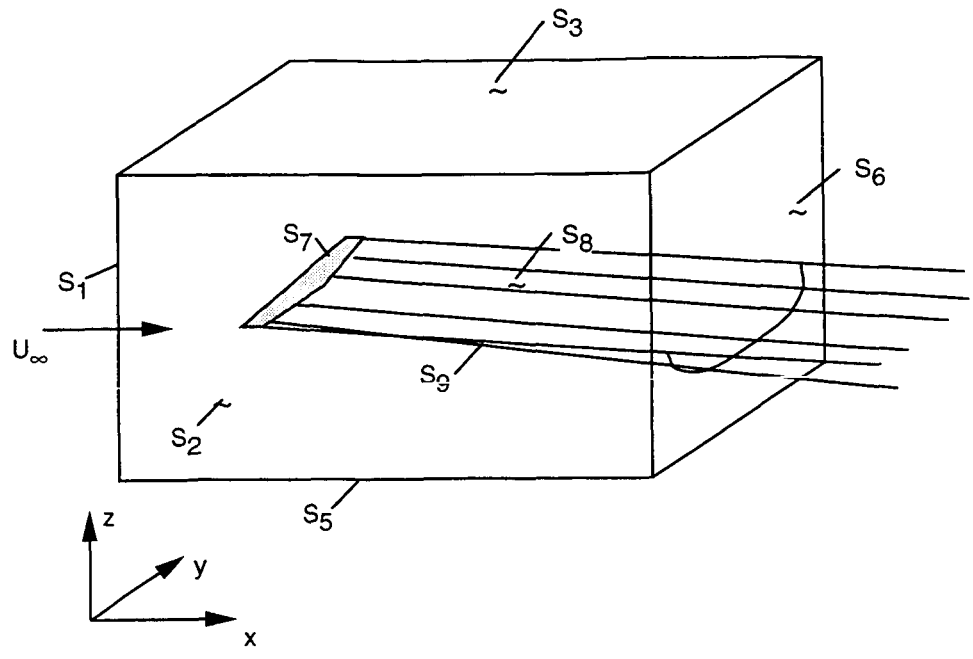

Figure 6. Control volume for momentum conservation.

For stationary flow, there can be no accumulation of momentum within the volume, so

$$\mathbf{F} = -\iint \rho \mathbf{V}(\mathbf{V}\cdot\hat{\mathbf{n}})\,ds \tag{11}$$

For simplicity in this development, body forces are excluded. In addition, the flow is assumed to be inviscid, so surface shear stresses are neglected. The remaining surface force on the boundary is simply the surface integral of the pressure, so

$$\iint p\mathbf{n}\,ds = -\iint \rho \mathbf{V}(\mathbf{V}\cdot\hat{\mathbf{n}})\,ds \tag{12}$$

Since the purpose of this development is to derive an expression for the drag, only the x-component of the force and momentum, parallel to the freestream, will be considered:

$$\iint p n_x\,ds = -\iint \rho V_x(\mathbf{V}\cdot\hat{\mathbf{n}})\,ds \tag{13}$$

The contributions to these surface integrals from the various surfaces of the control volume can now be evaluated separately. The surfaces bounding the wake discontinuity, S_8 and S_9, are considered first. To evaluate these, we must make one of two assumptions about the wake. Either it is a truly force-free wake, aligned everywhere with the local flow, or it is a drag-free wake, aligned with the freestream. In the first case, there is no pressure differential across the wake, and $\mathbf{V}\cdot\hat{\mathbf{n}} = 0$ on the wake surfaces. The unit normals, $\hat{\mathbf{n}}_8$ and $\hat{\mathbf{n}}_9$ have opposite sign, so

$$\iint_8 p n_x\,ds + \iint_9 p n_x\,ds = 0 \quad \text{and} \quad \iint_{8,9} \rho V_x(\mathbf{V}\cdot\hat{\mathbf{n}})\,ds = 0 \tag{14}$$

In the second case, a pressure differential may exist, but $n_x = 0$. There is a tangential velocity (V_y) discontinuity but V_x and V_z are continuous. Again, $\mathbf{n}_8$ and $\mathbf{n}_9$ have opposite sign, so

$$\iint_{8,9} p n_x \, ds = 0 \quad \text{and} \iint_8 \rho V_x (\mathbf{V} \cdot \hat{\mathbf{n}}) \, ds + \iint_9 \rho V_x (\mathbf{V} \cdot \hat{\mathbf{n}}) \, ds = 0 \tag{15}$$

For both of the wake positions considered, the contribution of the wake-bounding surfaces to the x-component momentum balance is zero. Next consider the surface surrounding the wing, S_7. On the wing surface, $\mathbf{V} \cdot \hat{\mathbf{n}} = 0$, and the pressure integral is the drag:

$$\iint_7 p n_x \, ds = D \tag{16}$$

For an inviscid flow that is everywhere subsonic, this drag is defined as the induced drag, D_i. It will be shown that the induced drag is the result of the momentum left in the flow associated with the trailing wake vorticity. The surfaces that remain constitute the six exterior faces of the control volume. Note that $n_x = 0$ on the top, bottom, and side faces, $n_x = -1$ on the front face, and $n_x = 1$ on the rear face. At this point, it is convenient to express the pressure and velocity in terms of perturbations from the freestream, so the drag expression becomes:

$$\begin{aligned} D_i \; + \; & \iint_6 (p - p_\infty) \, ds - \iint_1 (p - p_\infty) \, ds = \\ - \; & \iint_3 \rho (U_\infty + u) w \, ds + \iint_5 \rho (U_\infty + u) w \, ds + \iint_2 \rho (U_\infty + u) v \, ds \\ - \; & \iint_4 \rho (U_\infty + u) v \, ds + \iint_1 \rho (U_\infty + u)^2 \, ds - \iint_6 \rho (U_\infty + u)^2 \, ds \end{aligned} \tag{17}$$

For stationary flow through this volume, mass conservation is expressed by:

$$\iint \rho (\mathbf{V} \cdot \hat{\mathbf{n}}) \, ds = 0 \tag{18}$$

Expressing this in terms of perturbations from the freestream gives:

$$\begin{aligned} \iint_3 \rho w \, ds \; - \; & \iint_5 \rho w \, ds - \iint_2 \rho v \, ds + \iint_4 \rho v \, ds \\ - \; & \iint_1 \rho (U_\infty + u) \, ds + \iint_6 \rho (U_\infty + u) \, ds = 0 \end{aligned} \tag{19}$$

Substitution of this into equation (17) yields:

$$\begin{aligned} D_i \; + \; & \iint_6 (p - p_\infty) \, ds - \iint_1 (p - p_\infty) \, ds = - \iint_3 \rho u w \, ds + \iint_5 \rho u w \, ds \\ + \; & \iint_2 \rho u v \, ds - \iint_4 \rho u v \, ds + \iint_1 \rho u (U_\infty + u) \, ds - \int_6 \rho u (U_\infty + u) \, ds \end{aligned} \tag{20}$$

As the control volume size is increased, the perturbation velocities on the front, top, bottom, and side faces become diminishingly small, leaving:

$$D_i = - \iint_6 (p - p_\infty) \, ds - \iint_6 \rho u (U_\infty + u) \, ds \tag{21}$$

At this point, a relationship between the pressure and velocity on surface S_6 is needed. Rather than restrict this development to incompressible flow, the compressible form of Bernoulli's equation will be used. However, the flow through surface S_6 is regarded as a small perturbation from the freestream, caused only by the induced velocities from the trailing wake. For any subsonic freestream Mach number, the cross-flow perturbations are small compared to the speed of sound. Assuming small perturbations and isentropic flow, a second-order accurate form of Bernoulli's equation is given by:

$$p - p_\infty = -\frac{1}{2}\rho_\infty \left\{ 2uU_\infty + (1 - M_\infty^2)u^2 + v^2 + w^2 \right\} \tag{22}$$

The derivation of this form of Bernoulli's equation is given in the Appendix. Substituting this relation, the drag equation becomes:

$$D_i = \frac{1}{2}\rho_\infty \iint_6 \left\{ 2uU_\infty + (1 - M_\infty^2)u^2 + v^2 + w^2 \right\} ds - \iint_6 \rho u(U_\infty + u)\, ds \tag{23}$$

The density in the second integral may also be expressed as a perturbation from freestream, $\rho = \rho_\infty + \rho'$. Substituting and collecting terms,

$$D_i = \frac{1}{2}\rho_\infty \iint_6 (v^2 + w^2 + u^2)\, ds - U_\infty \iint_6 \rho' u\, ds - \iint_6 \rho' u^2\, ds - \frac{1}{2}\rho_\infty (2 + M_\infty^2) \iint_6 u^2\, ds \tag{24}$$

The derivation of a second-order accurate expression for the perturbation density, ρ', follows the derivation for Bernoulli's equation, producing:

$$\rho' = -\frac{1}{2}\rho_\infty \frac{M_\infty^2}{U_\infty^2} \left\{ 2uU_\infty + \Big(1 - (2 - \gamma)M_\infty^2\Big)u^2 + v^2 + w^2 \right\} \tag{25}$$

Substituting this into equation (24) and collecting terms:

$$D_i = \frac{1}{2}\rho_\infty \iint_6 \left\{ (v^2 + w^2 + u^2) + (M_\infty^2 - 2)u^2 + \frac{M_\infty^2 u}{U_\infty} \Big((\gamma - 2)M_\infty^2 u^2 + v^2 + w^2 \Big) \right\} ds \tag{26}$$

This expression relates the induced drag to the perturbation velocities in a transverse plane defined by the rear face of the control volume. With the assumptions already made (i.e., inviscid, isentropic flow) potential flow exists outside the wake, so that

$$\iint (v^2 + w^2 + u^2)\, ds = \iint \left\{ \left(\frac{\partial \phi}{\partial x}\right)^2 + \left(\frac{\partial \phi}{\partial y}\right)^2 + \left(\frac{\partial \phi}{\partial z}\right)^2 \right\} ds = \iint bf \nabla\phi \cdot \nabla\phi\, ds \tag{27}$$

The vector identity $\nabla\phi \cdot \nabla\phi = \nabla \cdot \phi\nabla\phi - \phi\nabla^2\phi$ may be substituted, noting that $\nabla^2\phi = 0$ outside the wake:

$$\iint (v^2 + w^2 + u^2)\, ds = \iint \nabla \cdot \phi\nabla\phi\, ds \tag{28}$$

Separating the divergence term into cross flow and freestream components,

$$\begin{aligned} \iint \nabla \cdot \phi\nabla\phi\, ds &= \iint \left\{ (\nabla \cdot \phi\nabla\phi)_{yz} + \frac{\partial}{\partial x}\left(\phi \frac{\partial \phi}{\partial x}\right) \right\} ds \\ &= \iint \left\{ (\nabla \cdot \phi\nabla\phi)_{yz} + \phi \frac{\partial u}{\partial x} + u^2 \right\} ds \end{aligned} \tag{29}$$

Gauss' theorem relates the area integral of the two dimensional divergence to a contour integral on the boundary. In this case, the boundary includes a contour surrounding the trace of the wake discontinuity on the surface, S_6. In general,

$$\iint \nabla \cdot \mathbf{F}\, ds = \oint \mathbf{F} \cdot \hat{\mathbf{n}}\, dl \tag{30}$$

so,

$$\iint \nabla \cdot \phi \nabla \phi\, ds = \oint \phi (\nabla \phi \cdot \hat{\mathbf{n}})\, dl = \oint \phi \left(\frac{\partial \phi}{\partial n}\right) dl \tag{31}$$

Substituting these relations into equation (26) gives:

$$\begin{aligned} D_i \;=\; & \frac{1}{2}\rho_\infty \int_{-L}^{L} \Delta\phi \left(\frac{\partial \phi}{\partial n}\right) dl + \frac{1}{2}\rho_\infty \iint_6 \left\{ \phi \frac{\partial u}{\partial x} + (M_\infty^2 - 1)u^2 \right. \\ & \left. + \frac{M_\infty^2 u}{U_\infty}\left((\gamma - 2)M_\infty^2 u^2 + v^2 + w^2\right) \right\} ds \end{aligned} \tag{32}$$

where the contour integral has been replaced by a simple line integral along the wake trace from tip to tip. $\Delta\phi$ is the potential jump from the upper side to the lower side of the wake. Note that although the potential is discontinuous across the wake, the normal velocity, $\frac{\partial \phi}{\partial n}$ is continuous. The remaining surface integral depends only the u-perturbation velocity and its streamwise gradient. When the rear surface of the control volume is moved far downstream of the lifting system, the u-perturbation produced by the bound vorticity becomes diminishingly small, leaving only the perturbations produced by the trailing wake. This surface is traditionally referred to as the Trefftz plane. For the case of the streamwise wake, the wake cannot produce any u-perturbation, and the induced drag becomes simply:

$$D_i = \frac{1}{2}\rho_\infty \int_{-L}^{L} \Delta\phi \left(\frac{\partial \phi}{\partial n}\right) dl \tag{33}$$

For the force-free wake, u-perturbations are produced in the Trefftz plane because the vorticity is not perpendicular to the plane. Where a portion of wake is displaced by an angle $\varepsilon = -w'/U_\infty$, as shown in figure 7, the induced velocity has a u component, related to the w component by $u = w \tan\varepsilon = -ww'/U_\infty$. Here, w' is the induced velocity on the wake and w is the z-component of the velocity induced by the vortex. The u^2 and uw^2 terms in the surface integral are $O(w^4)$, and uv^2

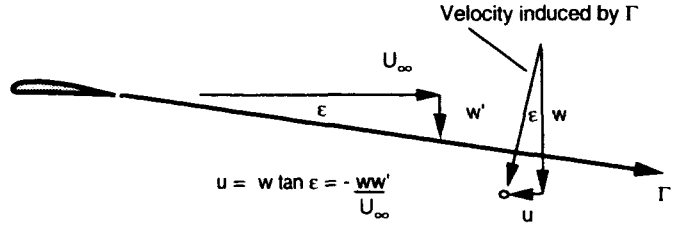

Figure 7. U-perturbation produced when wake is not aligned with freestream.

is $O(v^4)$, whereas the dominant terms of equation (26) are of order $O(w^2 + v^2)$. Traditionally, these higher-order terms are neglected based on the assumptions that the wake deflection is small and the perturbations are small compared with the freestream velocity. The $\frac{\partial u}{\partial x}$ term arises from the curvature and nonparallel nature of the vortices in the deformed wake. However, for typical wings, the wake shape is observed to evolve only slowly, so the $\frac{\partial u}{\partial x}$ term is also traditionally neglected. For this study, induced drag must be computed with sufficient accuracy to resolve small differences in drag due to nonlinear effects. These differences may amount to only 1–2 percent of the drag. In section 6, the magnitudes of these higher-order terms are numerically evaluated for a typical force-free wake to confirm that their contribution is negligibly small. Once this is done, the line integral in equation (33) can be used to evaluate the induced drag on a force-free wake. The Trefftz-plane line integral, equation (33), provides a simple means to evaluate the induced drag in the far-field from computational results. The potential jump and normal velocity may be surveyed and numerically integrated along the wake trace. It is worthwhile to restate the assumptions employed to derive this Trefftz-plane drag integral here:

1. The flow is assumed to be continuous, stationary, and inviscid.

2. The trailing wake is either force-free, or drag-free by virtue of trailing in the freestream direction. This does not imply that the two different wake shapes would produce the same drag, only that the derivation is valid in both cases.

3. The flow is isentropic, perfect gas, and in the vicinity of the wake far away from the wing, may be considered as a small perturbation from the freestream.

4. The force-free wake evolution is slow enough that u-perturbations are assumed to be negligible; the flow can be considered two dimensional in the Trefftz plane.

This derivation puts no explicit limitation on Mach number, although the requirement that the flow be continuous restricts straightforward application to Mach numbers less than 1.0. The appearance of shocks in the flow creates a problem, since they represent discontinuities in potential flow. The jump conditions that exist across the shock discontinuity are dependent on the specific governing equations used to describe the flow. Since the scope of this research involves drag predictions in potential flow, the isentropic shock jump conditions produced by the weak solution of the full potential equation will be considered. The control volume used to express momentum conservation must be modified from the previous development because of the presence of the shocks. As shown in figure 8, additional bounding surfaces, S_{10} and S_{11}, surround the shock. The domain inclosed by the new control volume is still simply connected.

After expanding the control volume large enough to eliminate the contributions on the forward and side faces, the expression for the drag becomes:

$$\begin{aligned} D &= D_i + D_w = -\iint_6 (p - p_\infty)\, ds - \iint_6 \rho u (U_\infty + u)\, ds - \iint_{10} p n_x\, ds \\ &\quad - \iint_{10} \rho (U_\infty + u)(\mathbf{V} \cdot \hat{\mathbf{n}})\, ds - \iint_{11} p n_x\, ds - \iint_{11} \rho (U_\infty + u)(\mathbf{V} \cdot \hat{\mathbf{n}})\, ds \end{aligned} \tag{34}$$

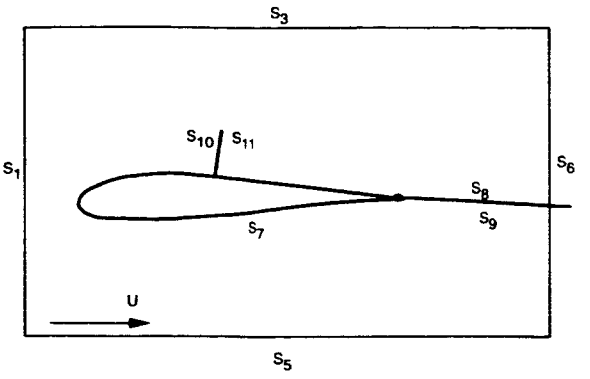

Figure 8. Additional bounding surfaces on shock discontinuity.

where the drag now includes the wave drag. Since surfaces S_{10} and S_{11} are identical except for the direction of the normal, these integrals can be combined so that:

$$\begin{aligned} D_i + D_w &= -\iint_6 (p - p_\infty)\, ds - \iint_6 \rho u (U_\infty + u)\, ds \\ &\quad - \iint_{10} \Big\{ (p_{10} - p_{11}) n_x + \rho u (\mathbf{V} \cdot \hat{\mathbf{n}})_{10} - \rho u_{11} (\mathbf{V}_{11} \cdot \hat{\mathbf{n}}_{10}) \Big\}\, ds \\ &\quad - U_\infty \iint_{10} \Big\{ \rho (\mathbf{V} \cdot \hat{\mathbf{n}})_{10} - \rho (\mathbf{V}_{11} \cdot \hat{\mathbf{n}}_{10}) \Big\}\, ds \end{aligned} \tag{35}$$

The last integral is zero based on mass conservation across the shock. Mass conservation is satisfied by both the isentropic shock and the Rankine-Hugoniot shock jump relations. The drag becomes:

$$\begin{aligned} D_i + D_w &= -\iint_6 (p - p_\infty)\, ds - \iint_6 \rho u (U_\infty + u)\, ds \\ &\quad - \iint_{10} \Big\{ (p_{10} - p_{11}) n_{x10} + \rho u (\mathbf{V} \cdot \hat{\mathbf{n}})_{10} - \rho u_{11} (\mathbf{V}_{11} \cdot \hat{\mathbf{n}}_{10}) \Big\}\, ds \end{aligned} \tag{36}$$

The remaining integral on the shock surface represents the normal-momentum change across the shock. Note that the Rankine-Hugoniot shock relations explicitly conserve the normal-momentum across the shock,

$$(p_{10} - p_{11}) n_{x10} + \rho u_{10} (\mathbf{V} \cdot \hat{\mathbf{n}})_{10} - \rho u_{11} (\mathbf{V}_{11} \cdot \hat{\mathbf{n}}_{10}) = 0 \tag{37}$$

so the integral on the shock surface is zero. This leaves only the Trefftz plane integral on S_6 to capture both the induced drag and the wave drag. In an inviscid, rotational flow, the loss of total pressure across the shock becomes the mechanism for convecting the wave drag downstream to the Trefftz plane. In this case, the shock surface added to the control volume appears unnecessary; no discontinuity in momentum occurs and the same integral relation results in either case.

In the case of potential flow, the isentropic shock jump relations do not conserve the normal-component of momentum, so the integral over the shock surface is finite. On the other hand, the total pressure is constant in the Trefftz plane, equal to the freestream value. Also, in the absence of the wake vorticity in the far field, the perturbation potential in the Trefftz plane must decay to zero; the

Trefftz-plane drag vanishes. Evidently, in potential flow only the induced drag appears in the far-field integral, and the wave drag is in equilibrium with the normal-momentum jump across the shock surface. This assertion has been widely discussed by Steger and Baldwin, Henne and Hicks, van der Vooren and Sloof, among others (refs. 42–44). Further discussion of wave drag is beyond the scope of this study. The expression for the induced drag in transonic potential flow is identical to equation (21), and the remaining development leading to equation (33) is the same.

3.2 Trefftz-Plane Integration of Computational Results

When computational methods such as the A502 panel code or the Tranair full-potential code are used to analyze wings, the induced drag may be determined by the Trefftz-plane integration method developed in section 3.1, provided the required wake properties can be obtained as outputs from the computational method. Both A502 and Tranair provide an off-body flow survey as an output feature. At specified points in the flow off the surface of the geometry, the three components of velocity and the perturbation potential are output. The user may specify that the contribution of some portion of the geometry to these properties be excluded from the survey.

To measure the wake properties needed for Trefftz-plane integration, pairs of survey points are located along the wake a very small distance above and below the wake, shown in figure 9. The survey must be made far enough downstream of the lifting system so that the assumptions leading to equation (33) are valid. The wake model must also be extended a considerable distance downstream of the survey so that the velocities induced are representative of an infinite wake.

For all of the drag calculations in this study, the wake is extended 30 semispans downstream of the trailing edge, and the Trefftz plane survey is located 15 semispans downstream of the trailing edge. The A502 high-order panel code, or the Tranair full-potential code is used to compute the velocity and perturbation potential at these points. The velocity in the wake at a particular station is found by averaging the velocities of the corresponding pair of survey points, and the jump in potential across the wake is found by the difference in potential between the two points. These results are then integrated numerically by the trapezoid rule.

3.3 Influence of Wake Shape on Far-Field Drag Computation

In section 3.1, the far-field integral expression for the induced drag is derived for the cases of a streamwise wake and a force-free wake. The consequence of any other wake shape is that the contribution of the wake-bounding surfaces, S_8 and S_9, to the force computation is nonzero. In other words, the drag (or thrust) on the wake shows up in the far-field integration. A pathological example of this is a wake which folds onto itself in the plane of symmetry, as shown in figure 10. Here, the vorticity on the two halves of the wake cancel and the Trefftz-plane drag is zero. While this shape is rather nonphysical, so is the commonly used streamwise wake.

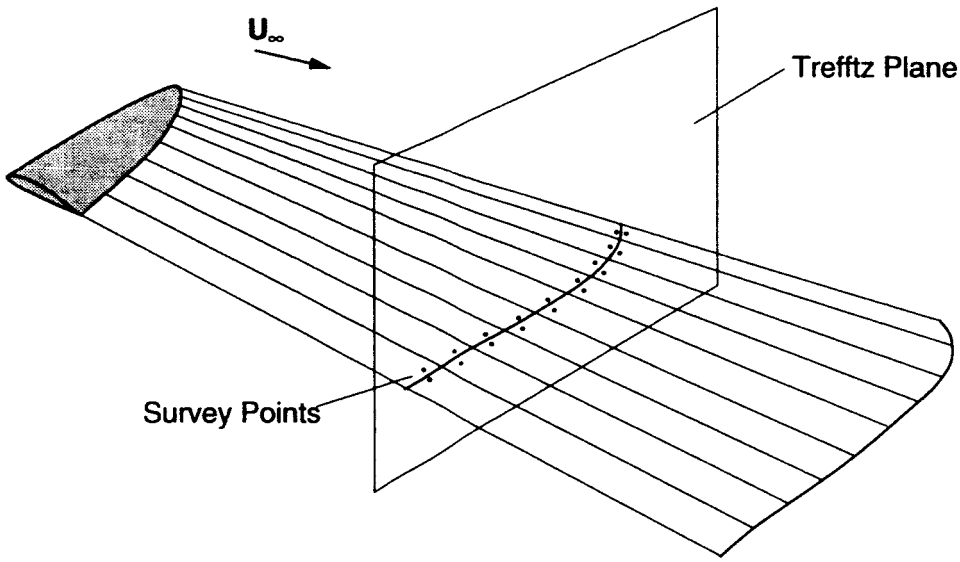

Figure 9. Survey points used to determine wake properties in Trefftz plane.

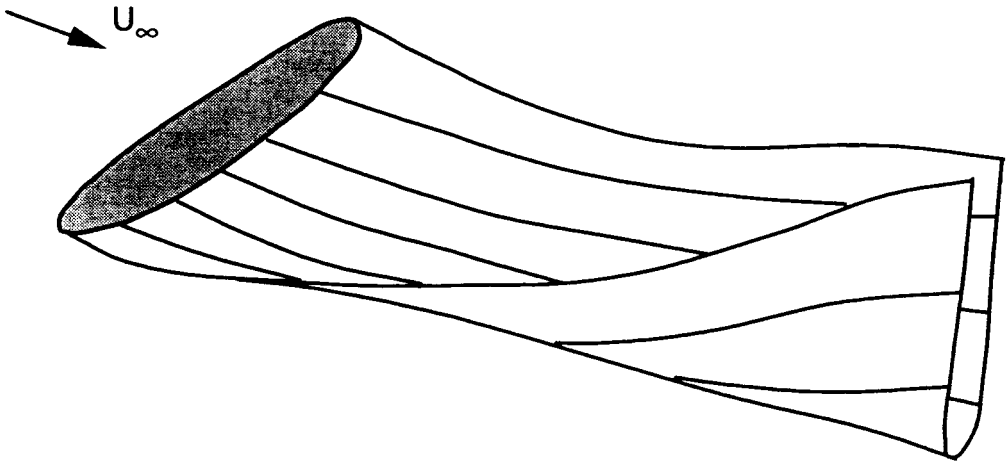

Figure 10. Nonphysical wake shape with zero drag.

It is not sufficient to argue that the wake deforms only slowly, and that the deformation has little effect on the downwash induced on the wing, as may be argued in the case of surface pressure integration. For the force-free wake, there is a small contribution to the drag from u-perturbation velocities produced by the wake, given in equation (32). For simplicity, only the case of low Mach number is considered here. For low speed flows, the u-perturbation contribution is:

$$\frac{1}{2}\rho_\infty \iint_6 \left(\phi \frac{\partial u}{\partial x} - u^2\right) ds \tag{38}$$

As shown in section 3.1, these terms are of $O(w^4)$, and are traditionally neglected in the far field where the contribution from the bound vorticity has died out. The magnitude of these terms for a typical wake are evaluated numerically in section 6. The benefit of neglecting these terms is that the expression for the induced drag reduces to the simple line integral in equation (33), The same expression is exact for the streamwise wake model. However, the question of whether the induced drag computed from the streamwise wake model is the same as the drag computed from a force-free wake model remains. This question actually has two parts. First, if the circulation distribution shed into the wake is fixed, is the Trefftz-plane drag affected by the wake shape, and secondly, is the circulation distribution affected? The first question may be addressed by introducing a partition surface into the control volume, in between the wing and the Trefftz plane. This partition is illustrated in figure 11. The arrangement of the control volumes resulting from this partition is shown in figure 12. The forward, side, top, and bottom faces of the near-field control volume are still moved far away, so the induced drag within the near-field volume may be evaluated by a surface integral on the partition using equation (26) simplified here for low Mach number:

$$D_i = \frac{1}{2}\rho_\infty \iint_P \left(v^2 + w^2 - u^2\right) ds \tag{39}$$

where the subscript P denotes the partition surface. Note that this integral is not restricted by the far-field assumption that the influence of the wing has died out. The induced drag within the entire far-field control volume is still given by equation (32). Provided that the wake is drag-free, the induced drag within the wake control volume is zero. It follows that the two drag computations must agree. Now, the portion of the force-free wake downstream of the partition may be replaced with a drag-free wake constructed as a freestream projection of the trace of the wake on the intermediate partition. The drag computed on the two planes will still agree. Of course, this does not preclude that both results may change. The wake substitution changes the perturbation velocities induced on the partition surface by the wake by changing the deflection angle of half the wake with respect to the partition. This removes approximately half the u-perturbation. Perhaps more important, the wake substitution also increases the effective distance between a vortex filament and a point in the plane, reducing the induced v and w perturbations, as shown in figure 13. If a wake filament has little or no curvature, the reduction of induced velocity is proportional to the cosine of the deflection angle. However, if the vortex curvature is significant, the modification of the induced velocity field in the partition may be more pronounced. As mentioned before, the wake deforms slowly for typical wings, so these effects are expected to be small.

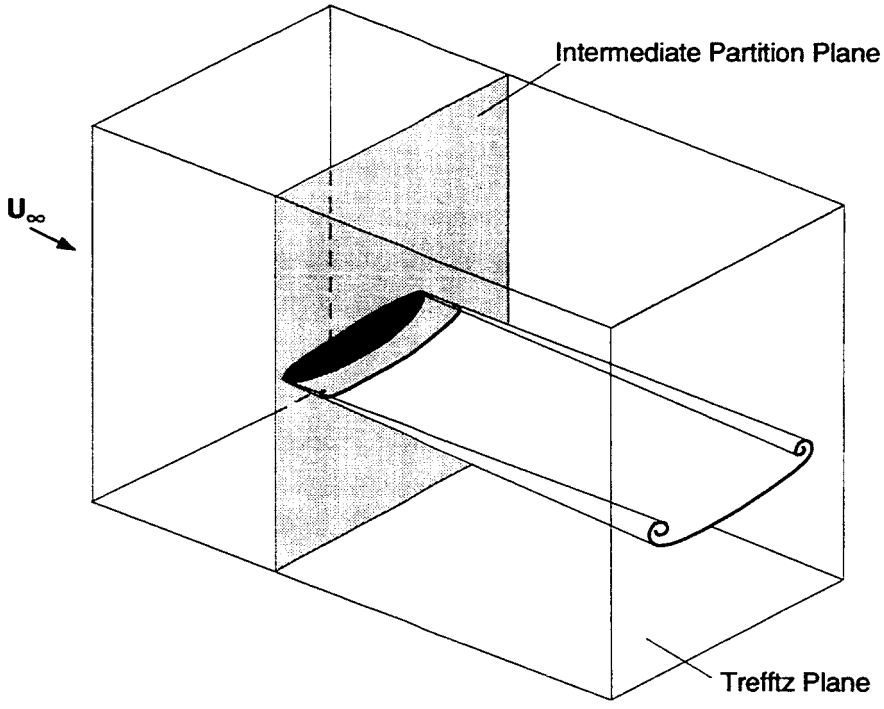

Figure 11. Intermediate partition in control volume.

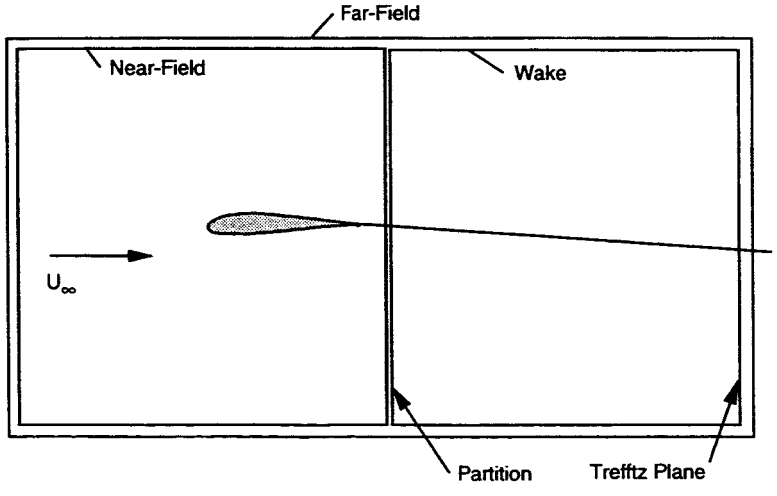

Figure 12. Near-field and wake control volumes.

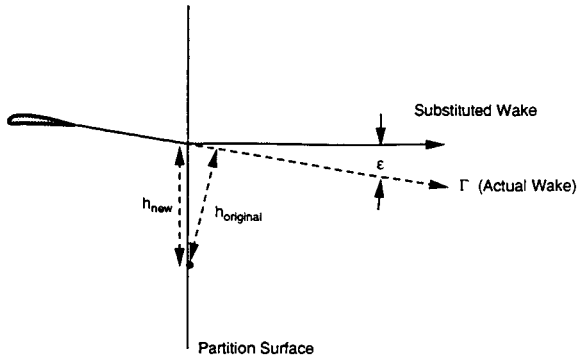

Figure 13. Wake substitution modifies induced velocities.

This allows substitution of a streamwise wake downstream of the partition with only small error. The need for high-accuracy drag prediction for this study requires that the magnitude of these effects be quantified. In section 6, the change in drag computed in the Trefftz plane produced by streamwise wake substitution is investigated numerically for two typical planar wings. Those results confirm that the error is negligible, even for the requirements of this study. For typical wing planforms, the deflection angle and curvature of the individual vortex filaments do not vary significantly along the length of the wake, so these small errors do not increase with proximity of the substitution point to the lifting system. The additional u-perturbation induced by the bound vorticity on the wing is not affected by the wake substitution. Therefore, the streamwise wake substitution may be made immediately downstream of the lifting system, as long as the above assumptions are valid. There may be cases where the wake deforms rapidly for a short distance downstream of the wing. In these cases, the high wake curvature may introduce some error, and the wake substitution should be delayed for a short distance downstream. As the partition where the streamwise wake substitution is made is brought close to the downstream extremity of the lifting system, most of the force-free wake and its influence on the wing planform is removed. In the special case of a wing with an unswept trailing edge, all of the wake may be replaced. In other cases, a small portion of force-free wake remains, as shown in figure 14. At this point, one may be tempted to extend the process of wake substitution further by arguing that the intermediate partition need not be perpendicular to the freestream. In particular, it might be arranged to match the trailing edge sweep of the wing, allowing more of the force-free wake to be eliminated. The full application of this argument, after all, leads to the traditional streamwise wake model where all of the force-free wake is substituted. However, when this is done, the changes in perturbation velocities induced on the partition surface are no longer negligible. Equation (39) must be re-cast to account for the orientation of the partition. In the following example, the partition is rotated by an angle λ about the z-axis. Since the purpose of the rotation is to match a trailing edge sweep angle, λ is not considered small. The revised expression for the induced drag on P is:

$$D_i = \frac{1}{2}\rho_\infty \iint_p \left(v^2 + w^2 - u^2\right) \cos\lambda \, ds + \rho_\infty \iint_p uv \sin\lambda \, ds \tag{40}$$

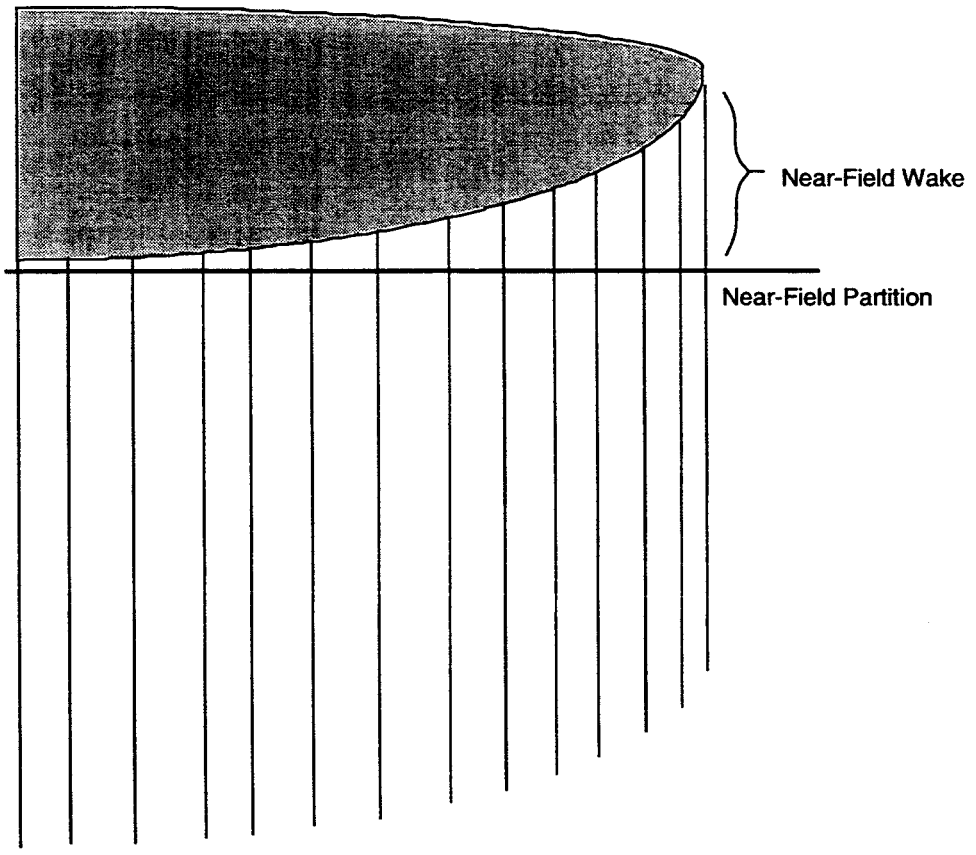

Figure 14. Near-field portion of force-free wake remains after substitution.

For a two dimensional (infinite) wake, the second integral is zero since the u-perturbation contributed by each individual vortex filament is an odd function of y centered about the filament, and the v-perturbation is an odd function of z centered about the filament. By superposition, this term would integrate to zero. However, because the wake is not two dimensional and the surface is swept, the distributions of u and v on the partition surface induced by each filament are not symmetrical. This becomes more pronounced as the surface is moved to proximity with the wing trailing edge, where the wake appears semi-infinite. Further, although u^2 is $O(w^4)$ as before, the uv term is $O(w^3)$. When the substitution of the streamwise wake is made, approximately half the contribution of the uv-perturbation is removed. Even for a modest sweep angle λ, this error is greater than the error produced by the more restrictive case where the partition is perpendicular to the freestream. Planforms with forward sweep in the trailing edge such as shown in figure 14 result in strong wake vorticity being shed well ahead of the partition. Based on the preceding discussion, the replacement of the initial roll-up region of the wake with a streamwise wake cannot be performed without substantially influencing the Trefftz-plane drag. The presence of this remaining portion of force-free wake represents the potential for wake interactions that would be overlooked by the traditional engineering approach. This wake interaction is discussed further in the following section. There is still the remaining question of whether the wake substitution modifies the distribution of bound circulation on the wing. Evidence suggests that the presence of the force-free near wake does modify the circulation distribution slightly from the solution with the classical streamwise wake (ref. 7). In any case, the numerical examples in section 6 quantify the errors resulting from wake substitution, including the effect of any change in circulation distribution.

3.4 Nonlinear Considerations in the Application of Munk's Stagger Theorem

Munk's stagger theorem (ref. 16), that the induced drag of a lifting system is determined only by the wake shape and the vorticity distribution in the wake, follows from the derivation of section 3.1. However, this derivation required that the wake must be either the true force-free shape, or a drag-free streamwise wake. Munk's condition for minimum induced drag for nonplanar wakes is that the "normalwash" in the Trefftz plane is proportional to the cosine of the local dihedral angle.

$$\mathbf{V} \cdot \hat{\mathbf{n}} = w_o \cos\beta \tag{41}$$

Attempting to minimize drag by applying this condition on the force-free wake would be difficult, since it would be practically impossible to design the wing that would produce a specific wake shape and vorticity distribution. However, minimizing drag of wings with streamwise wakes has been done extensively by Cone (ref. 8), Lowson (ref. 2), and others. Burkett and Lowson observed that the wake shape is altered by a coupling between the longitudinal arrangement of vortex elements on the wing and the angle of attack (refs. 45 and 2). Since all the vorticity sheds from the trailing edge, the projection of the trailing edge onto the Trefftz plane determines the wake shape. The often-stated consequence

of the stagger theorem, that the longitudinal arrangement of vortex elements does not affect the drag, must be reconsidered. A planar wing may create a nonplanar wake, as shown in figure 15.

This influence of the trailing edge shape on the wake shape is still within the linear theory. The conclusions of section 3.2 suggest additional, nonlinear influence of the longitudinal stagger (planform shape) on the wake shape. The streamwise wake substitution can only extend to the point where the partition intersects the downstream extremity of the lifting system. In essence, it is the shape of the force-free wake at this near-field partition that influences the far-field drag. Planforms with a significant portion of force-free wake remaining between the trailing edge and the partition have the greatest potential for favorable wake interference by creating a highly nonplanar wake. Two planar wing designs which attempt to exploit the benefit of a nonplanar wake are studied in section 7.

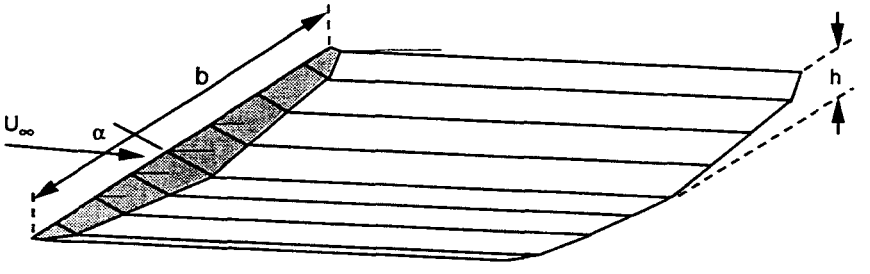

Figure 15. Planar wing producing a nonplanar wake.

4 APPLICATIONS OF COMPUTATIONAL METHODS FOR INDUCED DRAG PREDICTION

In this section, two wing planforms are analyzed with the computational methods described in the two preceding sections to assess the accuracy of induced drag predictions using surface pressure integration and Trefftz-plane integration. The sensitivity of induced drag predictions to modeling details such as surface panel density and flowfield grid density are studied to establish the level of expected accuracy for induced drag prediction.

4.1 Subsonic Induced Drag Computation

Two wing planforms with elliptical chord distributions were analyzed with the A502 high-order panel code to assess the accuracy of induced drag predictions using surface pressure integration and Trefftz-plane integration. The two wings, shown in figure 16, are distinguished by the x-coordinate of the wingtip. The traditional elliptical wing has an unswept 25 percent chord line so the x-coordinate of the tip, normalized by the root chord is $X_t = 0.25$. The other wing has an unswept trailing edge so the x-coordinate of the tip is $X_t = 1.00$.

The motivation for selection of these particular wings came from earlier studies by Van Dam (ref. 3). He used the low-order panel method VSAERO (ref. 35) to evaluate a family of elliptical wings with increasing values of X_t, as shown in figure 17. Each of these wings had $AR = 7.0$ and were lofted with untwisted NACA 0012 sections. These wings were modeled with 1000 surface panels, using 50 chordwise panels (Nc = 50) and 10 spanwise panels (Ns = 10) on the upper and lower surface. The panel spacing was chosen by a cosine function from leading edge to trailing edge, and a half-cosine function from root to tip. The iterative wake relaxation feature built into VSAERO was used to model the trailing wake shape.

Van Dam used surface-pressure integration to compute the induced drag of this family of wings. The wings were analyzed at 4 deg angle of attack, producing a lift coefficient of about 0.34, representative of cruise conditions. The span efficiencies predicted by Van Dam for this family of wings is shown in figure 18. His results indicated a surprising reduction in induced drag as the tip was sheared back, with a savings of 8 percent reported for the $X_t = 1.5$ "crescent-moon shaped wing." Van Dam attributed the drag benefit to the favorable interaction of the rolled-up wake on the wing planform. These results caused both intense interest and healthy skepticism throughout the aeronautical research community, indicated by papers from Burkett, Smith and Kroo, and DeHaan (refs. 45, and 4–6). Although a small benefit from wake interaction seems plausible for this planform, an 8 percent savings would be surprising.

For this study, the $X_t = 0.25$ and 1.00 wings were analyzed with the A502 high-order panel method. The panel spacing in the chordwise direction was defined by a $(\text{half} - \text{cosine})^{1.25}$ function from the leading edge to the maximum thickness point at 30 percent chord, and uniform spacing from 30 percent

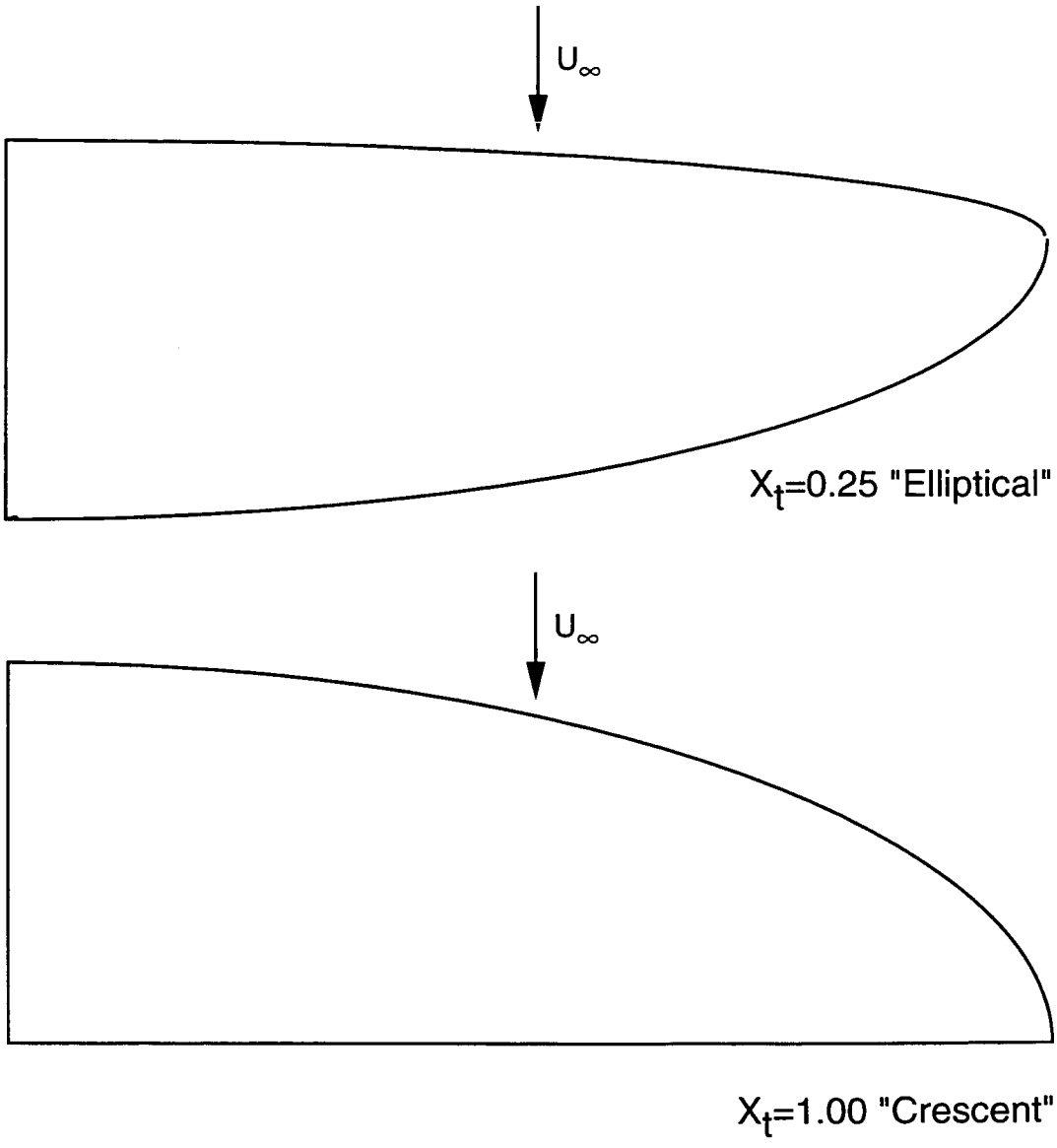

Figure 16. Two elliptical wing planforms.

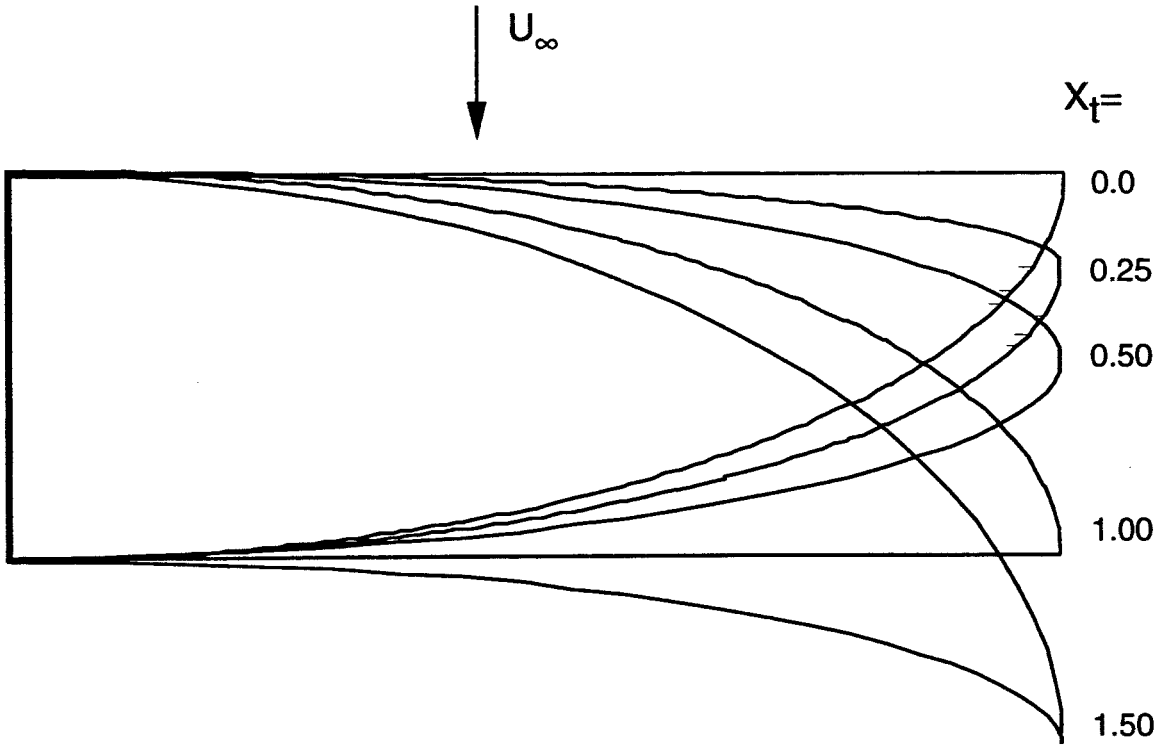

Figure 17. Family of wings studied by Van Dam (ref. 3).

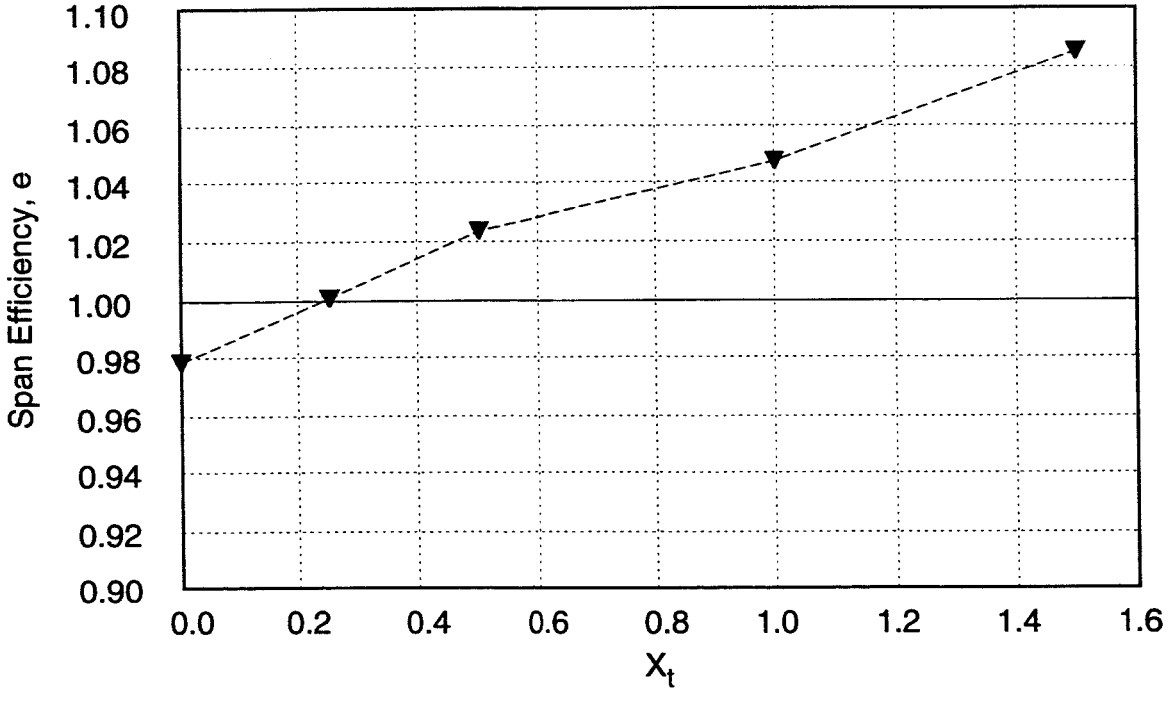

Figure 18. Span Efficiency versus X_t predicted by Van Dam (ref. 3).

chord to the trailing edge with some additional panels added near the trailing edge. The width of the last panel at the trailing edge was 0.25 percent of the local chord, insuring that the Kutta condition was imposed at a control point very near the physical trailing edge. This distribution produces somewhat higher panel density near the leading edge than cosine spacing. The spanwise panel spacing was defined by a $(\text{half} - \text{cosine})^{0.85}$ function, which concentrated more panels near the wingtip than a cosine distribution. These panel spacings seem to provide the most satisfactory resolution of the pressure distribution over the wing. The wing tip was cropped at a span-fraction of 0.9995 and closed with additional panels. Figure 19 shows a typical panel arrangement on the $X_t = 0.25$ elliptical wing, with 1000 panels (Nc $\times$ Ns = 50 $\times$ 10 on the upper and lower surfaces), and a detail of the paneling of the extreme tip. For convenience, the $X_t = 1.00$ wing will be referred to as a crescent wing, although it lacks the extreme sweep of the $X_t = 1.50$ wing studied by Van Dam.

The trailing wake was modeled as a straight freestream extension of the trailing edge for both wings. Note that for the crescent wing with straight trailing edge, this leads to a planar wake. For the classic elliptical wing at nonzero angle of attack, the wake is not flat; the trace of the wake in the Trefftz plane is curved.

4.2 Sensitivity to Paneling—Surface Pressure Integration

The sensitivity of induced drag calculated by surface-pressure integration to variations in surface panel density was investigated by analyzing both wing geometries with a range of panel densities. The span efficiency for each case was determined from the lift and drag coefficients computed by A502. The surface-pressure integration within the A502 code assumes a linear pressure distribution over each sub-panel, consistent with the quadratic distribution of doublet singularities (ref. 37). The variation of span efficiency for the crescent and elliptical wings with spanwise panel refinement is shown in figure 20.

For Ns =10, the predicted span efficiencies for the elliptical and crescent wings are 0.982 and 1.042, respectively. These results agree closely with Van Dam's results of 1.00 and 1.047 with the same spanwise panel density, even though the panel distribution is somewhat different.

Initial studies focused on refining both the chordwise and spanwise paneling, but found that 70–80 chordwise panels on each surface is adequate. This is evident from two cases with the same spanwise panel density. As shown on figure 20, panelings of Nc $\times$ Ns = 72 $\times$ 36 and 86 $\times$ 36 for the crescent wing resulted in virtually identical computed span efficiency. Spanwise panel density had a strong effect on the pressure-integrated span efficiency, especially for the crescent wing. The span efficiency predicted for the crescent wing decreased almost 7 percent as Ns is increased from 10 to 69. For the same panel refinement, the elliptical wing span efficiency decreased almost 3 percent. As the spanwise panel density was increased, the predicted drag difference between the two planforms decreased from 6 percent to 1.8 percent. The computed span efficiency for both wings continued to

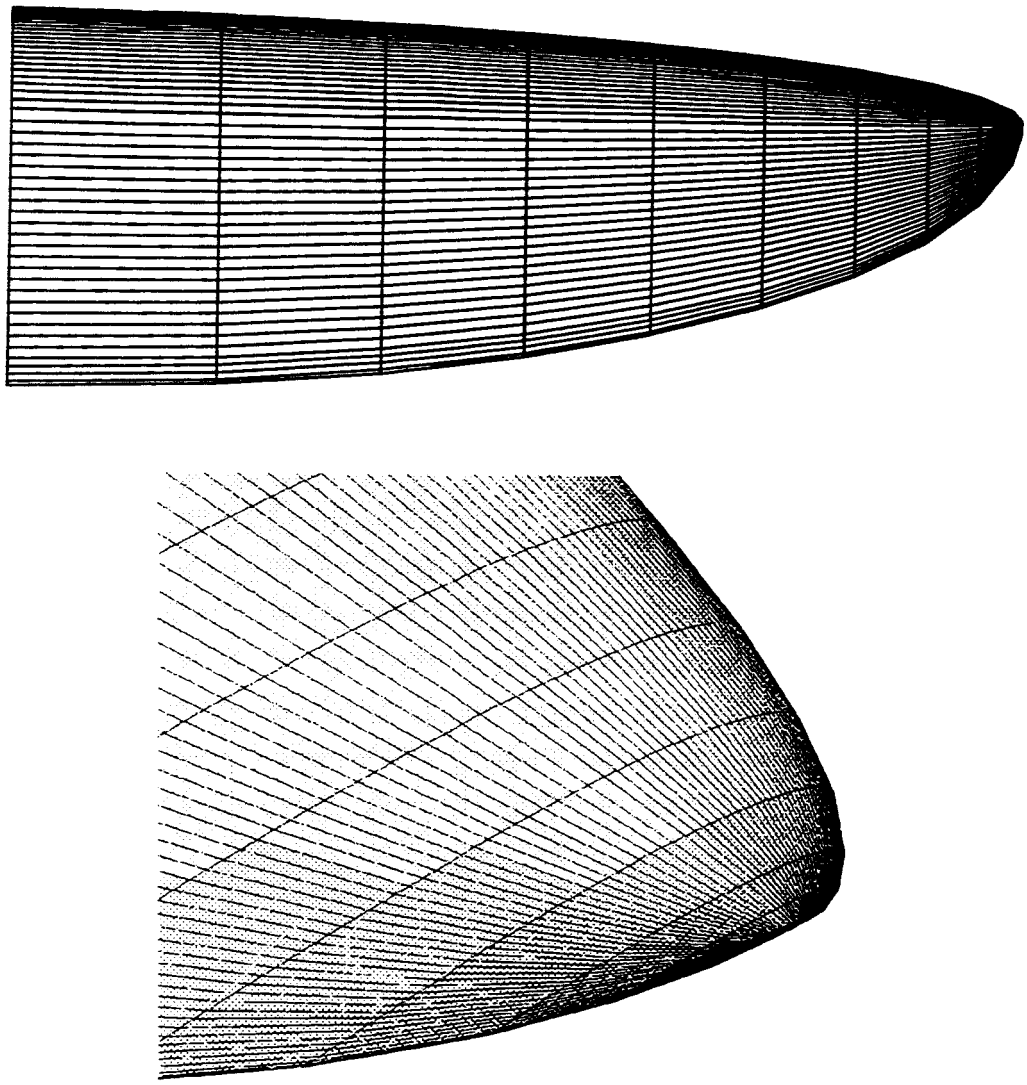

Figure 19. Typical surface panel model.

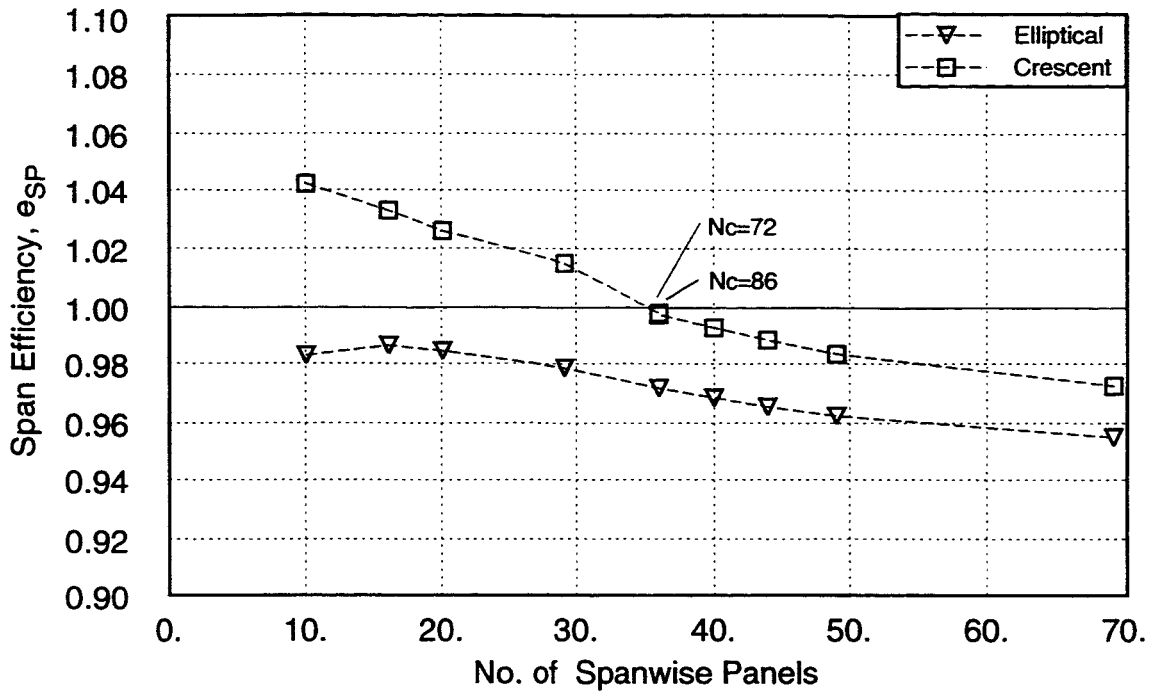

Figure 20. Effect of spanwise panel density on span efficiency computed by surface pressure integration.

decrease, even with Ns = 69, over 11,000 total panels, requiring cpu time well beyond practical limits for most applications.

The spanwise distribution of lift and induced drag for the two wing planforms were determined by integrating the surface pressures on panel columns of constant span. The lift distributions for the crescent and elliptical wings are shown in figure 21, along with a true elliptical distribution. The crescent wing ($X_t = 1.0$) exhibits a more nearly elliptical loading than the classical elliptical wing ($X_t = 0.25$). Recall that the classical elliptical wing concept arises from lifting line theory, where the trailing wake from an elliptical circulation distribution produces uniform downwash on an unswept lifting line. It follows that an elliptical chord distribution would produce the elliptical loading, since the induced angle of attack is constant. In reality, the downwash distribution over the actual wing surface where the bound vorticity is distributed is not uniform, leading to a somewhat nonelliptical loading. Of course, a truly elliptical circulation distribution is unachievable since it requires an infinite vorticity strength along the free edge of the wake.

Figure 22 shows the distribution of induced drag along the span for both wings. The induced drag distribution on the elliptical wing is nearly elliptical, reflecting more or less constant downwash along the span. The effects of sweep on the crescent wing modify the downwash distribution, and therefore the induced drag distribution along the span. Compared with the elliptical wing, the inboard portion of the crescent wing produces less lift and more drag, resulting from greater downwash. Similarly, induced upwash on the the tip region creates a considerable amount of thrust. The rapid variation of

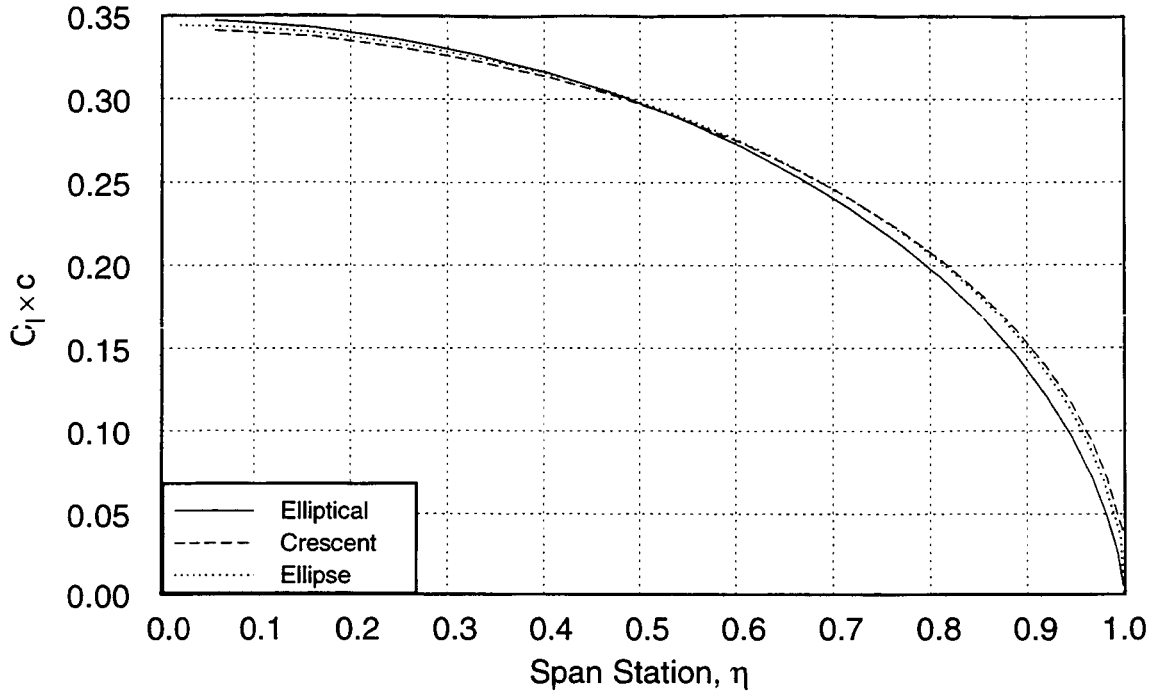

Figure 21. Spanwise lift distribution for elliptical and crescent wings.

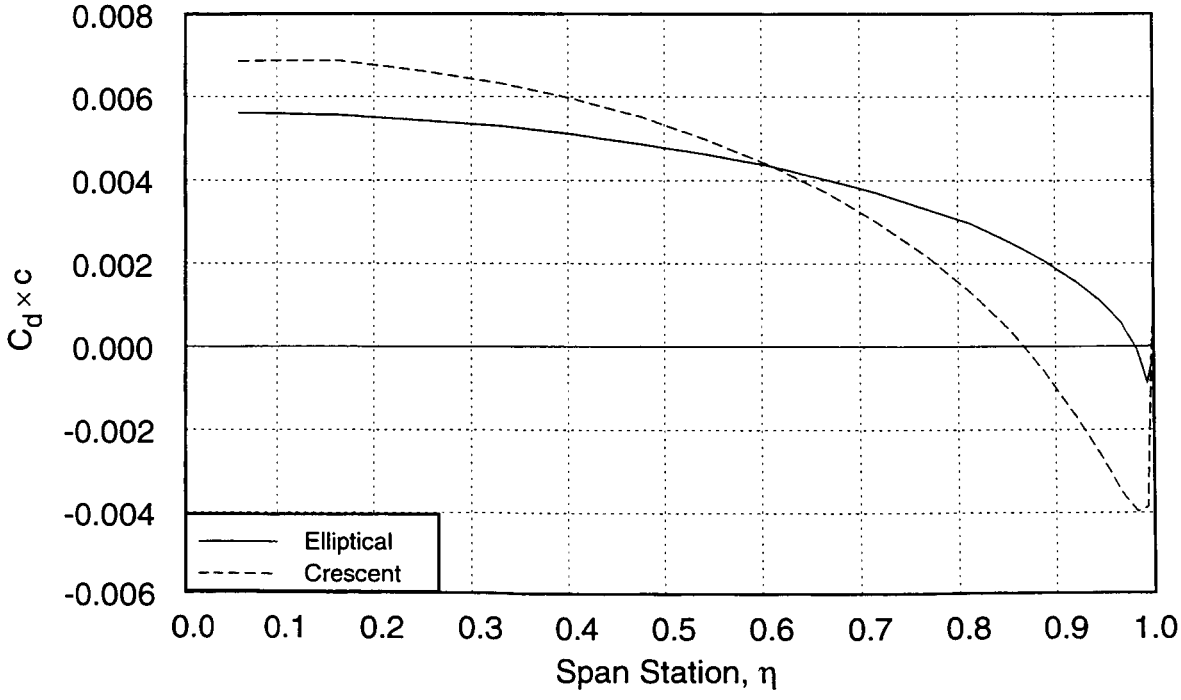

Figure 22. Spanwise drag distribution for elliptical and crescent wings.

drag on the outboard portion of the crescent wing shown in figure 22 indicates large spanwise pressure gradients which are more difficult to resolve, so this planform incurs greater integration error.

Errors in pressure integration are evidently planform dependent when the spanwise resolution is inadequate. The change in span efficiency with initial panel refinement is associated with more accurate resolution of the three-dimensional flow near the wingtip. As the panel density is increased further, the convergence behavior is consistent with the hypothesis described in section 2.2, that the changing physical distance where approximations to the AIC's are introduced makes convergence of the induced drag difficult. DeHaan demonstrated very similar convergence properties with the Douglas panel method (ref. 5).

4.3 Sensitivity to Paneling—Trefftz Plane Integration

For each of these cases, the induced drag was also determined by Trefftz-plane integration, shown in figure 23. Span efficiency was computed from the Trefftz-plane drag and the pressure-integrated lift. There was very little sensitivity of the Trefftz-plane results to spanwise panel density since the distribution of wake properties was integrated numerically. With Ns = 10, the computed drag of the elliptical wing is within 1 percent of the result with Ns =20, and within 1.5 percent of the result with Ns = 69. The computed span efficiency of the crescent wing is 0.991, compared with a span efficiency of 0.984 for the elliptical wing. The crescent wing result is 0.85 percent better than the elliptical wing, half the drag reduction predicted from highest resolution pressure integration.

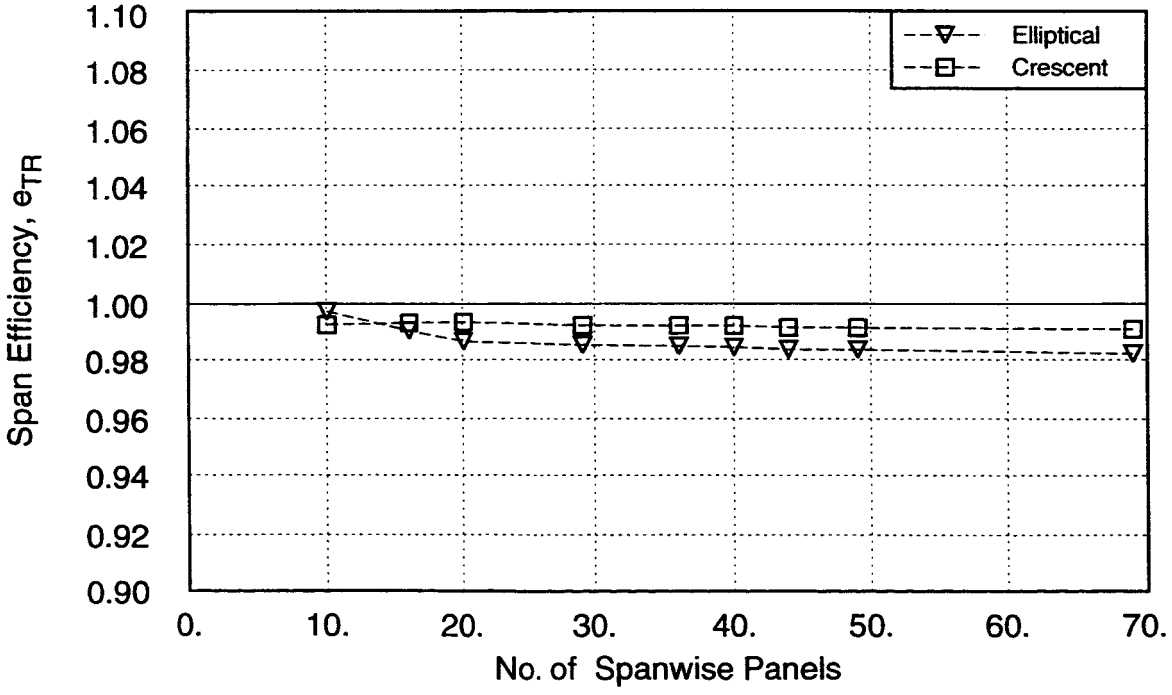

Figure 23. Effect of spanwise panel density on span efficiency computed by Trefftz-plane integration.

4.4 Sensitivity to Angle of Attack

To further study the reliability of both methods of induced drag computation, both wings were run at various angles of attack. For the untwisted planforms studied here, the span efficiency should not vary with angle of attack, except for the (very small) effect of the nonplanar wake on the elliptical wing, which should increase span efficiency at higher angles of attack. As angle of attack was varied, the location and shape of the leading edge suction peak changes, affecting the accuracy of the surface-pressure integration. In addition, the induced drag at low angles of attack is quite small, so numerical errors may have a more significant impact on the integration. The variation of span efficiency found by surface-pressure integration, shown in figure 24, seems to indicate that this is indeed the case. Even with very high panel density (Nc $\times$ Ns = 86 $\times$ 36), the pressure-integration results show strong dependence on angle of attack. No such dependence on angle of attack is evident in the Trefftz-plane integration, as shown in figure 25.

4.5 Conclusions Regarding Computational Prediction of Induced Drag

When the spanwise panel density is increased sufficiently, the span efficiency found by pressure integration is slightly less than 1.0 for both the elliptical and crescent wings. These results are consistent with the nearly elliptical span loading produced by both wings. The unusually high span efficiencies reported by Van Dam are apparently a numerical artifact of inaccurate pressure integration. The lack of convergence of the drag predicted by pressure integration, and the sensitivity to planform, indicates that this is not a satisfactory method for comparing span efficiency of various wings.

Trefftz-plane integration is evidently a much more reliable method of determining induced drag. The span efficiency computed with 20 spanwise panels agrees with the result using 69 spanwise panels to within 0.5 percent. The 0.85 percent difference in span efficiency between the elliptical and crescent wings, analyzed with streamwise wake models, is consistent with the difference in span loading. The impact of correctly modeling the force-free wake on the induced drag of these wings is discussed in section 6.

4.6 Modification of Elliptical Wing to Achieve Elliptic Span-Loading

As observed in section 4.1, the spanwise lift distribution on the $X_t = 0.25$ elliptical wing deviates somewhat from an elliptic distribution. This is the result of nonuniform downwash induced over the wing surface by the trailing wake. The effective sweep of the outboard region of the $X_t = 1.00$ crescent wing modifies the downwash distribution, leading to a more nearly elliptic loading. Camber, twist, or alteration of the chord distribution may also be used to increase the loading on the outboard region of the unswept wing. From the point of view of the airplane designer, camber and especially twist modifications are undesirable for increasing the loading near the tip, since premature tip stall may result. An increase in chord would have the effect of achieving a more desirable span loading while

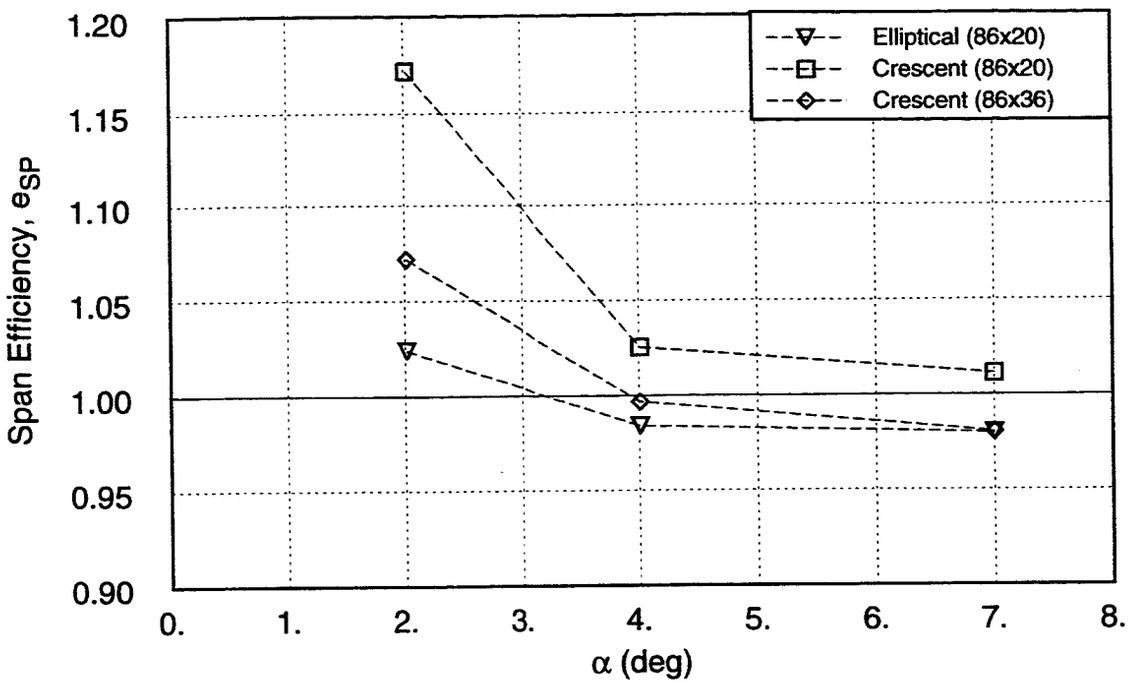

Figure 24. Effect of angle of attack on span efficiency computed by surface pressure integration.

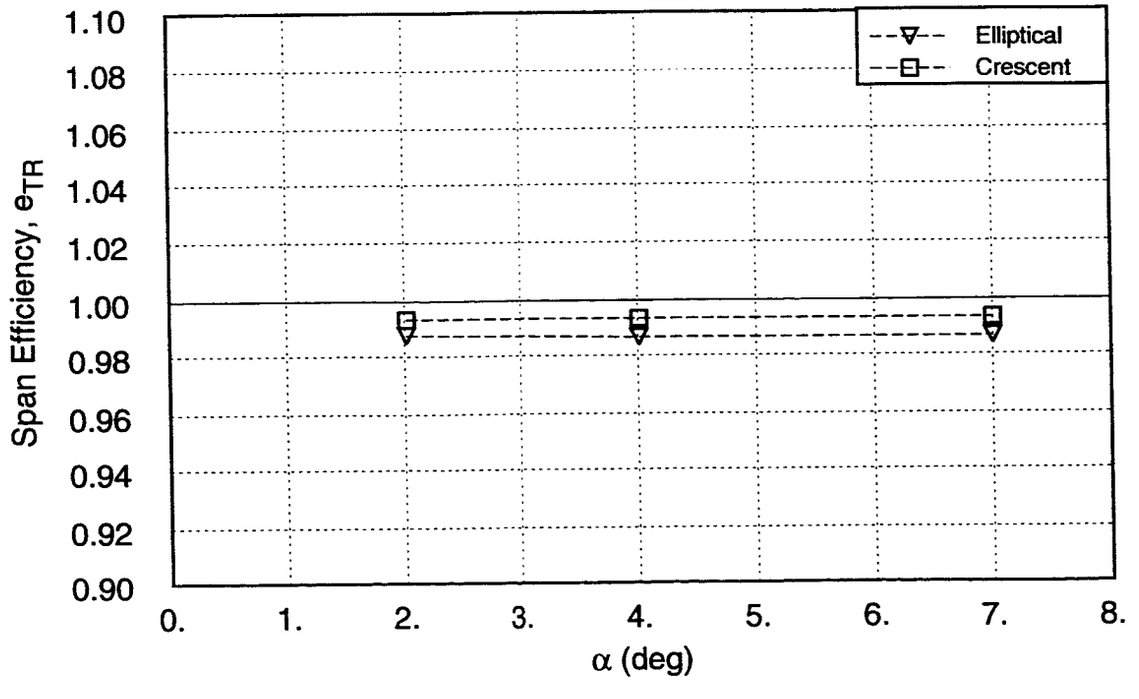

Figure 25. Effect of angle of attack on span efficiency computed by Trefftz-plane integration.

reducing the section loading, delaying stall. The chord distribution of the $X_t = 0.25$ wing was modified through an iterative process of increasing the chord by the amount (percentage) of the deficit in loading at each span station. The span loading for the new wing was computed and the process was repeated. Three iterations of this process produced the wing planform shown in figure 26. As shown in figure 27, the lift distribution for this wing is as close to the elliptic loading as the $X_t = 1.00$ crescent wing. The computed span efficiency for this wing was 0.990, the same as the $X_t = 1.00$ crescent wing.

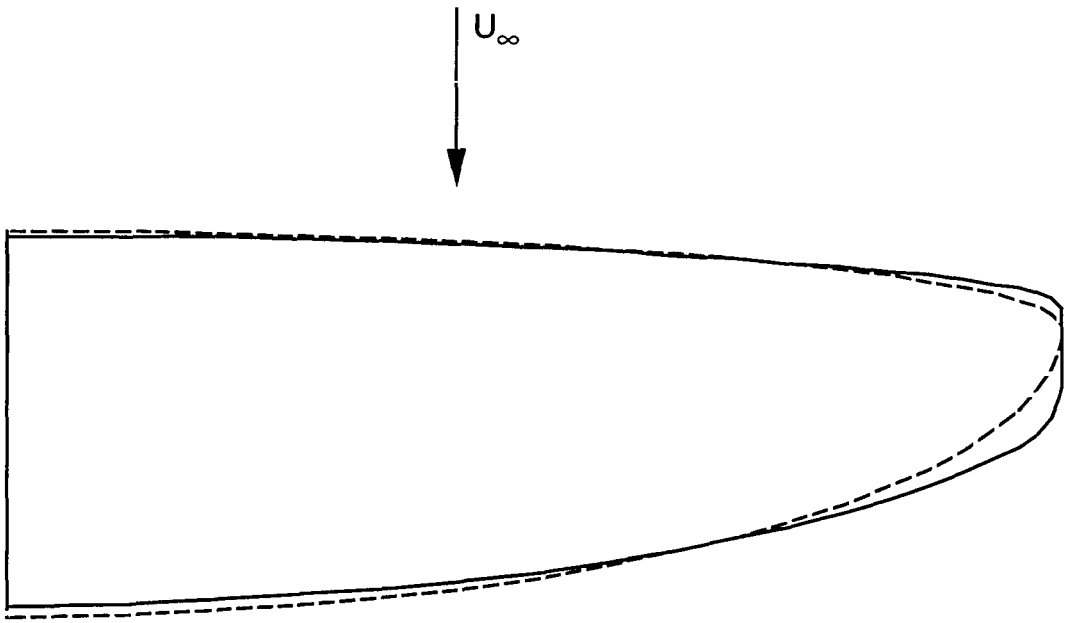

Figure 26. Modified $X_t = 0.25$ elliptical wing.

4.7 Transonic Induced Drag Computation

The same Trefftz-plane procedure used in section 4.1 may be used with a transonic full-potential flow solver, provided the required wake properties can be obtained. To evaluate the Trefftz-plane procedure for transonic flows, the $X_t = 1.00$ crescent wing was analyzed with the Tranair full-potential code with the angle of attack fixed at 5 deg.

The first task in using the Tranair code was to develop a set of grid directives that produced an accurate "grid-independent" solution. Tranair allows the user to identify regions of the solution where different constraints on the level of grid refinement may be imposed. The automated procedure for solution-adaptive grid refinement within Tranair focuses on regions with high flow gradients such as the leading edge and wingtip regions. Without constraints on grid refinement, Tranair would over-emphasize these regions at the expense of regions where the gradients are relatively small, such as the mid-chord region of the wing.

Initial solutions of Tranair at a Mach number of 0.01 with various grid directives resulted in as much as 2 percent variation in predicted lift coefficient. Analysis of these results indicated that poor

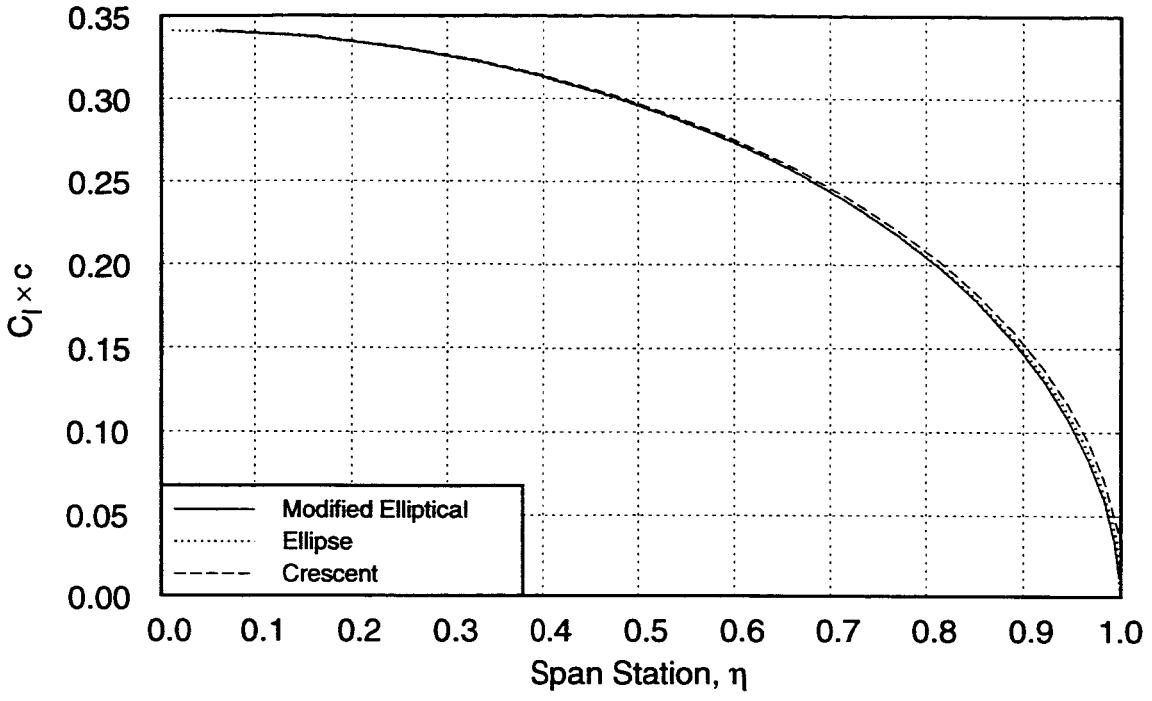

Figure 27. Spanwise lift distribution for modified elliptical and crescent wings.

resolution of the flow in the mid-chord region of the wing was the source of the variation. Subsequent solutions used grid directives to enforce a minimum level of grid refinement in this area. Three solutions were obtained with minimum refinements of 2 levels, 3 levels, and 4 levels, and a maximum refinement of 7 levels. The total number of grid boxes used were 510,000, 630,000, and 770,000, respectively. The variation in lift coefficient for these three solutions was 0.2 percent. A cross-sectional slice through the grid illustrates the unstructured cartesian grid, shown in figure 28.

Trefftz-plane drag integration was applied to Tranair solutions for Mach numbers of 0.01 through 0.70 to study the effect of Mach number on the span efficiency of an unswept wing. The Trefftz plane was located 5 semispans downstream of the trailing edge. As with the panel-code study in section 4.1, span efficiency was computed from the pressure-integrated lift and the Trefftz-plane integrated drag. There was a small increase in computed span efficiency with increasing Mach number, up to the critical Mach number, as shown in table 1. Above the critical Mach number, the span efficiency decreases slightly. The span efficiency predicted for the crescent wing at Mach number = 0.01 is about 1.5 percent higher than the same case predicted by the A502 panel code. This difference is not surprising given the entirely different solution method and assumptions. As one would expect from the nearly-constant span efficiency, there was no influence of Mach number on the shape of the spanwise lift distribution of the crescent wing, shown in figure 29. Since the angle of attack was fixed, the wing lift coefficient increased with Mach number. As an aid in comparing the shape of the lift distributions, the lift

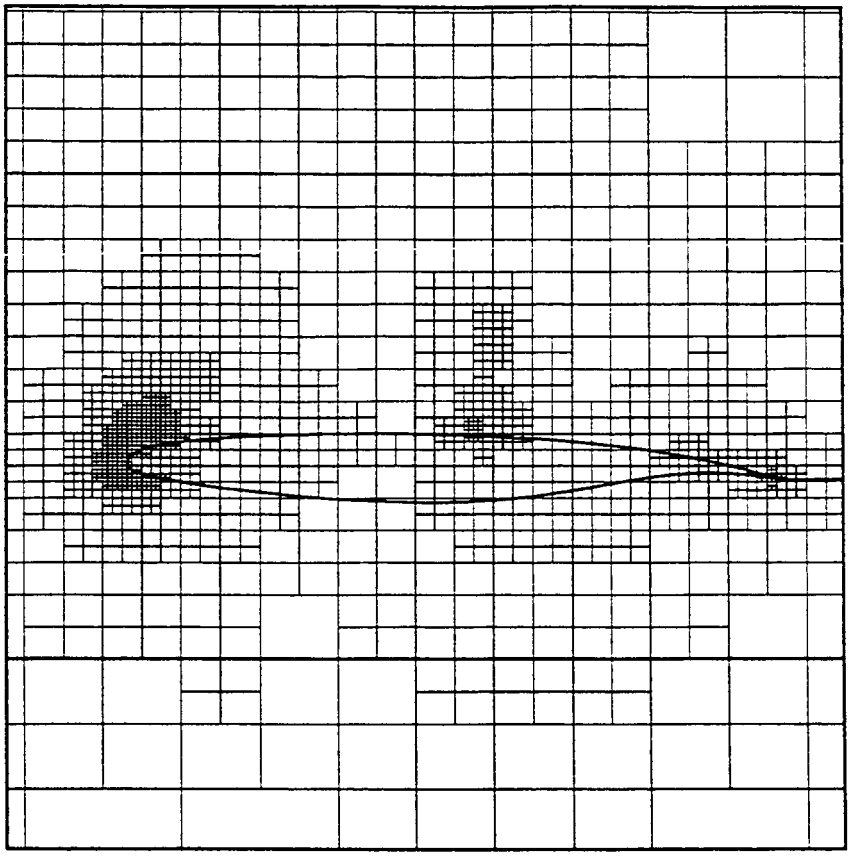

Figure 28. Typical solution-adapted Tranair grid.

Table 1. Span efficiency versus Mach number for the $X_t = 1.00$ crescent wing, $\alpha = 5°$

Mach no.	0.01	0.3	0.5	0.6	0.65	0.7
C_L	0.427	0.442	0.478	0.512	0.533	0.569
e	1.006	1.007	1.009	1.011	1.012	1.002

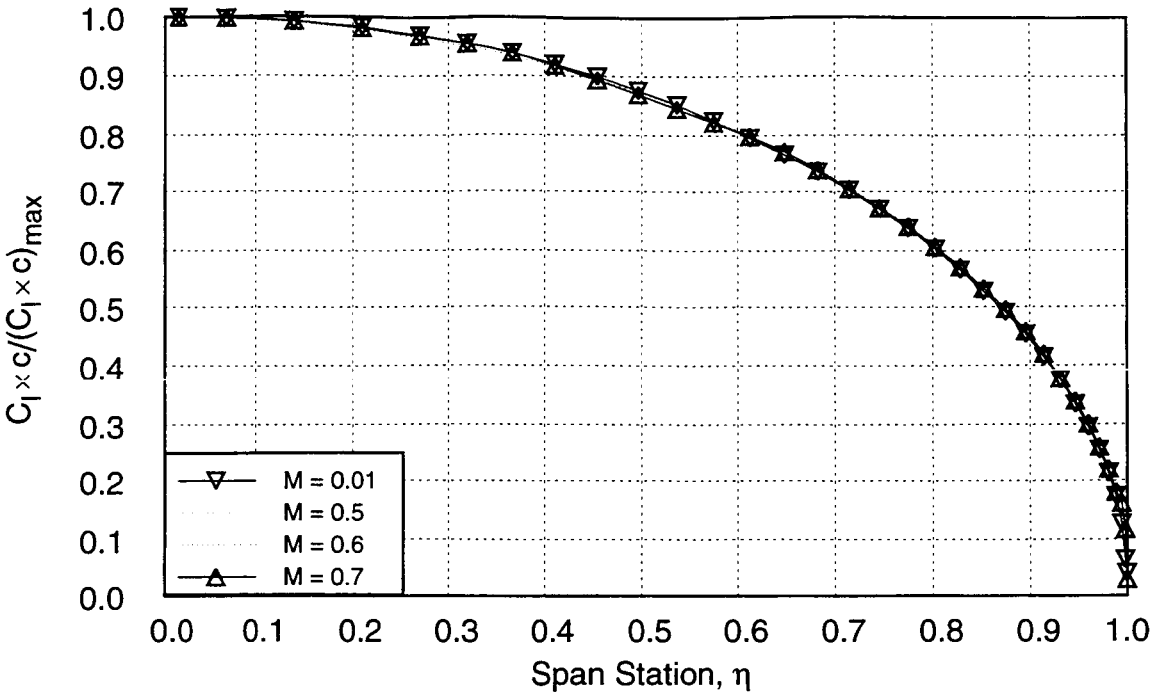

Figure 29. Spanwise lift distribution for crescent wing versus Mach number.

distributions plotted in figure 29 have been normalized by maximum section lift coefficient for each Mach number.

These results demonstrate the conclusion from section 3 that the wave drag does not appear in the Trefftz plane for potential flows. The solution at Mach number of 0.7 had considerable supersonic flow and a large shock on the upper surface, yet the computed span efficiency is very near the subsonic value.

5 INFLUENCE OF COMPRESSIBILITY ON INDUCED DRAG

In the last section, the technique for computing induced drag in the Trefftz plane was demonstrated for transonic flow using the Tranair full-potential code. Results for the unswept crescent wing indicated that there was no significant change in spanwise lift distribution or computed span efficiency as the Mach number was increased. While useful as a test case, the crescent wing is not representative of wings designed for transonic flight. Compressibility may be expected to affect the induced drag through two mechanisms. First, while the induced drag produced by a given circulation distribution is not affected by Mach number, the lift is affected by the change in the relationship between velocity and pressure. Second, the spanwise lift distribution of a swept wing is expected to change as Mach number is increased. The influence of Mach number on a swept wing is anticipated by the Prandtl-Glauert transformation, which has the effect of stretching the geometry in the freestream direction, increasing the effective wing sweep. The increase in sweep changes the lift distribution. While this effect is included in the solution of the linear Prandtl-Glauert equation, its effect especially important for "supercritical" wings that operate under conditions where the Prandtl-Glauert equation is no longer valid. In this section, the influence of compressibility on a modern supercritical swept wing designed for a commercial transport is investigated.

5.1 Relationship Between Circulation and Lift in Transonic Flow

In incompressible flow, the Kutta-Joukowski law expresses the relationship between circulation and lift in two dimensional flow as $L' = \rho U_\infty \Gamma$. The lift on a finite wing may be found by integration of the circulation along the span, or equivalently, by integration of the circulation in the trailing wake. But the lift is also the resultant of the surface pressure distribution. The circulation and the pressure distribution are both related to the velocity distribution over the wing. The circulation is defined by a contour integral around the airfoil, $\mathbf{\Gamma} = \oint \mathbf{V} \cdot \hat{\mathbf{t}} dl$, while the pressure is related to the velocity by the Bernoulli equation.

The equivalence of the lift determined by the circulation and pressure integration in incompressible flow is easily demonstrated by a simple model problem of a constant-pressure panel, shown in figure 30. An appropriate distribution of vorticity is specified on the thin panel so that the perturbation velocity on the surface is constant. The circulation becomes $\mathbf{\Gamma} = \int \mathbf{V} \cdot \hat{\mathbf{t}}\, dl = 2uc$, and the lift is $L' = \rho U_\infty \Gamma = 2\rho u U_\infty c$. The pressure on the upper and lower surfaces are $p_u = p_\infty - \frac{1}{2}\rho(u^2 + 2uU_\infty)$ and $p_l = p_\infty + \frac{1}{2}\rho(u^2 + 2uU_\infty)$, so the pressure integrated lift is $(p_l - p_u)c = 2\rho u U_\infty c$.

The relationship between pressure and velocity is modified in compressible flow, as described by the isentropic Bernoulli equation. For a given u-component velocity perturbation, the local pressure changes as Mach number is increased. However, since the circulation is not affected by the increase in Mach number, a discrepancy develops between the Kutta-Joukowski lift and the pressure-integrated lift. To assess the magnitude of this discrepancy, the lift on the constant-pressure panel, figure 30,

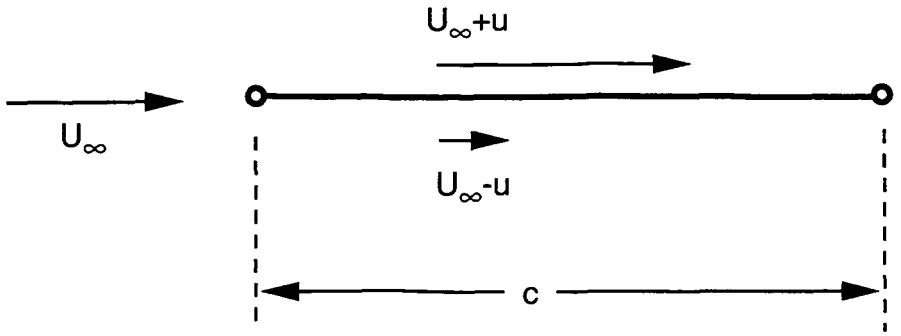

Figure 30. Constant pressure panel for calculation of circulation and lift.

was evaluated by both methods for a range of Mach numbers and panel lift coefficients. As shown in figure 31, compressibility reduces the lift below the value predicted by the Kutta-Joukowski law by a modest amount, about 2 percent at a Mach number of 0.8 and a lift coefficient of 1.0. On a real wing, this effect varies over the surface with the magnitude of the local velocity perturbation, and the actual reduction in lift must be determined numerically.

As discussed in section 3, the Trefftz-plane drag is not affected by compressibility since the velocity perturbations in the far field are small. The expected result of this loss of lift with fixed circulation is a small decrease in span efficiency as Mach number is increased. The induced drag predictions for the $X_t = 1.0$ crescent wing in section 4 did not indicate that this compressibility effect was significant, but those calculations were limited to a Mach number of 0.7 and a C_L of 0.57. This effect will be studied further in the next section, using a modern "supercritical wing" design for a commercial transport.

5.2 Influence of Mach Number on the Induced Drag of a Swept Wing

As mentioned above, a change in the spanwise lift distribution of a swept wing is anticipated by the Prandtl-Glauert equation. While this may be regarded as a linear effect, its consequences are especially important as Mach number increases beyond the range where the Prandtl-Glauert equation is applicable, necessitating nonlinear analysis.

To study this effect on lift distribution, and the corresponding effect on span efficiency, a modern supercritical wing designed for a commercial transport was analyzed with Tranair. The wing planform is shown in figure 32. The wing geometry included the wing deflection under 1–g flight conditions. The wing upper and lower surfaces were modeled with a panel distribution of Ns = 32 and Nc = 76. The spanwise panel distribution was approximately uniformly spaced over the inboard 85 percent of the span, with closer spacing near the tip. A streamwise wake model was used, with the Trefftz-plane survey located 6 semispans downstream of the trailing edge. The distribution of Trefftz-plane survey points is determined by the spanwise panel distribution. While this distribution was less desirable for Trefftz plane integration than the cosine distribution normally used, it was considered adequate for a study of the relative effects of Mach number on lift distribution and span efficiency. The grid directives

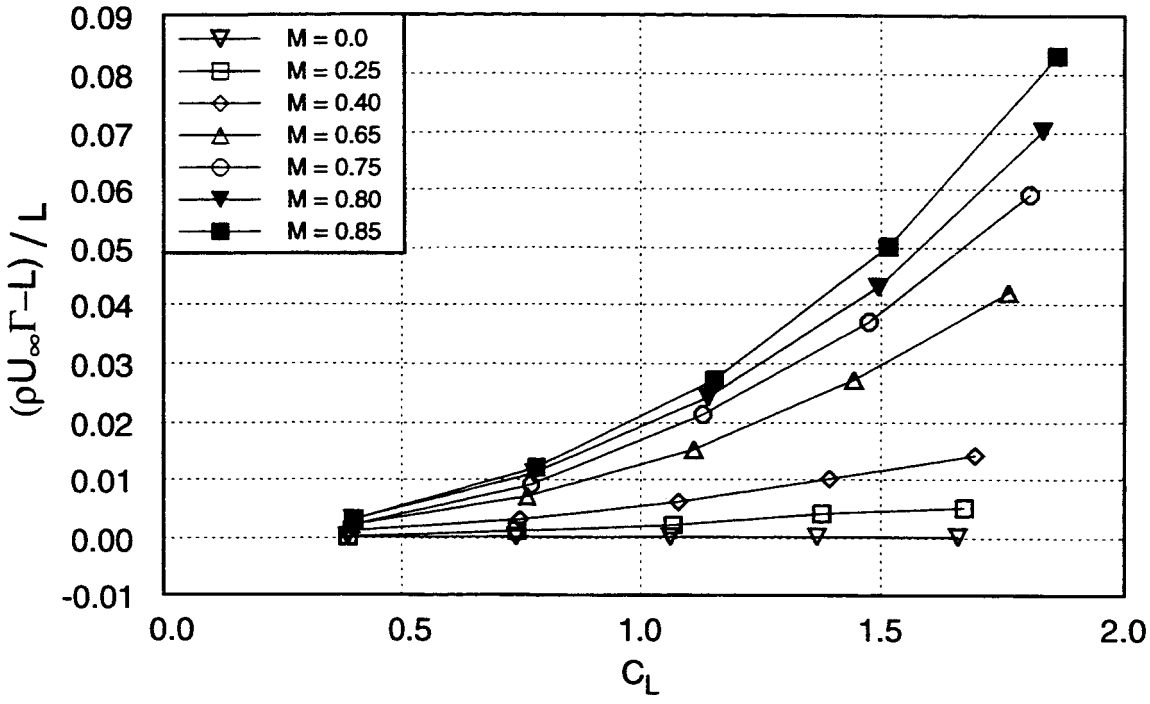

Figure 31. Effect of Mach number on relationship between circulation and lift.

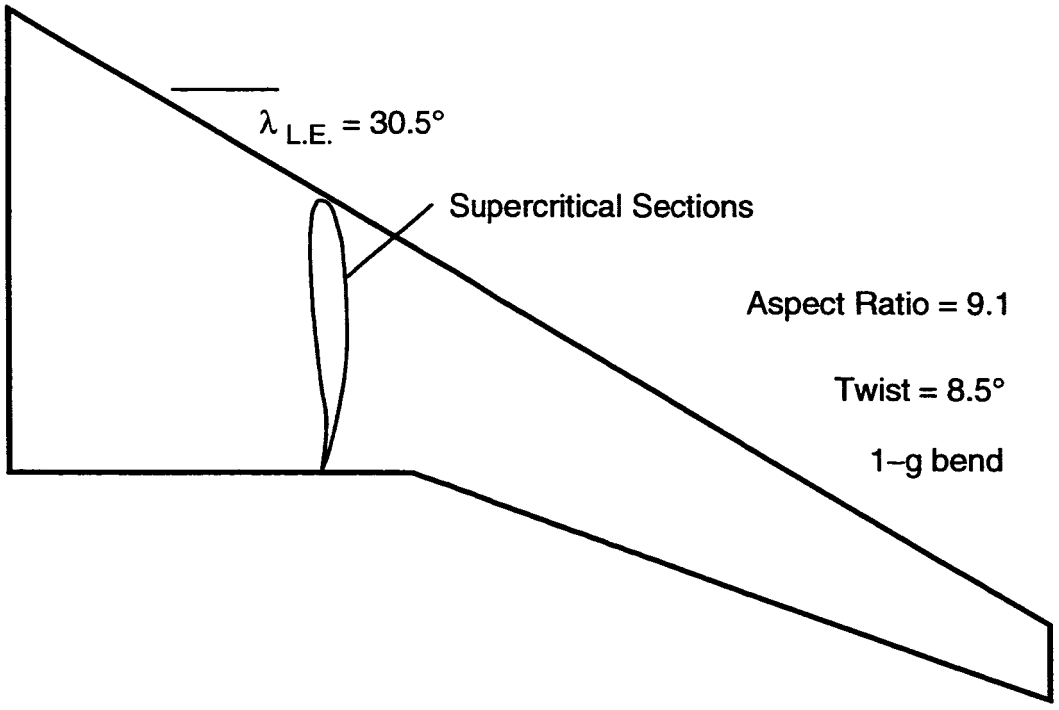

Figure 32. Modern transonic transport wing.

specified to control the solution-adaptive grid scheme of Tranair were the same as those used for the crescent wing in section 4. The solution used a total of 770,000 grid boxes, with minimum of three levels, and at most seven levels of grid refinement on the wing surface. Span efficiency was computed using the same technique as described in section 4, using the pressure-integrated lift and the Trefftz-plane integrated drag. The wing was analyzed at Mach numbers of 0.01, 0.6, 0.7, and 0.8, with the angle of attack fixed at 2 deg. The same wing geometry was also analyzed with the A502 high-order panel method at Mach numbers of 0.01 and 0.6. The spanwise lift distributions for these conditions are shown in figure 33. The lift distributions have been normalized by the maximum lift for each case to allow comparison of the distribution shapes. As expected, the lift distribution on the swept wing was affected by increasing Mach number. The increase in effective sweep produced an increase in the loading on the outer portion of the wing. At a Mach number of 0.01, the Tranair and A502 solutions agree, whereas at a Mach number of 0.6, there is slight disagreement. At Mach 0.6, a small region of supersonic flow was present on the inboard third of the wing near the leading edge, indicating that this case is slightly above the range of validity for the linear panel method. Since the wing was designed to fly at a Mach number of 0.8, the nonlinear full-potential method was required to design the wing to achieve the desired spanwise lift distribution.

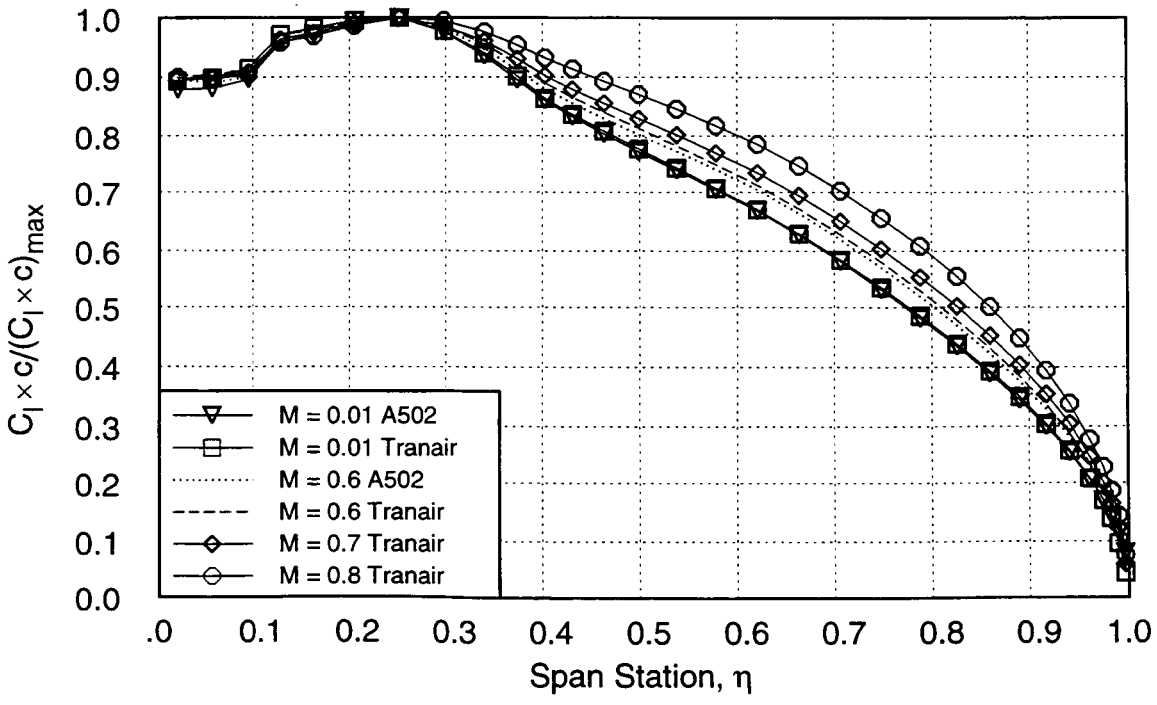

Figure 33. Effect of Mach number on spanwise lift distribution of modern transonic transport wing, $\alpha = 2$ deg.

The predicted span efficiency for this wing over this range of Mach number is given in table 2. It was observed in section 4 that the span efficiency predicted with Tranair is typically 1.5 percent higher than the A502 result. This characteristic is evident here as well. In addition, the spanwise distribution of survey points for Trefftz plane analysis may not produce results of comparable accuracy to the crescent wing study. Despite the issue of absolute accuracy, these results are expected to reflect the trend in span efficiency with increasing Mach number. It is evident that there is an increase in span efficiency with increasing Mach number, due to the change in the spanwise lift distribution. Although a span efficiency of 1.05 may seem unlikely, the 1–g wing deflection produces a nonplanar wake with a height-to-semispan ratio (2h/b) of 0.18. Based on reference 7, an optimally loaded wing with circular deflection of this magnitude is expected to achieve a span efficiency of 1.02.

To investigate the significance of the compressibility effect that reduces the lift below the value expected from the circulation, the lift was calculated in the Trefftz plane by integration of $L = \rho U_\infty \int \Delta\phi \frac{\partial \phi}{\partial \tilde{\mathbf{n}}} dy$ along the wake trace. The resulting values of lift coefficient are compared with the pressure-integrated lift in table 3. The lift computed in the Trefftz plane is slightly less than the pressure-integrated value at very low Mach number, while the two methods agree more closely at a Mach number of 0.8. This may indicate that the compressible effect of reducing the pressure-integrated lift slightly is present here, but the effect is evidently negligible for this wing at this Mach number and lift coefficient.

Table 2. Variation of span efficiency with Mach number for swept wing, $\alpha = 2°$

Mach no.	0.01	0.6	0.7	0.8
C_L	0.366	0.435	0.479	0.593
e_A502	0.974	0.988		
e_Tranair	0.985	1.013	1.026	1.051

Table 3. Comparison of pressure-integrated lift and lift based on circulation

Mach no.	0.01	0.8
C_L_pressure int.	0.3662	0.5929
C_L_$\rho U_\infty \Gamma$	0.3654	0.5925
% difference	−0.2%	−0.06%

6 COMPUTATIONAL MODELING OF FORCE-FREE WAKES

The far-field drag expressions derived in section 3 indicate the importance of accurately modeling at least the initial roll-up of the near-wake if any favorable interaction is to be found. As cited in section 1, a variety of techniques exist for computing the force-free wake shape downstream of the wing. The most widely used methods use a vortex-lattice model of the wing and wake (refs. 27–32). Both collocation and time-marching schemes have been used to relax the discrete-vortex wake to the force-free shape. In all cases, the velocities induced on the wake are computed and the wake is displaced to align the wake vortices with the local flow. A viscous core model is required to prevent erratic behavior of the vortex filaments when they pass near each other. Most schemes use some variation of Lamb's core model (ref. 29). Once the force-free wake shape is created, it can then be converted to a panel geometry for drag analysis by the high-order panel code, using the technique demonstrated in section 4.

6.1 Initial Studies with Vortex-Lattice Wake Relaxation

To study the influence of wake modeling on the computation of induced drag for the wings described in section 4, the time-marching vortex-lattice wake relaxation program of reference 27 was used to create a rolled-up wake model for $X_t = 1.00$ crescent wing at 4.0 deg angle of attack. The wake was modeled by 50 trailing vortex filaments, distributed by a cosine function along the span. The timestep was chosen so that the streamwise resolution was 0.1 chord. The wake was allowed to grow to a point 20 semispans downstream, and then truncated to a length of 15 semispans to remove the starting vortex and the region of wake distorted by its influence.

A panel model was created with NACA 0012 airfoils on the wing and the wake geometry defined by the relaxed discrete-vortex wake. The 50-vortex wake model was edited to 18 spanwise panels on the wing and wake. The thickness effects captured by the panel model of the wing resulted in higher lift than the mean-surface vortex lattice model at the same angle of attack. The angle of attack of the wing was adjusted to 3.57 deg to match the lift coefficient of the vortex-lattice model. This is important since it is the wing circulation that determines the wake shape.

The computed span efficiency for this model was 1.035, almost 5 percent higher than the expected value based on the streamwise wake result, $e = 0.99$. For the $X_t = 1.00$ crescent wing (straight trailing edge), the hypothesis presented in section 3 predicts that the substitution of the streamwise wake should have very little effect, since the partition may be moved to the trailing edge, completely eliminating the force-free wake.

The same vortex-lattice wake was re-edited to create a panel model with 19 spanwise panels to improve the resolution of the wake roll-up. The span efficiency computed with this wake was 1.058. A second vortex-lattice wake was generated with half the timestep size, again to improve the resolution of the wake shape. The panel model was again edited to 19 spanwise panels. For this wake, the computed

span efficiency was 1.082. The small change in wake shape that produced this large change in the computed span efficiency is shown in figure 34.

The results in section 4 demonstrate that 18 panels provide adequate numerical resolution for integration in the Trefftz-plane. The unexpected low drag prediction, and the variation in predicted drag from small changes in the wake model, were assumed to be more likely related to errors in wake shape (not drag-free) than to any favorable influence of the rolled-up wake. Evidently, the drag computed in the Trefftz plane is highly sensitive to details of the wake shape.

One possible source of error in wake shape is the approximation of the wing boundary conditions inherent to the vortex-lattice method. The wake shape is determined by velocities induced by the bound and trailing vortex systems. But vortex-lattice methods have velocity singularities at the panel edges, and the velocities are correct only at the control points. Significant velocity errors exist at other points in the field. If velocity errors exist on the wake near the trailing edge, this would lead to errors in wake shape.

A simple mean-surface model of an $AR = 5$ rectangular wing was used to compare the wake velocities predicted by the vortex-lattice code and the high-order panel code (A502). The wing model had 20 uniformly spaced spanwise panels and 6 chordwise panels, typical of what would be used for a wake relaxation problem. Figure 35 shows distributions of normal velocity, w, on the wake for the first chordlength downstream of the trailing edge, at 82 percent semispan. The vortex-lattice method predicts normal velocities very similar to those from A502, except in the immediate vicinity of the trailing edge. The discrete vortex representation does not accurately model the wing flow at the trailing edge.

6.2 A Hybrid Wake Relaxation Scheme

One method of improving the velocities near the trailing edge is a hybrid wake-relaxation method that takes advantage of the more accurate velocities of the panel method while exploiting the well-behaved nature of the discrete-vortex wake with a viscous-core model. The high-order panel method is used to compute the velocities induced on the wake by the wing, while the velocities induced by the wake itself are computed from the discrete-vortex model. The wake vortex strengths are determined from the vorticity distribution on the wake from the panel code. The relaxation scheme iteratively repositions the wake to be tangent to the local flow.

A flow chart of the iteration process used to relax the wake shape is shown in figure 36. The notation used to identify the nodal locations in the wake is shown in figure 37. At the beginning of each iteration, a complete flow solution for the wing and wake geometry is obtained from the high-order panel code. The aerodynamic influence coefficient (AIC) matrix and the singularity strengths for this solution are saved to permit evaluation of field velocities from the solution. A survey of wake properties along the wing trailing edge is used to determine the wake circulation, given by the jump in potential

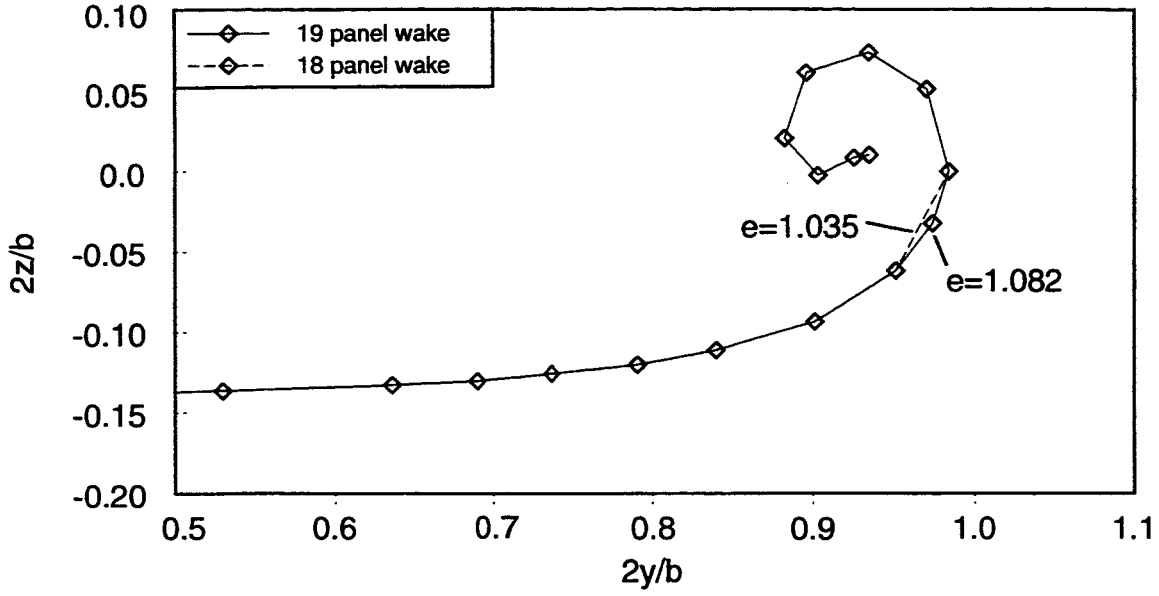

Figure 34. Computed span efficiency affected by small change in wake shape.

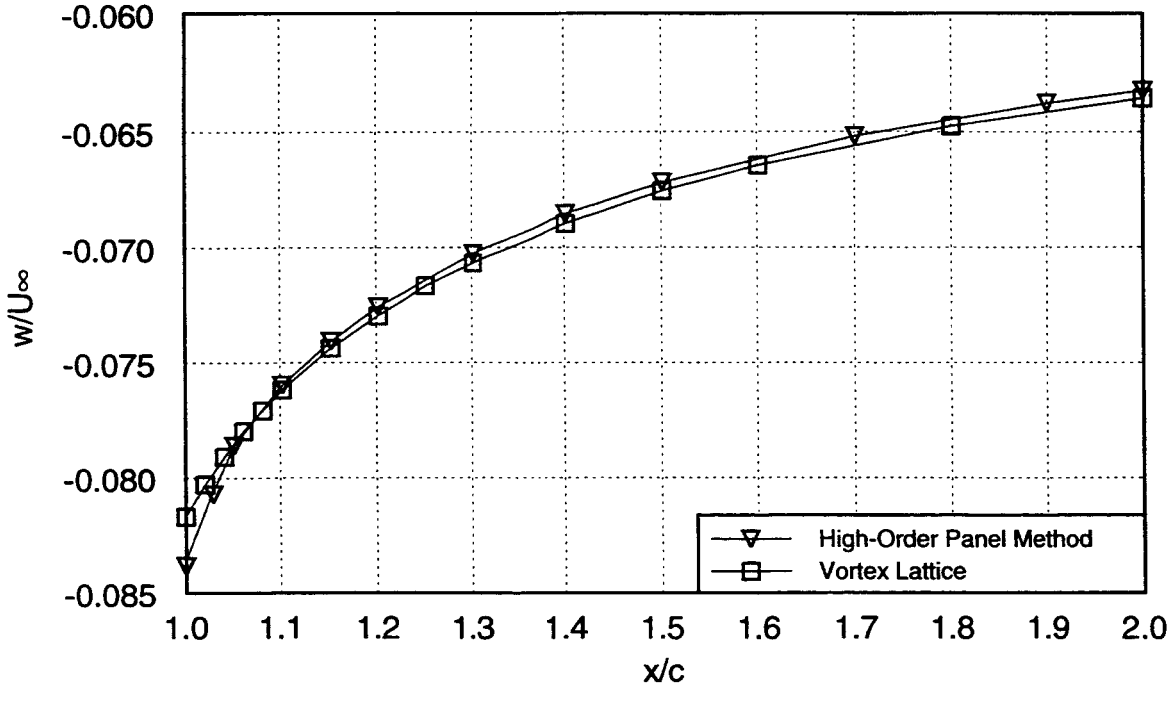

Figure 35. Downwash on wake, w, near trailing edge predicted by vortex-lattice method and high-order panel method.

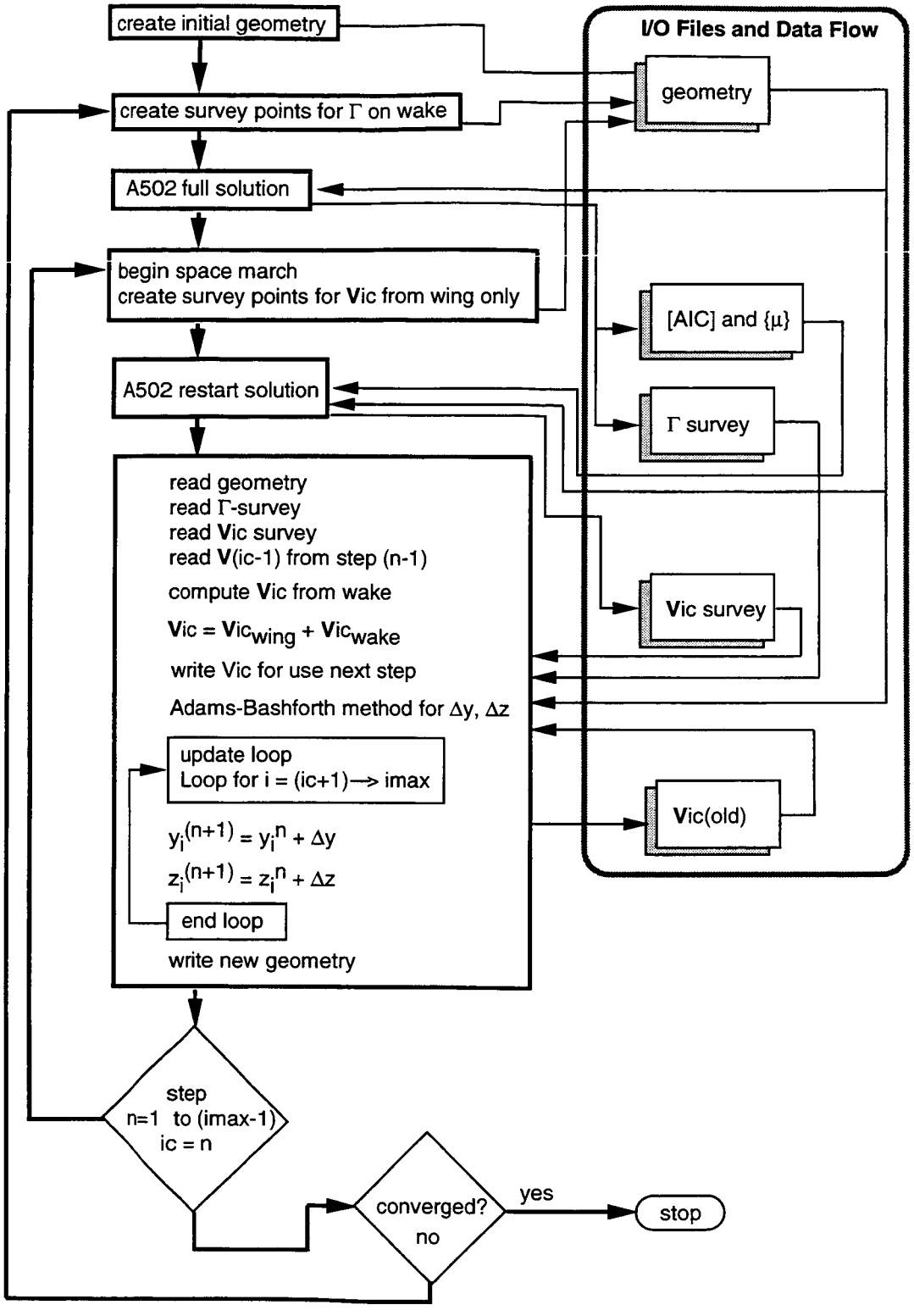

Figure 36. Hybrid wake relaxation process.

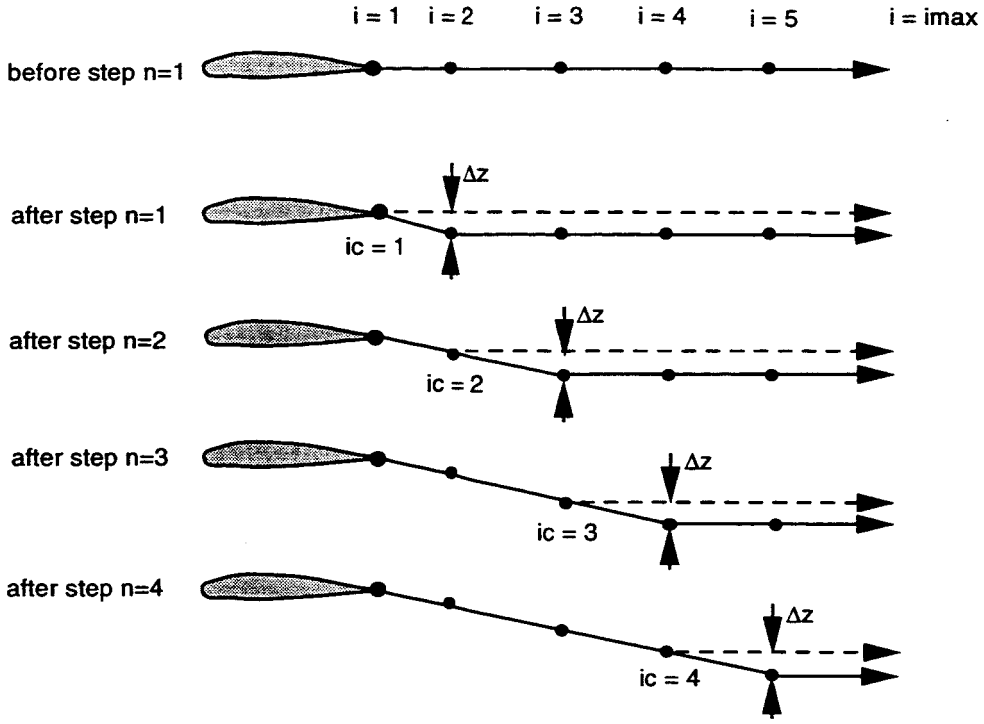

Figure 37. Sequence of steps of space march.

across the wake, $\Delta\phi$ and an equivalent discrete-vortex representation of the wake is constructed. The discrete vortex locations correspond to the panel edges of the distributed wake of the panel model. The vortex strength is equal to the drop in circulation from one panel-center to the next, $\gamma_j = \Delta\phi_{j+1} - \Delta\phi_j$. A downstream space-march is then used to convect the wake to align it with the local flow. Figure 37 shows the sequence of steps of this space-march. The restart feature of the panel code allows the saved AIC's and singularity strengths to be used to compute the velocities induced by the wing system (not including the wake) along a spanwise row of nodes on the wake. The wing-induced velocities are combined with velocities induced by the discrete-vortex wake, which are computed at the same nodes using the Biot-Savart law, modified by the viscous-core model of reference 27:

$$V_i = V_{b.s.}(1 - e^{\frac{(-h^2 V_\infty}{4\nu x}}) \tag{42}$$

where V_i is the induced velocity, $V_{b.s}$ is the induced velocity computed by the Biot-Savart law, h is the radial distance from the vortex, and x is the distance from the vortex source (trailing edge). A value of effective core viscosity, $\nu = 0.00075$ was found to be suitable. A second-order Adams-Bashforth method uses these hybrid velocities and those saved from the previous row of nodes to determine the correct location of the next row of nodes so that the intervening wake segment is tangent to the local flow:

$$Y^*_{i+1} = Y_i + \frac{dx}{U_\infty}(\frac{3}{2}v_i - \frac{1}{2}v_{i-1}) \tag{43}$$

$$Z^*_{i+1} = Z_i + \frac{dx}{U_\infty}(\frac{3}{2}w_i - \frac{1}{2}w_{i-1}) \tag{44}$$

where Y^*, Z^* are interim values, and i is the current node index. Although the convergence rate is reduced, the method is more robust with the nodal displacement reduced by an under-relaxation factor, r, such that:

$$dy = r(Y^*_{i+1} - Y^{n-1}_{i+1}) \tag{45}$$

$$dz = r(Z^*_{i+1} - Z^{n-1}_{i+1}) \tag{46}$$

Finally, the nodal displacements are applied:

$$Y^n_{i+1\rightarrow imax} = Y^{n-1}_{i+1\rightarrow imax} + dy \tag{47}$$

$$Z^n_{i+1\rightarrow imax} = Z^{n-1}_{i+1\rightarrow imax} + dz \tag{48}$$

where i is the node index and n is the iteration index. For this study, an under-relaxation value of $r = 0.5$ was used. Note that at each step in the space march, the entire wake downstream of the current node is displaced, as illustrated in figure 37.

Once this marching process propagates to the downstream boundary of the wake, the next iteration begins with a new flow solution from the panel code with the revised wake geometry. The update of the AIC's and singularity strengths is necessary because the wake displacement modifies the influence of the wake on the wing. This iteration process is repeated until the wake shape converges. Experience with this method has shown that convergence to a qualitatively reasonable wake shape takes three or four iterations, but convergence of the Trefftz-plane drag computation to within 0.25 percent requires approximately 12 iterations.

6.3 Application of Hybrid Wake-Relaxation Scheme

This hybrid wake-relaxation scheme was applied to the $X_t = 1.00$ crescent wing to determine whether the force-free wake could be modeled with sufficient accuracy to allow Trefftz-plane integration for induced drag. The wake was relaxed for 12 iterations to a point 5 semispans downstream. From that point, the wake was extended in the freestream direction for a length of 30 semispans. A comparison of the wake shape produced by the hybrid scheme and the vortex-lattice method is shown in figure 38.

Drag was integrated in a Trefftz plane 15 semispans downstream of the wing. The resulting span efficiency is 0.992, much closer to the expected value. Table 4, gives a comparison of this result with those using the streamwise wake and the vortex-lattice wake models.

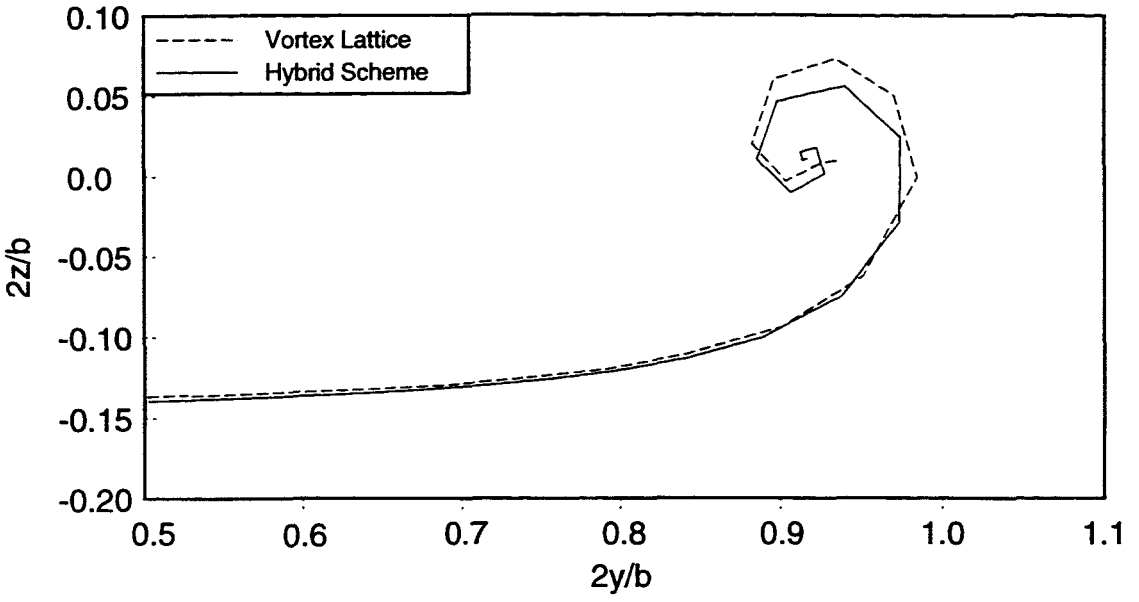

Figure 38. Wake shapes produced by vortex-lattice and hybrid methods.

Table 4. Span efficiency of $X_t = 1.00$ crescent wing, $C_L = 0.30$

Wake	Streamwise	Vortex lattice	Hybrid
e	0.991	1.082	0.992

6.4 Error from Neglecting the u-Perturbation Velocity for Force-Free Wakes

In section 3.1, the reduction of the surface integral to the classical Trefftz-plane contour integral for induced drag with force-free wakes required neglecting two terms involving u-perturbation velocity contributions. The Trefftz-plane drag results presented to this point have all been evaluated on wakes extending in the freestream direction, so the u-perturbation, and its gradient $\frac{\partial u}{\partial x}$, are clearly zero. However, as pointed out in section 3.2, the substitution of the streamwise wake modifies the velocity field in the partition by approximately half the u-perturbation and its gradient, thus modifying the drag computed from the contour integral in the Trefftz plane. The magnitude of the neglected terms and their influence on the Trefftz-plane drag may be assessed by evaluating area integrals in a plane downstream of a typical wing with a force-free wake.

The magnitude of these terms was computed for the $X_t = 1.00$ crescent wing with the accurate force-free wake. The elliptically loaded $AR = 7$ wing at a $C_L = 0.30$ is representative of a typical wing at cruise conditions. An integration grid was established on a plane 3.5 semispans downstream of the wing, with uniform grid spacing of 0.01 semispans. Recall that the force-free wake extends to

a point 5 semispans downstream of the wing. The grid is illustrated in figure 39. The perturbation velocities and perturbation potential were computed at the grid points by the A502 code, and the integrals in equation (38) are evaluated numerically. The value of the $(-u^2)$ integral resulted in a $\Delta C_D = -3.1 \times 10^{-7}$, and the $(\frac{\phi \partial u}{\partial x})$ integral resulted in a $\Delta C_D = 4.5 \times 10^{-6}$. Neglecting these terms in the Trefftz plane integral results in an error in drag coefficient of about 0.1 percent. To verify that the integration region was large enough to capture all of the significant u-perturbation, a second integration was performed on a much larger grid, also shown in figure 39. This required that the grid spacing was much coarser, about 0.035 semispans. The value of the $(-u^2)$ integral on this larger, coarser grid resulted in a $\Delta C_D = -3.5 \times 10^{-7}$, so the first grid appears to have been adequate.

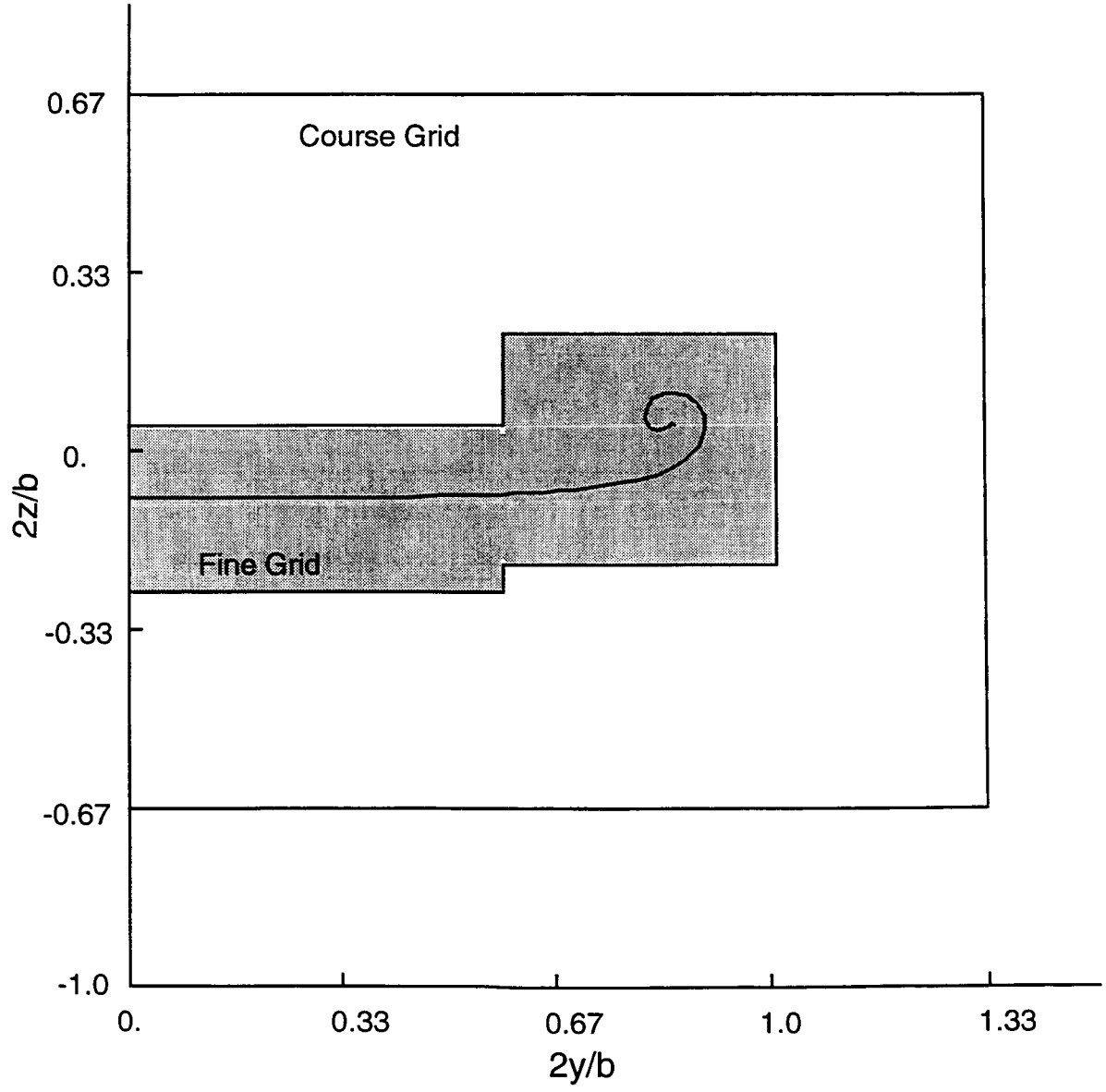

Figure 39. Survey regions for evaluating $\iint -u^2\, ds$ and $\iint \phi \frac{\partial u}{\partial x}\, ds$.

The classical contour integral is not expected to accurately predict the induced drag when the plane is located close to the wing, where the bound vorticity contributes significant u-perturbations. To estimate the magnitude of the $(-u^2)$ integral in close proximity to the wing, the larger integration grid was relocated to a point only 1.0 chord downstream of the trailing edge. The result was a $\Delta C_D = -1.0 \times 10^{-4}$, or about 2.5 percent of the drag. Accurate drag computation on the near-field partition requires evaluation of the complete surface integral, equation (39). The $(-u^2)$ integral was also evaluated on the smaller fine grid at this station, but this time, only the velocity contribution from the wake was included. The result was a $\Delta C_D = -2.4 \times 10^{-6}$, confirming that the large u-perturbation near the wing is primarily due to the bound vorticity on the wing. The fact that the contribution from the wake is still small close to the wing allows the streamwise wake substitution to be made very near the wing without altering the velocities in the partition plane.

6.5 Effect of Streamwise Wake Substitution

The wake substitution hypothesis developed in section 3 indicates that the streamwise wake substitution may be made from a point where the partition meets the downstream extremity of the lifting system. The actual effect of the wake substitution on the computed induced drag was studied for the $X_t = 1.00$ crescent wing. For this wing, the wake was initially relaxed for a length of 5 semispans downstream. From that point, the wake was extended in the freestream direction for a length of 30 semispans. The force-free wake was truncated at various points and replaced with a straight, freestream extension of the wake shape at the truncation point. Trefftz-plane drag integration was carried out at the same plane for each case, 15 semispans downstream of the wing. For each case, the potential-flow problem was re-solved, so any effect of the wake substitution on the bound circulation distribution was included in the analysis. The results listed in table 5 indicate that for this particular planform, the computed drag was not significantly effected by the substitution, even to the point of completely eliminating the force-free wake. This was expected for this planform, since the trailing edge is unswept. The small variation in lift coefficient indicates that there is a slight influence of the wake substitution on the bound circulation. The variation in computed span efficiency for these cases is a measure of the accuracy of the force-free wake model and the numerical integration. Apparently, induced drag may be computed in the Trefftz plane, using the methods employed here, with a precision of about ± 0.25 percent.

Further confirmation of the wake-substitution hypothesis was gained from wake relaxation for the $X_t = 0.25$ elliptical wing. The wake was relaxed for a length of almost 1 semispan downstream (2.32 chordlengths), and extended in the same manner as the previous wake. The Trefftz plane results for this wing are given in table 6. In this case, the traditional wake model, where the wake is a freestream projection of the trailing edge, results in an error of 1.5 percent compared with the force-free wake model. When the force-free wake is replaced with a streamwise wake at a point just downstream of the trailing edge at the wing root, the drag is within 0.5 percent of the value with the full length of

Table 5. Span efficiency vs. force-free wake length for the $X_t = 1.00$ crescent wing

Force-free wake length (chordlengths)	0.0	1.02	2.32	5.61	8.42	12.61
C_L	0.30666	0.30555	0.30553	0.30552	0.30552	0.30552
e	0.991	0.988	0.990	0.988	0.989	0.992

Table 6. Span efficiency vs. force-free wake length for the $X_t = 0.25$ elliptical wing

Force-free wake length (chordlengths)	None	0.1	2.32
C_L	0.30356	0.30169	0.29965
e	0.985	0.975	0.970

force-free wake. The 0.5 percent change is probably due to changes in the bound circulation distribution when the streamwise wake is substituted at the near-field partition, as well as minor errors in the force-free wake model. Although the error associated with the traditional streamwise wake is planform dependent, this result is probably typical for commonly used wing planforms. A 1.5 percent error is acceptable for many engineering predictions of induced drag. The hybrid wake-relaxation scheme successfully models the force-free wake shape for cases where higher accuracy is desired, or when the possibility exists for a high degree of wake interaction. As shown here, only a small portion of the force-free wake must be modeled to gain a significant accuracy improvement over the streamwise wake.

7 PLANAR WING DESIGNS TO EXPLOIT FAVORABLE WAKE INTERACTION

Work by Cone (ref. 8), Lowson (ref. 2), and others has demonstrated that the induced drag of a nonplanar wing is lower than that of a planar wing of the same span and lift. The range of increased span efficiency for various height-to-span ratios are shown in figure 40 for V-shaped dihedral, circular-arc dihedral, and a wing with 90 deg winglet. As discussed in section 3, the wing need not be nonplanar to experience this benefit. When the trailing edge is not straight, it sheds a nonplanar wake when the wing is inclined at an angle of attack, as shown in figure 15. While this effect is small for most wings at the low angle of attack associated with cruise conditions, the effect is amplified at high angles of attack used for climb and/or maneuver. These are often the conditions where induced drag becomes an important design issue.

In this section, two planar wing designs are considered which exaggerate the nonplanar character of the wake. A streamwise wake model is used for initial study, and where sufficient performance benefit is found to warrant further study, a force- free wake is created using the hybrid wake-relaxation method to enable more refined analysis.

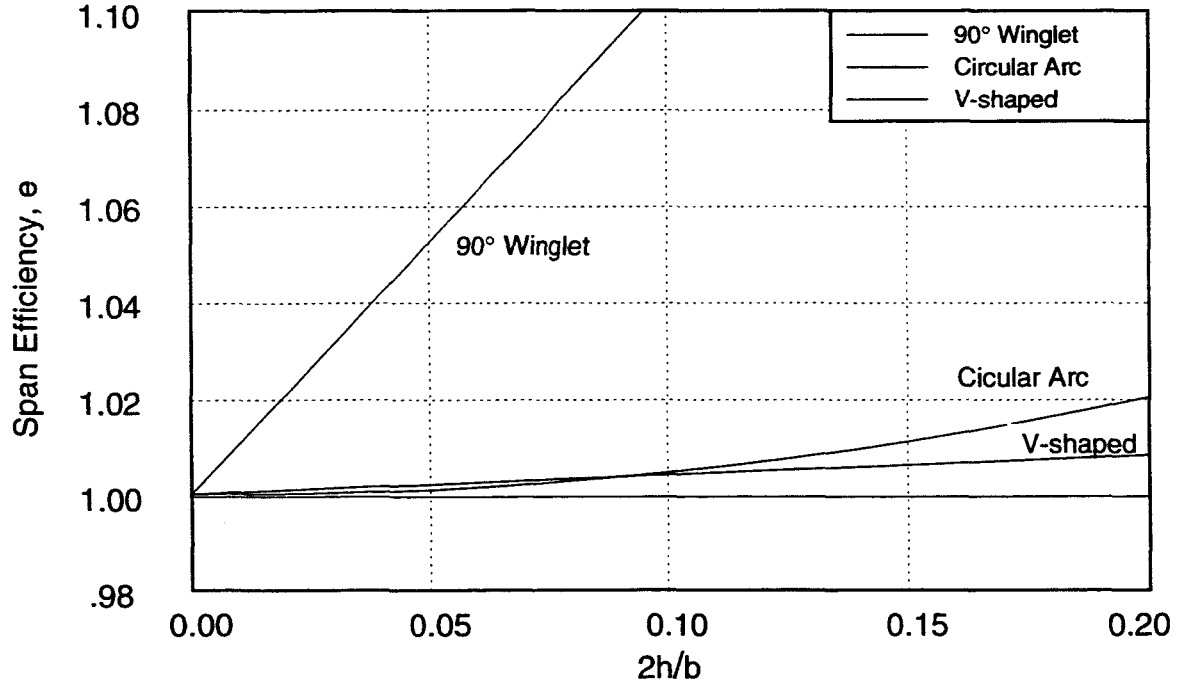

Figure 40. Effect of "spanwise camber" on span efficiency of optimally loaded wings.

7.1 Nonplanar Wake from Planar Wing with Forced Side-Edge Separation

A typical wing analysis using linear panel methods assumes that the wake sheds only from the trailing edge. In reality, there is often some degree of separation on the side edge of the wingtip. The vorticity shed from the side edge forms a wake that is nonplanar, even in close proximity to the trailing edge, as shown in figure 41. The structure of this side-edge vortex formation has been studied extensively, experimentally by Chow and Zilliac (ref. 46) and computationally by Srinivasan (ref. 47). The characteristics of a wing with this side-edge separation may be analyzed with panel methods by prescribing a wake attached to the wingtip side edge. While the exact location and character of the separation may be difficult to define for typical, well-rounded tip shapes, an approximate wake shape will give some indication of whether the induced drag is influenced by the side-edge separation. Further, a wingtip with a sharp side edge or chine may be designed which produces a specific separation pattern (ref. 48).

The nonplanar character of the wake can be exaggerated by forcing the flow around the wingtip side edge to separate almost immediately behind the leading edge. The streamwise wake shed from this wing replicates the wake shed from a wing with a winglet, as shown schematically in figure 42. If the side edge is angled slightly, this corresponds to a winglet with less than 90 deg dihedral. For an $AR = 6$ wing, a height-to-semispan ratio, 2h/b, of 0.05 is obtained at an angle of attack of 8.5 deg. A streamwise wake shed from the 5 deg angled side edge corresponds to a winglet with 72 deg dihedral.

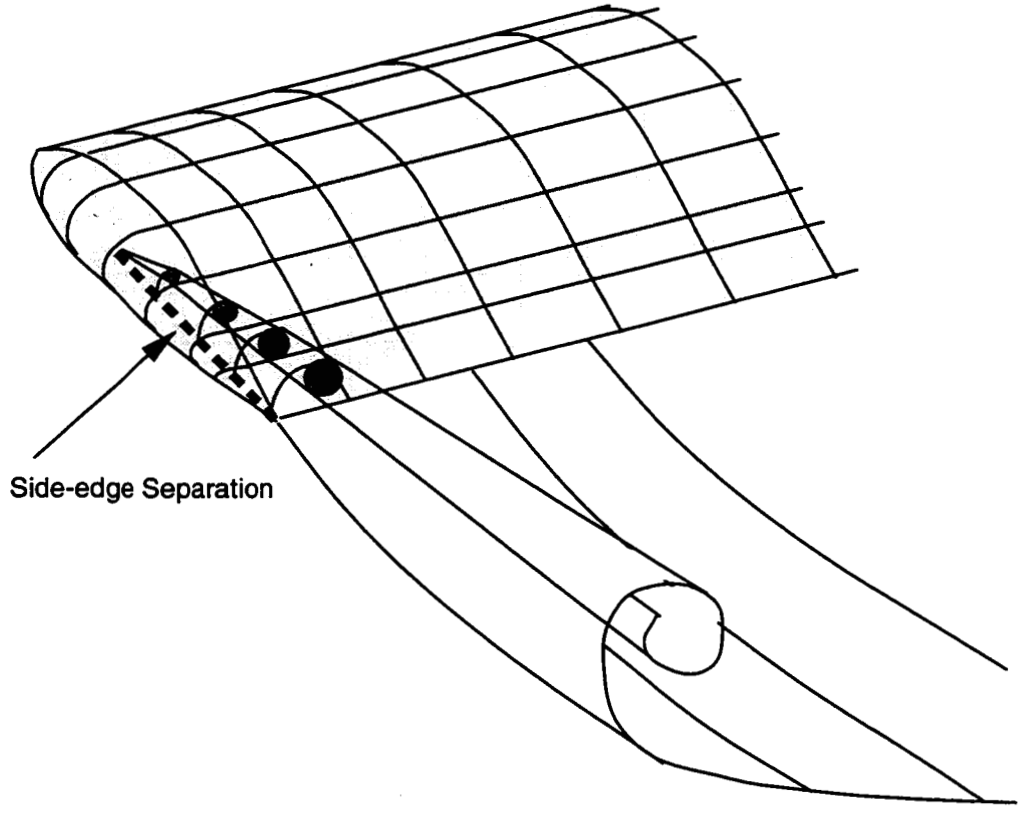

Figure 41. Trailing wake produced by side-edge separation.

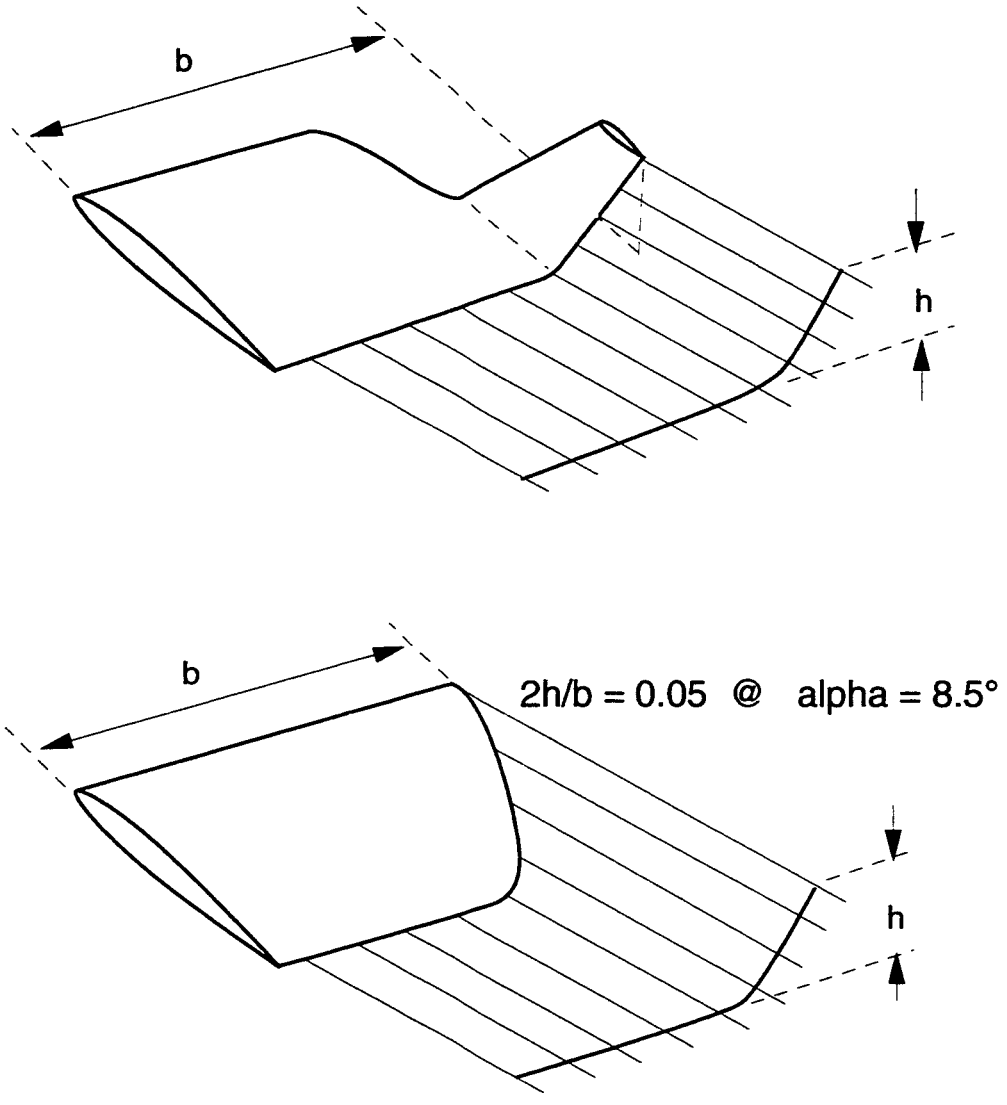

Figure 42. Nonplanar wake from planar wing resembles wake from winglet.

As in the case of the wing with winglet, the optimal span loading is no longer elliptical. Compared to an elliptical loading, more load must be carried on the outboard portion of the wing. The span loading may be controlled by twist, camber, or planform shape. For this wing design, twist, and to some degree, camber seem to be poor choices for increasing the lift load near the tip, since these would produce higher section lift coefficients near the tip, leading to undesirable tip stall. On the other hand, increasing the chord near the tip maintains moderate section lift coefficients while producing greater wake height.

The optimal loading for a wing with 72 deg winglet was found using the discrete-vortex collocation method of Kroo (ref. 49). The discrete-vortex method predicts a span efficiency of 1.04 for this wing, compared with 1.01 for the elliptically-loaded planar wing. This optimal span loading was used as a guide to shape an analytical function to describe the planform of a planar wing with the side-edge separation modeled. A combination of "super-ellipse" functions defines most of the wing shape, with an additional tangent function to describe the angled wingtip side edge. The best span loading obtained with this analytical planform definition is from the wing shown in figure 43, referred to as Planform A. The analytical functions describing this wing are given below.

$$X_{le}(\eta) = X_t(1 - (1 - \eta^4)^{0.25}), X_t = 0.015$$

$$Chord(\eta) = min \begin{cases} C_r(0.75(1-\eta)^{10})^{0.1} + 0.25(1 - \eta^{1.15})^{0.87}), & C_r = 0.94 \\ C_t + (1 - \eta)\tan(1.48), & C_t = 0.05 \end{cases}$$

Figure 44 shows the span loading achieved on this wing compared with an elliptical loading and the "target" loading from the discrete-vortex optimization. A summary of the computed span efficiency for Planform A is shown in table 7. The result from the $X_t = 1.0$ crescent wing is provided for comparison as an elliptically-loaded planar wing.

The span efficiency is expected to be dependent on angle of attack, since the effective wake height varies with angle of attack. While it appears that this mechanism for increasing span efficiency is working to some extent, only about 1.0 percent improvement over the elliptically-loaded planar wing has been achieved. Figure 44 indicates that the target span loading has not been obtained near the wingtip. The strong downwash induced by the tip vortex trailing along the wingtip side edge makes it difficult to develop the required lift loading.

To achieve a span loading closer to the optimum, a second planform was developed with a piecewise linear chord distribution. The chord distribution for this wing, referred to as Planform B, is given in table 8, and the wing is shown in figure 45.

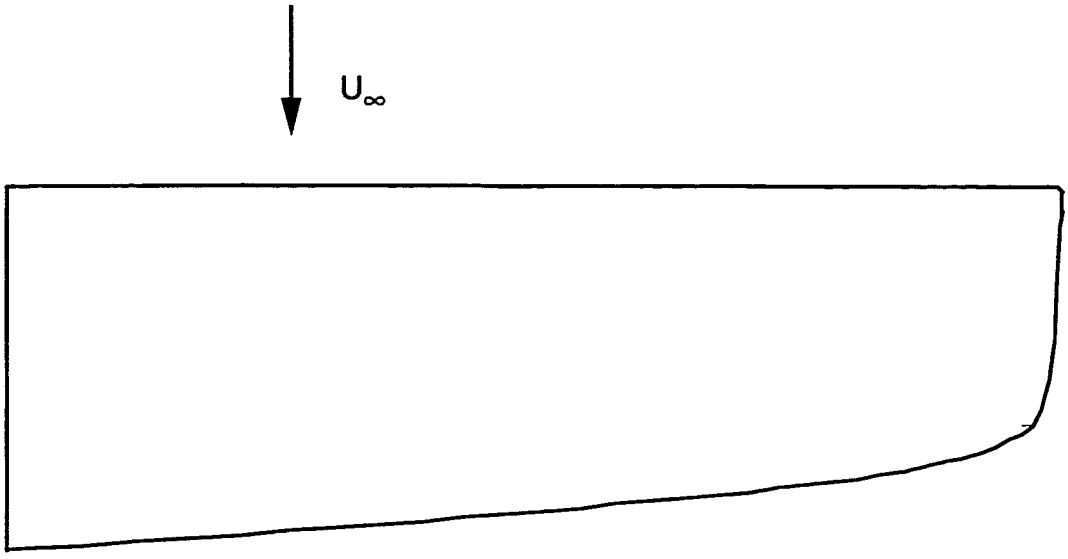

Figure 43. Planform A.

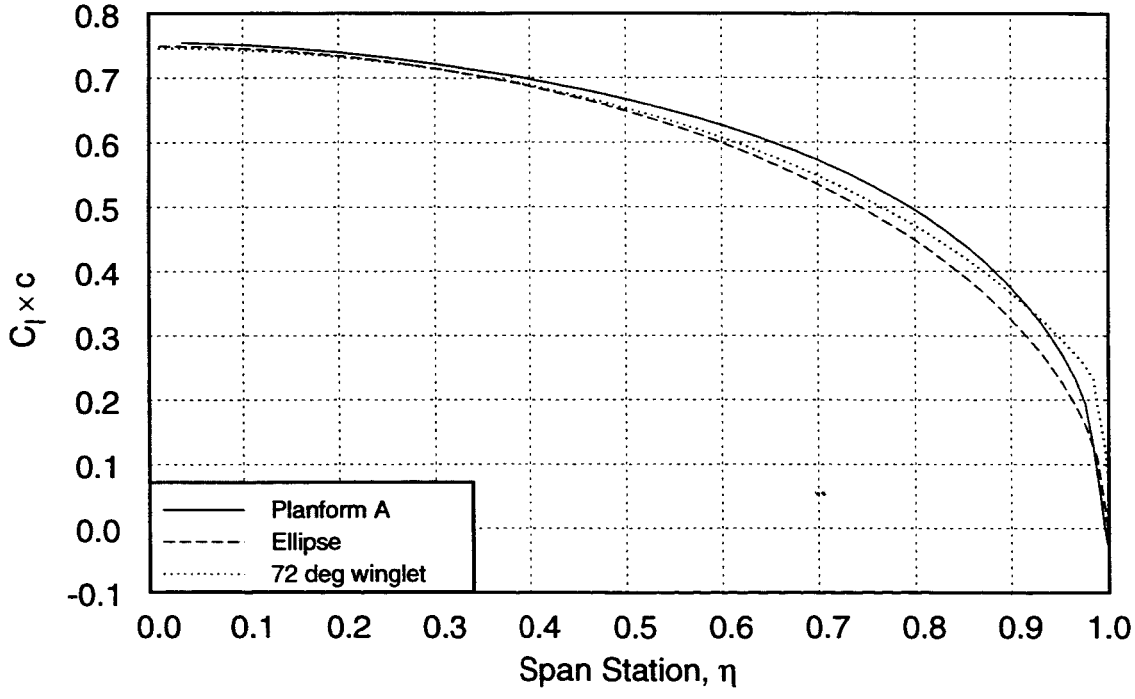

Figure 44. Spanwise lift distribution for Planform A.

Table 7. Span efficiency of Planform A compared with the $X_t = 1.0$ crescent wing

Planform	Angle of attack	e
A	3.0°	0.985
A	8.5°	0.9996
$X_t = 1.0$ crescent	4.0°	0.990

Table 8. Chord distribution of Planform B

Span station (η)	0.0	0.4	0.84	0.967	0.98	0.987	1.0
Chord	0.94	0.89	0.685	0.71	0.69	0.65	0.05

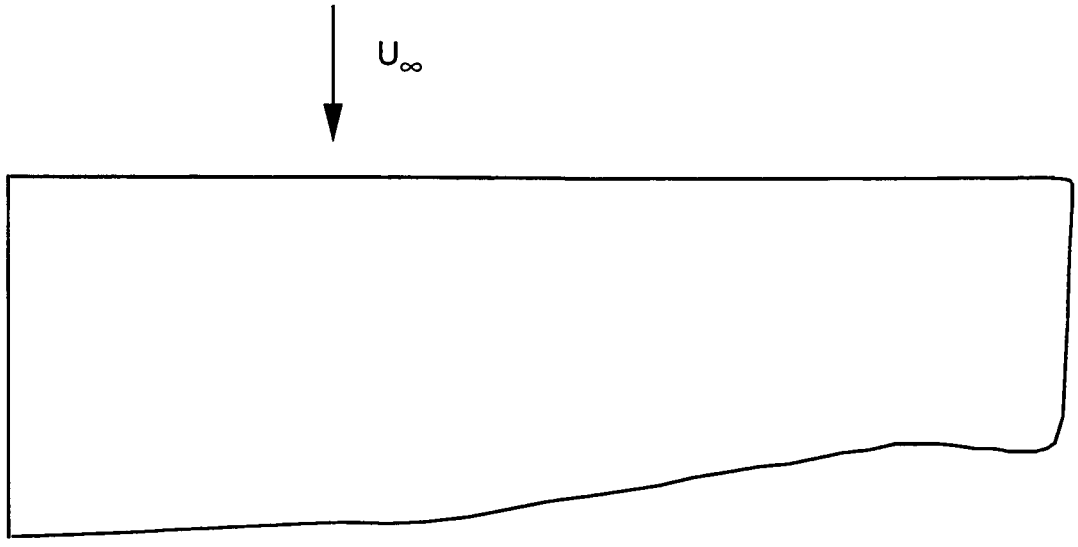

Figure 45. Planform B.

The spanwise lift distribution for Planform B is shown in figure 46, compared with the elliptical and target distributions. This wing produces a span loading somewhat closer to the target, but is still unable to develop the desired lift load in the immediate vicinity of the tip, due to the large downwash produced by the nearby tip vortex. The computed span efficiency for Planform B is given in table 9. As further confirmation that the nonplanar wake shedding from the side edge is responsible for the increased span efficiency with increased angle of attack, the 8.5 deg angle case was re-analyzed with the wingtip side edge modeled with attached flow. The downstream "corner" of the wingtip was shifted outboard so that the wake would extend along the full wing span. This result is included in table 9.

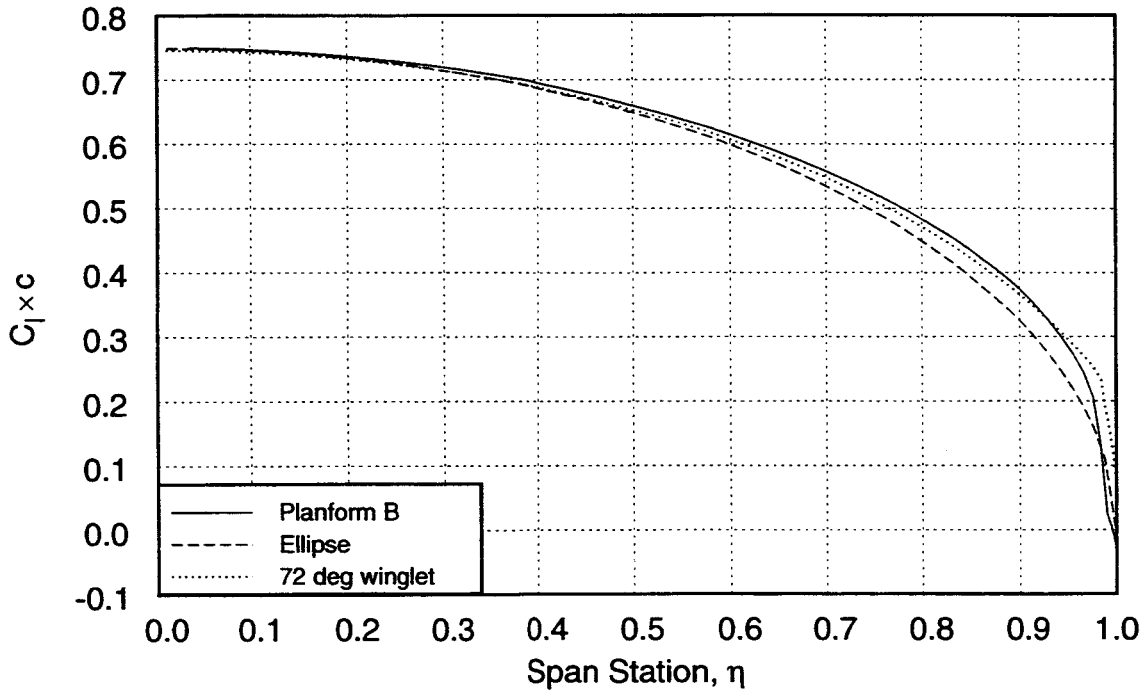

Figure 46. Spanwise lift distribution for Planform B.

Table 9. Span efficiency of Planform B

Angle of attack	Span efficiency, e
2.5°	0.984
5.0°	0.994
8.5°	1.0044
8.5°, w/ attached side-edge flow	0.984

The span efficiency of Planform B is slightly better than Planform A, demonstrating almost 1.5 percent improvement over the elliptically-loaded planar wing at high angle of attack. The variation of span efficiency with angle of attack, and the loss of span efficiency when the side-edge separation is removed, confirm that the wake shedding from the wingtip side edge is responsible for the improvement. But the benefit is only about half of the anticipated 3 percent. These results are not promising enough to warrant further study with a more accurately modeled wake shape.

In the case of a wing with a winglet, the winglet provides the lifting surface necessary to produce the optimal lift load near the tip, and relocates the shed vorticity away from the wingtip, reducing the downwash. Without the contribution from the actual winglet, it does not appear possible to achieve an equivalent wake shape and circulation distribution.

7.2 Nonplanar Wake from Planar Split-Tip Wing

A second concept for developing a highly nonplanar wake is the split tip arrangement shown in figure 47. While "tip sails" and other types of split tips have been studied by Zimmer (ref. 1) and others, they have typically inclined the tips at various dihedral angles. The planform presented here is planar. It has been designed with the specific goals of producing a highly nonplanar wake at angles of attack,

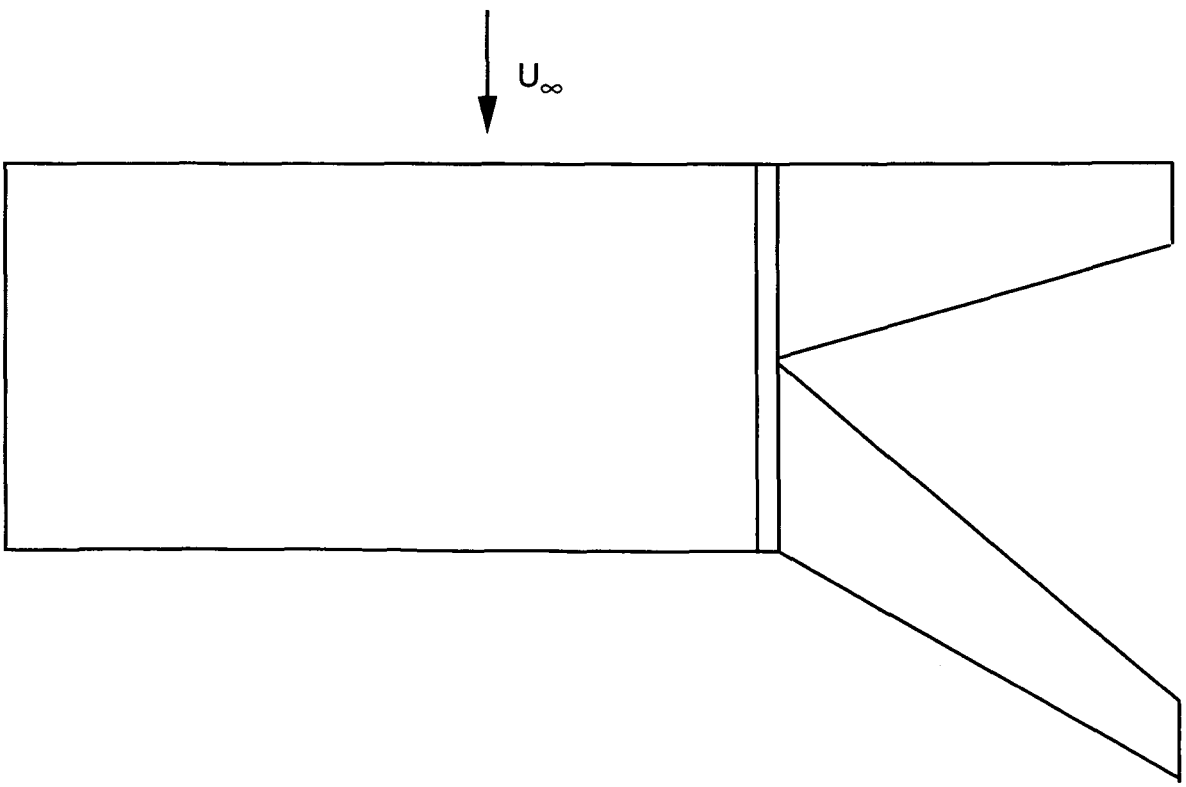

Figure 47. Split-tip planform.

and promoting interaction between the aft tip and the tip vortex shed by the forward tip. The split-tip planform was analyzed with the discrete-vortex method, LinAir (ref. 34), to get a quick, preliminary estimate of span efficiency. At 9 deg angle of attack, the span efficiency predicted by the discrete-vortex method was e = 1.066.

A complete panel model of the wing was developed to allow analysis with the A502 panel code. The main portion of the wing, and the two tip surfaces are lofted with symmetrical NACA 0012 airfoils with no twist. A blended fairing provides a smooth transition from the main wing surface to the tip surfaces, as shown in figure 48.

The initial analysis of the split-tip wing was performed with a traditional streamwise wake model. A streamwise wake shed from the trailing edge of the forward tip would impinge on the upper surface of the aft tip, so its shape was modified slightly to follow approximate streamlines over the surface until free to trail in the freestream direction without intersecting the surface. The inboard edge of this wake was abutted to the upper surface of the wing, modeling an attached flow where the wake follows the upper surface to the wing trailing edge. The trace of this streamwise wake model in the Trefftz plane, shed from the split-tip planform at 9 deg angle of attack is shown in figure 49. The height-to-semispan ratio of this wake is 0.073, despite the fact that the wing itself is planar. The computed span efficiency for this wing with the streamwise wake model is 1.048.

According to the hypothesis developed in section 3, streamwise wake substitution at a near-field partition can be made only as close as the trailing edge of the aft tip. This leaves a significant portion of the wake trailing from the forward tip and passing over the aft tip surface that must be accurately modeled as a force-free wake. Substitution of this portion of the wake with a streamwise wake is expected to produce some error in Trefftz-plane drag. The fact that the streamwise wake model indicates such a high span efficiency is promising enough to warrant a more realistic analysis with a force-free wake model.

The split-tip geometry poses several challenges to the wake relaxation method. A portion of the wake from the forward tip passes very close above the upper surface of the aft tip. The abutment of this wake with the upper surface of the wing must be free to seek its equilibrium location. From that point, the wake must merge with the wake trailing from the wing and aft tip. The close interaction of the forward wake with the wing surface requires that the velocities induced by the wing surface be very accurate; otherwise the wake may inadvertently penetrate the surface. The strong velocity singularities of discrete-vortex and low-order panel methods would make successful wake relaxation unlikely. The hybrid wake-relaxation scheme described in section 6 is well-suited for these problems. The high-order panel method used with the hybrid scheme provides smooth, continuous velocities near the wing surface. The viscous core model allows the two wake sheets to merge without nonphysical orbiting of the vortex filaments.

The hybrid wake-relaxation scheme was used to create a force-free wake model for the split-tip wing at an angle of attack of 9 deg. Sixteen iterations of the method were used to relax the wake to a point

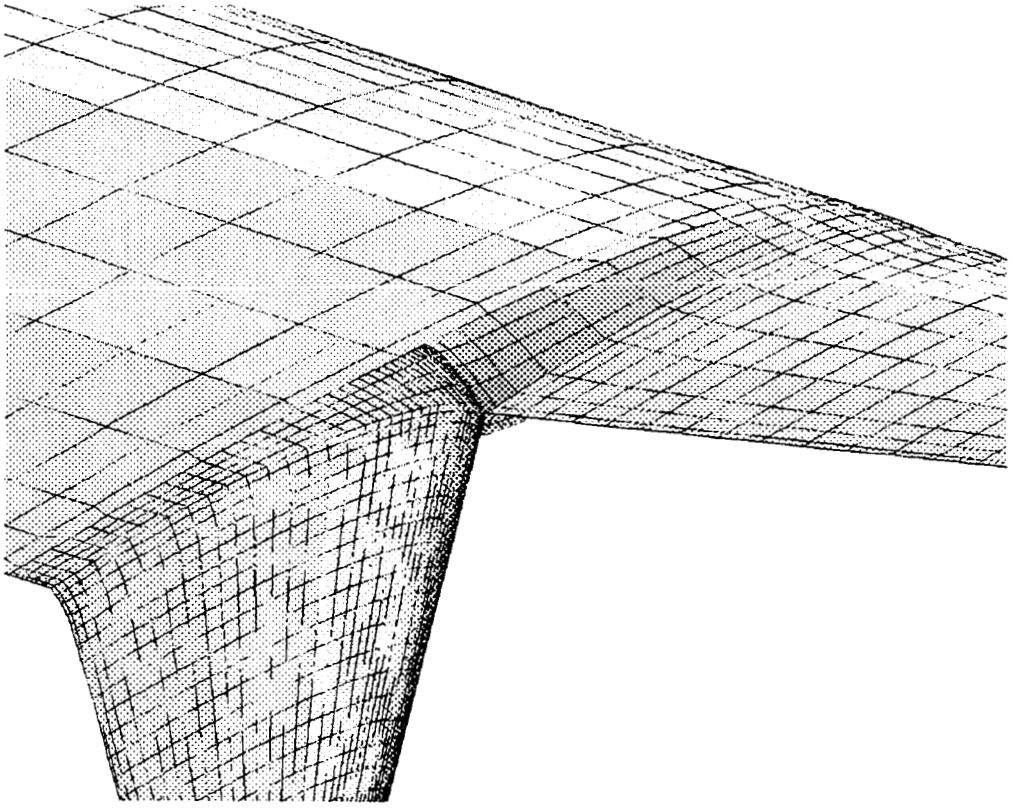

Figure 48. Detail of split-tip junction region.

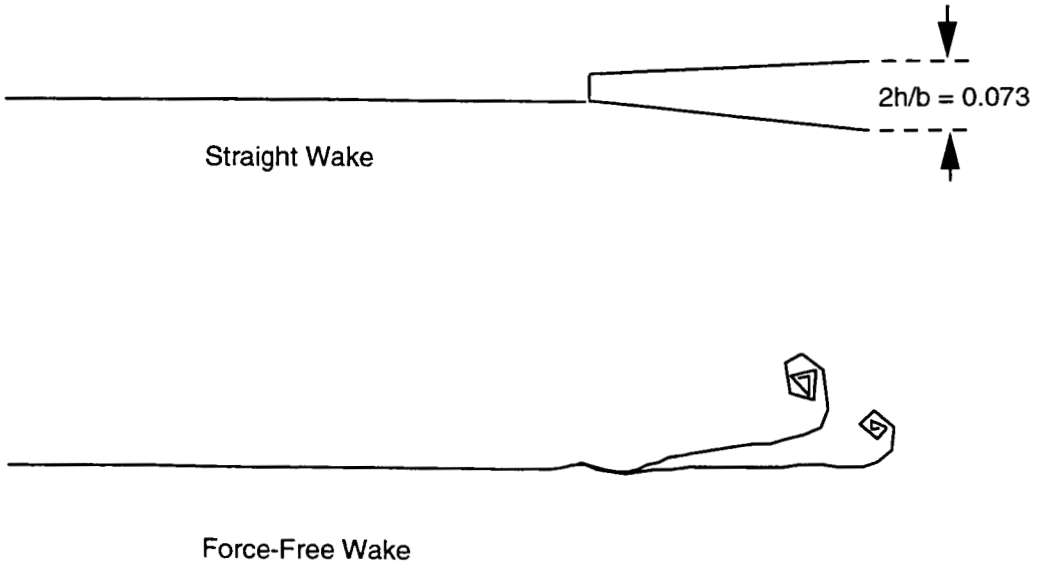

Figure 49. Wake shapes modeled for the split-tip wing.

2 chordlengths downstream of the trailing edge. From that point, the wake was extended straight in the freestream direction for 30 semispans. The trace of this wake in the Trefftz plane is shown in figure 49. A few details of the structure of the wake are shown in figure 50. Following the same methods used in section 4, this wake geometry was used to produce a panel model of the split-tip wing and wake for analysis with the A502 high-order panel code. Trefftz-plane drag integration on this wake produced a span efficiency of e = 1.1133. To confirm that the wake shape from the hybrid scheme was thoroughly converged, the same analysis was repeated on the wake from the 15th iteration. This wake produced a span efficiency of e = 1.1149, a difference of less than 0.2 percent. Table 10 gives a summary of the computed span efficiency for the split-tip wing with various analysis methods and wake models.

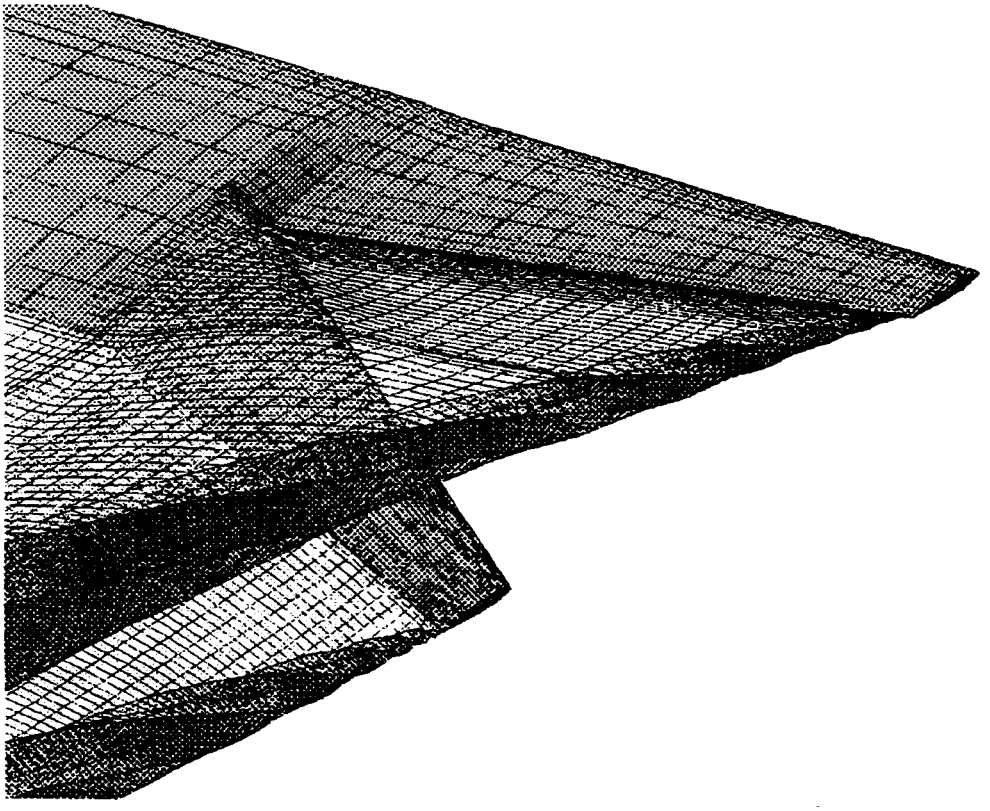

Figure 50. Force-free wake computed by hybrid wake scheme for split-tip wing.

Table 10. Predicted span efficiency of the split-tip wing

Analysis method	Wake model	e
Discrete vortex	Streamwise	1.066
High-order panel	Streamwise	1.048
High-order panel	Force-free	1.113

These results indicate that it is possible to produce a span efficiency greater than 1.0 with a planar wing, by promoting a highly nonplanar wake shape. But more importantly, these results exhibit significant nonlinear wake interaction, evident from the 6 percent increase in span efficiency predicted with the force-free wake compared with the streamwise wake. The force-free wake from the forward tip interacting with the aft tip surface apparently changes the circulation distribution and/or wake velocities in a manor not captured by the traditional streamwise wake model. Experimental confirmation of these results is discussed in section 8.

8 EXPERIMENTAL STUDIES OF THE ELLIPTICAL AND SPLIT-TIP WING PLANFORMS

The predicted performance of the split-tip wing presented in section 7 represents a 12 percent reduction in induced drag compared with an elliptically-loaded planar wing. The computational tools used to make these predictions have been validated by good agreement with expected results for other geometries, under circumstances where other methods have given poor results. Every attempt has been made to obtain model-independent solutions to the inviscid governing equations and boundary conditions. Nevertheless, these results are surprising and should be regarded skeptically until confirmed by experiment.

Of course, induced drag cannot be measured directly by experiment. However, the experiment can be designed to obtain an approximate increment in induced drag between two wing configurations by comparing the drag of wings with the same span and wetted area. An estimate of the actual induced drag can be obtained by subtracting an estimate of the viscous drag from the measured total drag. The viscous drag estimate may be based on airfoil section data. In addition, wake survey techniques may be used that allow decomposition of experimental drag measurements into induced and viscous components (ref. 24).

An experimental investigation of the induced drag of the split-tip wing and a classical elliptical wing ($X_t = 0.25$) was conducted as part of this study. Obtaining experimental drag measurements to within 1–2 percent accuracy is difficult, especially with the facilities available for this study. Unusually careful experimental techniques were required to obtain force measurements of acceptible accuracy. This section describes the test procedures, data analysis, and results of the experiment.

8.1 Model Description

Two wind tunnel models were constructed to test the elliptical and split-tip planforms. Both wings have a 6.0 ft span and 5.4 ft^2 of planform area. The model dimensions are shown in figure 51. Both wings were lofted with NACA 0012 airfoil sections, without twist. Untwisted, uncambered wing designs were chosen to aid in data interpretation. For these wings, the lift is zero at zero angle of attack, so that any error in flow angularity in the tunnel may be measured. In addition, since there is no twist, there is no induced drag at zero lift, simplifying the drag decomposition. In order to create enough volume in the wing to house the internal force balance, the center section of each wing was thickened slightly using an NACA 0015 airfoil. The thickened area was smoothly blended to the 12 percent thick section over 3 in. of span.

The elliptical wing was machined from a single piece of aluminum. The forward and aft tip surfaces and the main wing surface of the split-tip wing were individually machined from aluminum, and joined with short steel internal spars. The wing surface contours were maintained to within 0.003 in., and sanded smooth with 400-grit carborundum paper, producing an (approximately) 8-microinch finish.

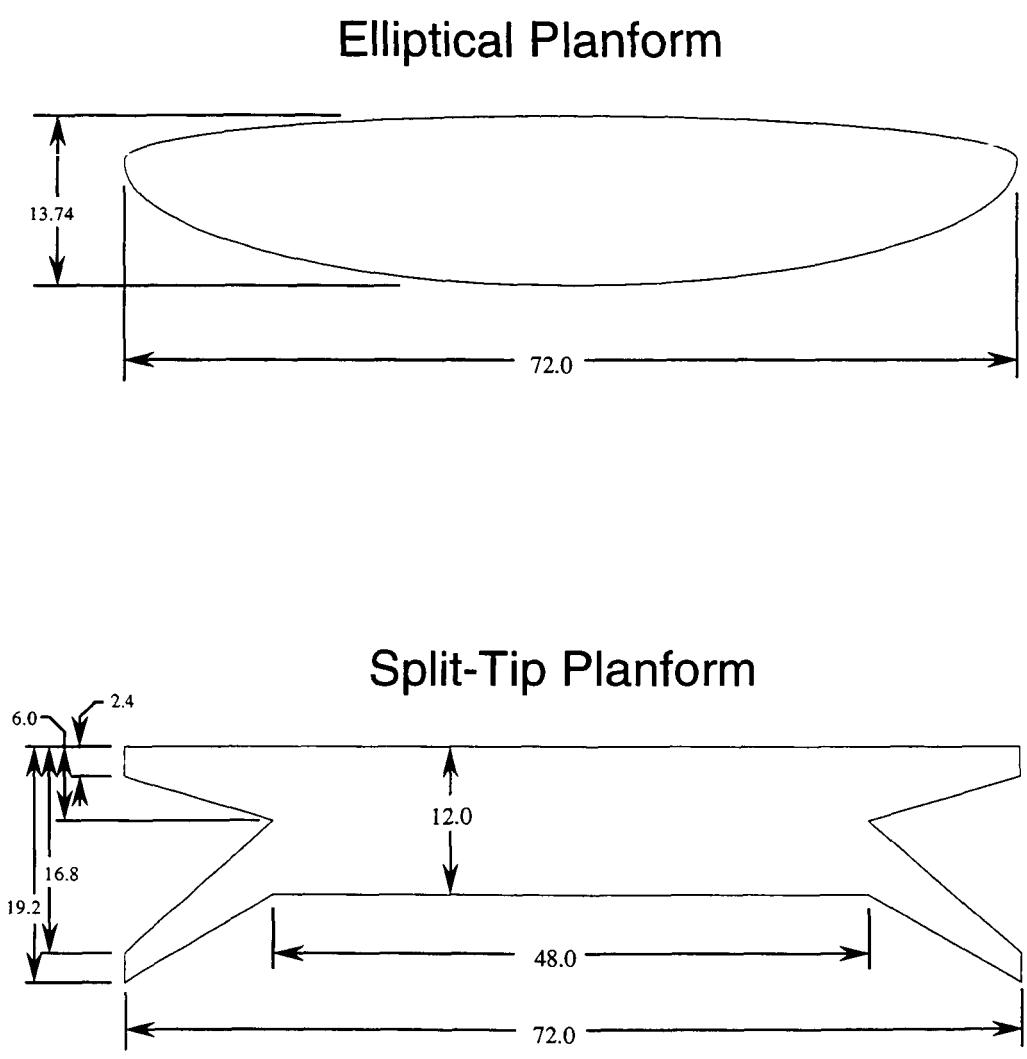

Figure 51. Elliptical and split-tip model dimensions.

The leading edge regions were further sanded with 600-grit carborundum paper, producing an (approximately) 4-microinch finish. The transition fairings were shaped from high-density PVC foam and finished with enamel. Flush-fitting cover plates were used to fair over the balance cavity and inclinometer cavity in the wings, and all instrumentation wiring was routed internally. The models were designed to withstand a dynamic pressure of 100 psf at a lift coefficient of 1.5, with a safety factor of 5.0.

8.2 Test Facility

Both models were tested in the Ames 7- by 10-Foot Low Speed Wind Tunnel. This facility is an atmospheric, return circuit wind tunnel with a single stage 1400-horsepower fan and a fresh-air exchanger. The flow quality in the test section has been documented by Wadcock (ref. 50). The flow quality assessment identified rather poor quality flow, containing a very low frequency ($\tau \approx 23$ sec) periodic swirl and axial velocity variation, and a stream angle of about 0.3°. The poor flow quality required special care to insure sufficient data quality for this experiment. This issue is discussed in sections 8.8 and 8.10.

The wings were mounted on a cylindrical post with a thin blade-type strut and a pitch link. Figure 52 shows details of the model support strut. The blade cross-section was an NACA 0012 airfoil. The model support located the wings approximately 6 in. above the tunnel centerline, oriented

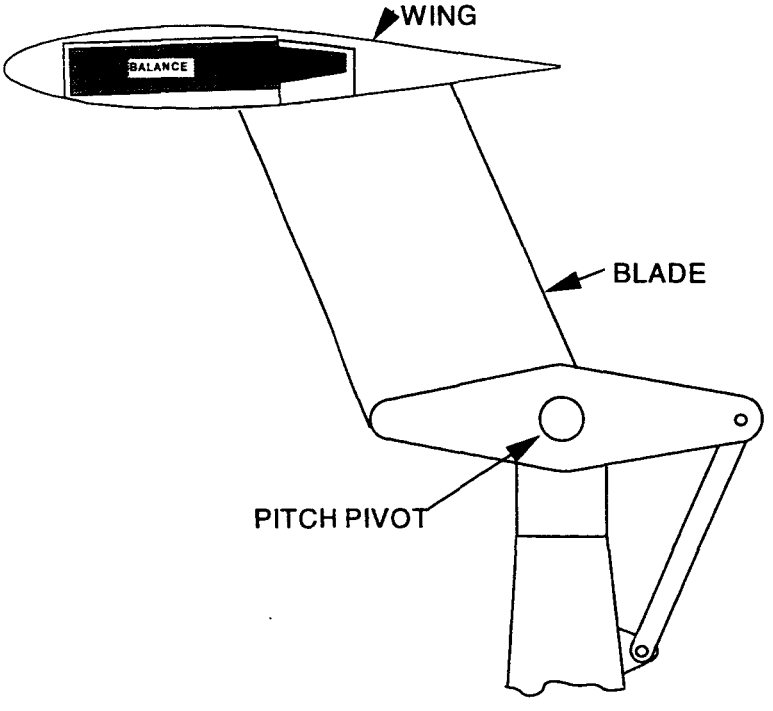

Figure 52. Model support system.

horizontally so that the 6 ft wingspan was centered in the 10 ft test section width. The end of the model support blade was contoured to fit the undersurface of the wings with a constant 0.075 in. gap to prevent "fouling" contact between the model support and the model.

The Ames 7- by 10-Foot Wind Tunnel is equipped with a 3-axis traversing survey apparatus, which was used to make high-resolution surveys of the flowfield downstream of the wings. The operation and function of the survey apparatus is described by Shoemaker (ref. 24).

8.3 Instrumentation

The models were instrumented with a 6-component internal strain-gage force balance. The contours of the wings were designed so that the entire balance was enclosed inside the wing, with no fuselage or other fairing, except the slight thickening of the airfoil to 15 percent from 12 percent thickness. A Task 1.0 in. mk. III balance was used. The measurement capacities of the mk. III balance are given in table 11. The capacity of the balance was suitable for testing the wing models at a dynamic pressure of 100 psf, with the exception of the rather low rolling moment capacity. The poor flow quality documented by Wadcock (ref. 50) was expected to produce substantial unsteady roll moments on the model, which would limit the allowable dynamic pressure. Unfortunately, the low rolling moment capacity is a necessary consequence of selecting a balance small enough to fit entirely within the contours of the wing.

Table 11. Task mk. III balance capacity

Forward normal force (N1)	400 lb
Aft normal force (N2)	400 lb
Axial force (A)	150 lb
Forward side force (S1)	200 lb
Aft side force (S2)	200 lb
Roll moment (RM)	21 ft-lb

The cylindrical outer sleeve of the balance, called the "metric" side, is fitted to a steel balance housing that fits into a cavity in the underside of the wing. The same balance housing was used for both wings. The balance was pinned to the housing with a single balance pin located in the forward, bottom pin hole of the balance. The "non-metric" inner rod of the balance was fitted to a tapered socket on the top of the steel model support blade The balance instrumentation wiring was led through the back of the socket down to a channel in the model support blade, so there was no bridging of the balance wiring across the break from the metric portion to the non-metric portion. Figure 53 shows a cross section of the balance installation in the wing.

The models were also fitted with an internal inclinometer to measure the model angle of attack. The benefit of an internally mounted inclinometer is that the angle of attack measurement is not affected by

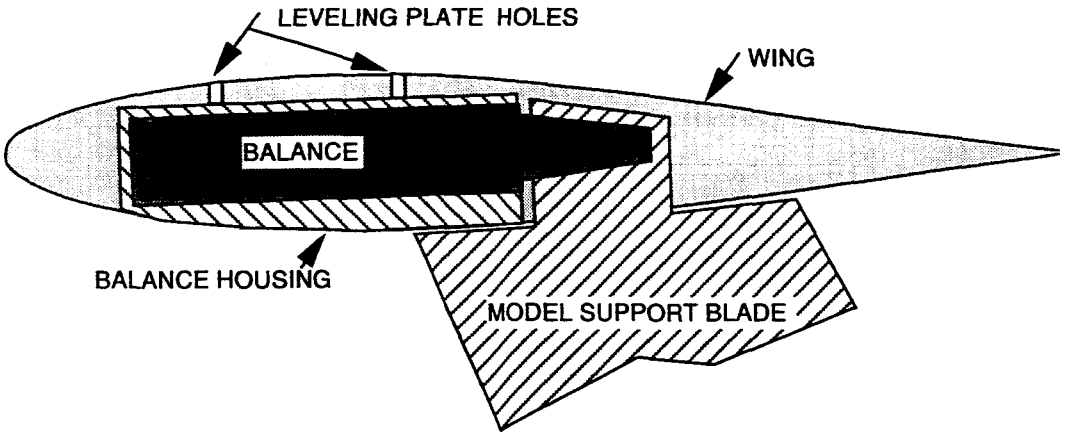

Figure 53. Balance installation detail.

deflection of the model support or force balance under aerodynamic load. One potential disadvantage of an internally-mounted inclinometer is that it is subjected to inertial excitation by the small motion of the model during testing. In certain cases, especially involving propulsion simulation, high-frequency excitation (e.g., from jet turbulence) can degrade the accuracy of the inclinometer. Past experience with internal inclinometers during low speed aerodynamic tests has demonstrated that this is not a problem for this type of testing. In these cases, good agreement with an external angle measurement was observed (ref. 51).

A Schaevitz $\pm 15°$ inclinometer was mounted in a cavity located 9 in. left of the wing centerline. The inclinometer wiring was led through a channel to the balance cavity and routed down the model support along with the balance wiring. The inclinometer wiring did bridge the metric break, so care was taken to locate the wiring to produce a negligible force tare. The external wiring sheath and shielding was removed to minimize the bending stiffness of the four individual 32 gage wires.

A seven-hole cone probe was used to survey the flowfield downstream of the wings. A ± 1.0 psid Pressure Scanning, Inc., 48-port pressure-transducer module was used to measure the cone-probe pressures.

Other instrumentation included flow measurements of the tunnel total pressure and temperature measured in the settling chamber upstream of the test section, and tunnel static pressure measured with orifices located at the upstream edge of the test section.

8.4 Calibrations

The Task 1.0 in. mk. III balance was calibrated by the NASA Ames Research Center's Balance Calibration Laboratory, using the hand-loading method. A complete 6-component calibration was performed, including positive and negative loadings of each gage, combined loadings and a full interaction calibration. The calibration repeatability was approximately 0.02 percent of full scale for each primary gage and for the gage interactions. Interactions refer to the unintended gage output on other gages

resulting from loading of a primary gage. For example, if the forward normal force gage is loaded, a small output will result in the aft normal force gage, the axial gage, and the side-force gages. The Task balance is designed to minimize these interactions, but in many cases, interactions as large as 3 percent of the applied load are found. These interactions must be carefully calibrated to achieve high accuracy force measurements with the balance. A matrix of calibration constants is supplied to the data reduction program from the Calibration Lab. During installation in the 7- by 10-Foot Wind Tunnel, check loadings of the normal force and axial force gages were performed. This check loading provides an end-to-end check of the balance installation, and signal conditioning to the data acquisition system to insure that the installation reproduces the balance calibration. The balance check loadings agreed with the calibration within 0.5 percent, which is considered satisfactory given the less accurate leveling ability of the model support system compared with the Calibration Lab.

The Shaevitz inclinometer was calibrated "in-situ" for each wing, using a Hilger & Watts microptic clinometer, resting on a leveling plate fit to the wing. The leveling plate legs fit through holes in the wing upper surface and bear directly on the balance housing. In this way, the inclinometer was calibrated to measure the angle of the balance housing directly. The accuracy of the microptic clinometer is traceable to 15″, or 0.004°. A third-order polynomial fit of the calibration data is supplied to the data reduction program. Angle checks were performed to ensure that the data reduction program correctly computes the angle of attack from the calibration. The results of the angle checks demonstrated that the angle of attack measurements are accurate to within 0.007°.

The set-up, calibration, and use of the PSI module to measure the cone- probe pressures is described by Shoemaker (ref. 24).

Tunnel total and static pressure measurements were used to compute the test section dynamic pressure. A standard empty-tunnel calibration of this instrumentation for dynamic pressure measurement was included in the data reduction program. The empty tunnel calibration was performed as part of the flow quality assessment of the Ames 7- by 10-Foot Wind Tunnel by Wadcock (ref. 50).

8.5 Instrumentation Error in Drag Measurement

The error in measurement of normal force, axial force, and angle of attack each contributes to the error in the resolved lift an drag forces. The resolution of balance forces into lift and drag is given by:

$$L = N\cos\alpha - A\sin\alpha \tag{49}$$

$$D = N\sin\alpha + A\cos\alpha \tag{50}$$

where α is the angle of attack, measured between the balance axis and the freestream, and N and A are the normal and axial force components.

The differentials of the lift and drag are:

$$\delta L = \delta N \cos\alpha - N \sin\alpha \delta\alpha + \delta A \sin\alpha + A \cos\alpha \delta\alpha \tag{51}$$

$$\delta D = \delta N \sin\alpha + N \cos\alpha \delta\alpha + \delta A \cos\alpha - A \sin\alpha \delta\alpha \tag{52}$$

Eliminating higher order terms for small angles,

$$\delta L = \delta N + \delta A\alpha + A\delta\alpha \tag{53}$$

$$\delta D = \delta N\alpha + N\delta\alpha + \delta A \tag{54}$$

The measurement accuracy of Task balances calibrated and installed following the standard procedures at NASA Ames is claimed to be ±0.5 percent of reading or ±0.2 percent of full scale (F.S.), whichever is less. This accuracy level is consistent with the results of the balance check-loadings performed before and after this experiment. The demonstrated accuracy of the Shaevitz inclinometer used in this experiment is 0.007° (0.00012 rad). These measurement uncertainties produce an uncertainty in lift and drag measurement that varies with the actual force levels and angle of attack. The uncertainty in lift and drag measurement is evaluated here for a representative example with an angle of attack of 5° (0.087 rad) and a dynamic pressure of 45 psf. The normal force is approximately 100 lb, and the axial force is approximately −5 lb, so the uncertainty in these measurements is $\delta N = 0.5$ lb and $\delta A = 0.025$ lb. Substituting these values into equations (53) and (54) gives:

$$\delta L = 0.5 + (0.025)(0.087) - (5.0)(0.00012) = 0.5\text{lb} \tag{55}$$

$$\delta D = (0.5)(0.087) + (100)(0.00012) + 0.025 = 0.043 + 0.012 + 0.025 = 0.080\text{lb} \tag{56}$$

The lift and drag for this example are 100.1 lb and 3.73 lb, so the uncertainties in lift and drag due to balance measurement uncertainties are expected to be to 0.5 percent and 2.1 percent. Note that the uncertainty in lift results almost entirely from the uncertainty in normal force measurement, whereas the uncertainty in drag results from the uncertainty in normal force, axial force, and angle of attack, in roughly equal proportions. The presence of the middle term, $N\delta\alpha$, in the drag uncertainty highlights the importance of precise angle measurement, because the normal force is typically very large. This term contributed little to the drag uncertainty in this example because a high level of angle measurement accuracy was achieved. However, the limitation of dynamic pressure to 45 psf (see section 8.7) led to a reduction in the achievable accuracy. Since only about half the normal force capacity was used, the accuracy of the balance measurements was less than would be achieved with a more appropriately sized balance. It is also important to note that these uncertainties are primarily due to bias error in the calibration and test setup. The repeatability of measurements is generally much better than these uncertainties would indicate, provided careful sampling techniques are used. These techniques will be discussed in sections 8.6 and 8.8.

8.6 Data Acquisition and Reduction

This experiment employed the NASA Ames Standardized Wind Tunnel System (SWTS) for data acquisition and reduction. At the Ames 7- by 10-Foot Wind Tunnel, this system consists of Pacific amplifier/filters, a Teledyne analog-digital converter, and a Digital Equipment PDP 11/40 computer. The amplifier/filters provide excitation voltage, and filter and amplify the analog outputs from the balance and other transducers. The amplifier/filters were set to filter the balance signals with a 1 Hz low-pass filter to eliminate as much dynamic character as possible from the balance measurements. The analog-digital converter spans the $\pm$ full scale measurement capacity of each instrument into 9830 digital counts. For example, the resolution of the axial-force measurement of one digital count of axial force is $2(150)/9830 = 0.0305$ lb. The PDP 11/40 data-acquisition computer runs the SWTS data reduction program, which averages measurements over a prescribed sampling time, evaluates calibrations, performs engineering unit conversions, and resolves the measured balance forces into body and wind axis systems.

As part of conversion of the raw balance readings to engineering units, the SWTS program makes "delta-zero," "bias" and "tare" corrections. The purpose for these corrections may be explained by describing the installation procedure. After balance check loads are complete, the bare balance is leveled and the balance gage outputs are recorded as a bare-balance "zero" point. The model is then installed on the balance, the balance is re-leveled, and gage outputs are recorded as a "bias" point. The purpose of the bias point is to record the offset from true balance zero caused by the model in the level condition. The positive and negative loading calibrations of the balance gages often have different slopes, requiring special care in converting balance readings to engineering units. The portion of the applied load that offsets the model weight is evaluated from the negative normal-force calibration, while the remaining load is evaluated from the positive normal-force calibration. This process is illustrated in figure 54. The use of the bias point should not be confused with a "tare," which is used to subtract the model weight from the measured balance forces to obtain the applied aerodynamic load. Once the bias point is recorded, the gage outputs are nulled, which references the model-installed zero point to zero digital counts. Each day before testing begins, the model is leveled and a new zero point is taken. The "delta-zero" between this zero point and the original one is used to compensate for any drift in balance output or signal conditioning.

After the inclinometer is calibrated for angle of attack, two balance tare points are recorded, one point at the highest expected angle of attack, and one point at about half that angle. These tare points are recorded with the model installed, but under wind-off conditions. The model weight is determined from the axial force gage reading at the highest angle of attack, since this is the highest resolution measurement gage. The x- and z- locations of the center of gravity are determined from the forward and aft normal-force gage readings by solving a moment equilibrium equation about the balance reference point at the two angles. The model weight vector computed from this process can be

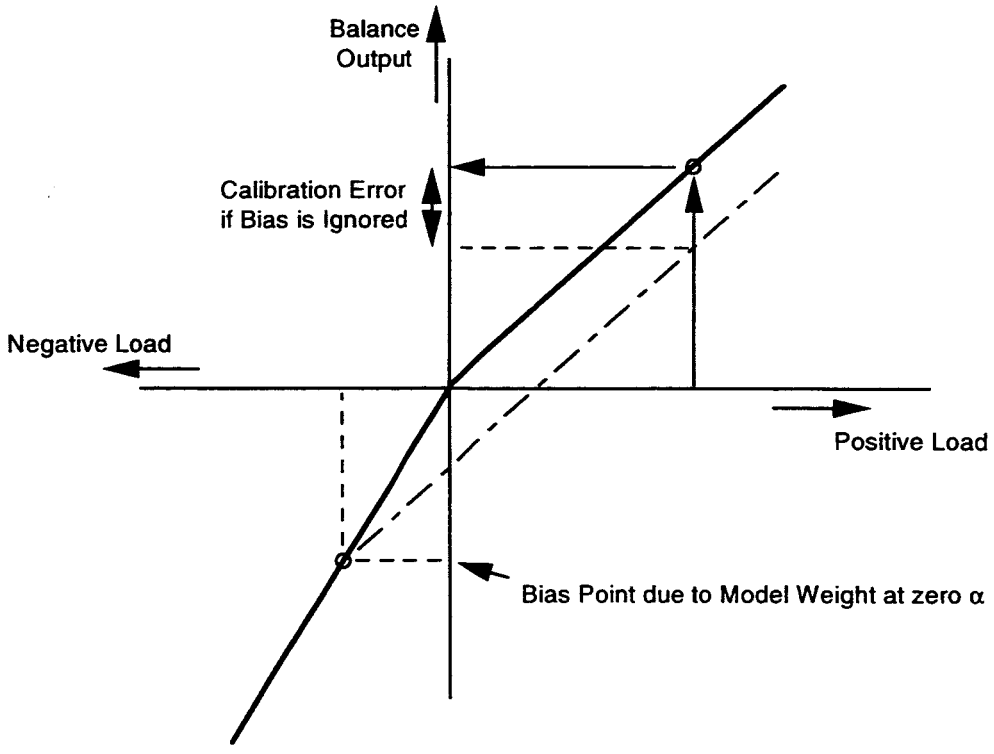

Figure 54. Bi-linear balance calibration.

resolved into components applied to the forward and aft normal-force gages and the axial force gage for any angle of attack, and subtracted from balance readings. The remaining balance forces are the applied aerodynamic loads.

8.7 Test Conditions

The first phase of the test was intended to determine the maximum tunnel speed at which testing could be conducted without exceeding the balance rolling moment capacity. An oscillograph was connected to the unfiltered balance outputs to monitor the dynamic loads experienced by the balance. The split-tip wing model was installed for this portion of the test. The velocity was slowly increased while the balance outputs were monitored. At a velocity of 200 ft/sec (dynamic pressure of 45 psf), the unsteady rolling moments produced by the poor flow quality periodically equaled the balance capacity. Figure 55 shows a sample of the dynamic output of the rolling moment gage recorded by the oscillograph. Based on this result, a dynamic pressure of 45 psf was selected for the entire test program. This value of dynamic pressure produced a Reynolds number of 1.12×10^6 based on the mean aerodynamic chord, and 2.0×10^5 based on the tip chord of the split-tip wing.

Data were taken for both wings over a range of angle of attack from $-4°$ to $9.5°$. The angle of attack was consistently set by approaching from lower angles.

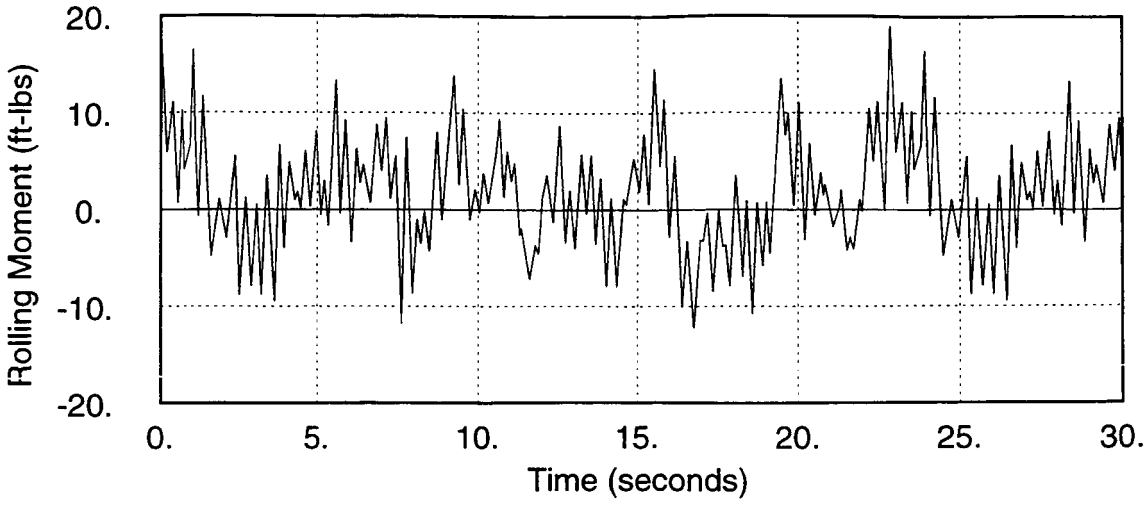

Figure 55. Time history of balance rolling moment output.

Data were taken for both wings with free boundary-layer transition, and with the boundary layer transition fixed at 15 percent chord. The purpose of fixing the boundary layer transition point was to eliminate the possibility of unusual hysteresis in the data resulting from formation of laminar separation bubbles, and to eliminate sensitivity of the drag data to changes in cleanliness or smoothness of the model. The boundary layer trip consisted of a 0.090-in. wide strip of varnish with glass spheres imbedded in the varnish. The glass-sphere diameter used was 0.016 in., determined from the criteria of Braslow (ref. 52).

8.8 Sampling Duration for Data Acquisition

The SWTS data acquisition program allows the researcher to alter the sampling time used to record a data channel during a data point. The analog-digital converter samples each data channel at a frequency of 150 Hz. The sampling duration determines how many individual samples are acquired from each data channel and averaged to record "steady" data values. For typical development wind tunnel tests in modern wind tunnels, a sampling time of 3 sec or less is common. Unfortunately, the poor flow quality of the Ames 7- by 10-Foot Wind Tunnel made short-duration data sampling very inaccurate. The rolling moment history shown in figure 55 is a useful example of how any particular one-second sample could produce an averaged reading significantly different from the true mean value. A test of data repeatability was performed by taking 5 consecutive data points at a fixed angle of attack. With a sampling time of 1 sec, the scatter in the measured drag was 3 percent. Increasing the sampling time to 20 sec made almost no improvement; the scatter was still approximately 3 percent. Figure 56 illustrates how the residual error in averaging an unsteady signal is affected by the sampling duration. For a particular signal wavelength, the excess signal beyond an exact multiple of the wavelength contributes an error in the predicted mean value.

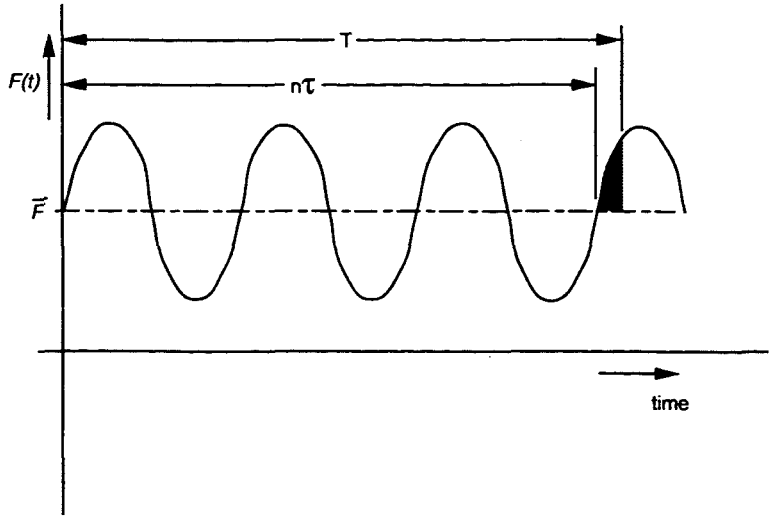

Figure 56. Effect of sampling duration on estimated mean value.

$$\begin{aligned}
\overline{F}_{est} &= \frac{1}{T}\int_0^T F(t)\,dt = \frac{1}{T}\left[\int_0^{n\tau} F(t)\,dt + \int_{n\tau}^{T} F(t)\,dt\right] \\
&= \frac{n\tau}{T}\cdot\frac{1}{n\tau}\int_0^{n\tau} F(t)\,dt + \frac{1}{T}\int_{n\tau}^{T} F(t)\,dt \\
&= \frac{n\tau}{T}\overline{F}_{true} + \frac{1}{T}\int_{n\tau}^{T} F(t)\,dt
\end{aligned} \tag{57}$$

The longer the sample duration, the smaller the residual interval is in relation to the total sampling interval and the smaller the error in the estimated mean value, as shown in equation (57). One criterion often cited is to sample at least 5 cycles of the lowest frequency disturbance that must be averaged out.

Figure 55 suggests that there is a significant disturbance in the flow with a period of about 23 sec. Low frequency variations in the dynamic pressure would not be evident in figure 55, but would also influence the drag measurement. Wadcock reported a ±0.5 percent fluctuation in dynamic pressure with a period corresponding to the "time of flight" around the wind tunnel circuit (ref. 50). For a test-section dynamic pressure of 45 psf, this corresponds to about 20–25 sec. Accurate averaging of the balance signals with these disturbance would require at least 120 sec sample duration!

A test of repeatability was performed again, with a sampling time of 180 sec. The resulting drag repeatability improved to 0.5 percent. While this sampling duration would be considered impractical for most wind tunnel research, the demand for accuracy, and the small number of required test points, enabled the remainder of the test data to be acquired with this sampling duration.

8.9 Estimated Error in Induced Drag from Periodic Rolling Moment

The low frequency swirl characteristic induced considerable periodic rolling moment on the wings, as shown in figure 55. The peak moment equaled the rolling moment capacity of the balance at a dynamic pressure of 45 psf. In the presence of the swirling flow, the wing produces the rolling moment by developing an asymmetrical spanwise lift distribution. This transient spanloading has some influence on the induced drag measured by the balance that would not be present in a steady flow.

To understand the nature of the induced-drag transient, the dynamic rolling-moment history was analyzed to determine its spectral characteristics. The analog trace shown in figure 55 was first digitized, and then fit with a Fourier series. The Fourier analysis indicates that the highest amplitude disturbances have frequencies of 0.22 Hz and 3.0 Hz, with other significant disturbances near 0.13 Hz and at several frequencies between 2.5 Hz and 3.2 Hz, as shown in the plot of amplitude versus frequency, figure 57. The 23 sec period (0.044 Hz) disturbance evident in the analog trace is apparently a "beating" phenomenon from several higher frequency disturbances, since the amplitude of the fundamental frequency in the Fourier analysis is less than 1 ft-lb. The RMS rolling moment from the Fourier series analysis is 7.2 ft-lb.

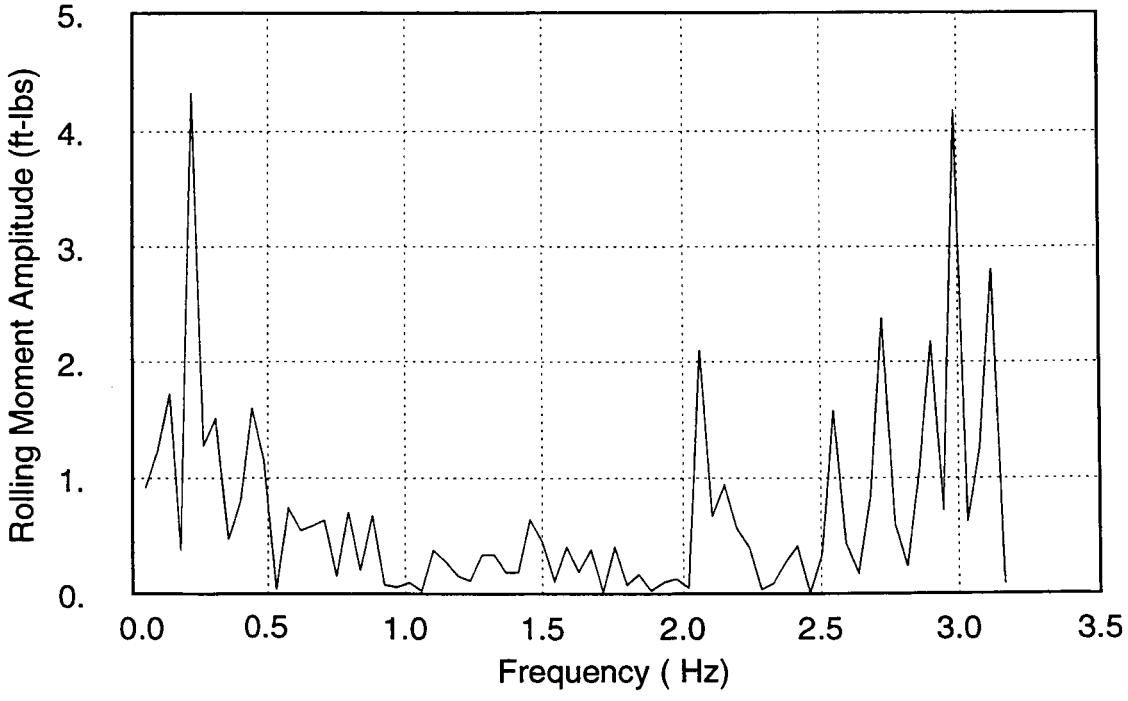

Figure 57. Amplitude spectrum of Fourier-series fit of rolling moment history.

In order to accurately estimate the influence of the unsteady lift distribution on induced drag, a time-accurate unsteady vortex-lattice simulation would be required. For the low-frequency unsteady loading present in this experiment, a quasi-steady analysis was considered acceptable for an estimate of the unsteady drag component. Among the effects neglected by the quasi-steady assumption are the

influences of the varying strength trailing vorticity and spanwise vorticity shed as the loading changes, and the apparent mass. The downwash induced by the unsteady wake contributes to the induced drag differently from the constant strength wake present in the quasi-steady analysis. The reduction in downwash also influences the magnitude of the unsteady component of the lift. Reissner studied the influence of unsteady plunging and flapping motion on the lift response of finite wings (ref. 53). The unsteady sectional lift on a wing is given by

$$\frac{\overline{L}'}{\frac{1}{2}\rho {U_\infty}^2 c} = 2\pi\{-k_o^2 + 2ik_o\overline{P}_{AR}(k_o)\}\frac{\overline{h}}{c} + 2\pi\{\frac{ik_o}{2} + (1+\frac{ik_o}{2})\overline{P}_{AR}(k_o)\}\overline{\alpha} \tag{58}$$

where k_o is the reduced frequency, $\omega c/2U_\infty$, and $\overline{h}$ and $\overline{\alpha}$ are the amplitudes of the plunging and flapping motion. For small values of k_o, this reduces to

$$\frac{\overline{L}'}{\frac{1}{2}\rho {U_\infty}^2 c} = 2\pi\overline{P}_{AR}(k_o)[\overline{\alpha} + 2ik_o\frac{\overline{h}}{c}] \tag{59}$$

The equivalent quasi-steady lift is

$$\frac{\overline{L}'}{\frac{1}{2}\rho {U_\infty}^2 c} = 2\pi(\frac{1}{1+\frac{2}{AR}})[\overline{\alpha} + 2ik_o\frac{\overline{h}}{c}] \tag{60}$$

$\overline{P}_{AR}(k_o)$ corrects the two-dimensional lift curve slope for the induced effects of the finite wing and for the unsteady flow effects. The function $\overline{P}_{AR}(k_o)$ is plotted in figure 58 for an $AR = 6$ elliptical wing.

For this experiment, the highest frequency with significant rolling moment amplitude is about 3 Hz, corresponding to a reduced frequency of $k_o = 0.042$. The amplitude of $\overline{P}_{AR}(k_o)$ from figure 58 for $k_o = 0.042$ is 0.72. The quasi-steady lift curve slope for $AR = 6$ is $0.75 \times 2\pi$. Therefore, for this low frequency, the unsteady lift curve slope is 96 percent of the quasi-steady value. Since the reduced frequency is so low that the lift response is close to the quasi-steady value, it may be inferred that there is little influence from reduced downwash, so that using quasi-steady aerodynamics to compute this small induced-drag transient is adequate.

To estimate the time-averaged induced drag increment associated with this motion, an elliptical wing was modeled with the discrete-vortex method, LinAir, which allows modeling of steady rolling motion (ref. 34). A nondimensional roll rate, $\hat{p} = pb/2U_\infty = 0.011$ input to LinAir was found to produce a rolling moment coefficient, $C_\ell = -0.0048$ or -7.0 ft-lb of rolling moment, corresponding to the RMS moment measured by the force balance. The asymmetrical load distribution resulting from this roll motion is shown in figure 59. The resulting RMS induced drag coefficient was $C_D = -0.00007$. To appreciate the magnitude of this unsteady rolling moment error, it may be compared to typical drag values from the elliptical wing. The measured zero-lift drag coefficient was 0.0085, and the drag coefficient measured at lift coefficients of 0.3 and 0.7 were 0.013 and 0.032, respectively. The RMS drag error is then 0.8 percent of the zero-lift drag, 0.5 percent of the drag at a $C_L = 0.3$, and 0.2 percent of the drag at a $C_L = 0.7$.

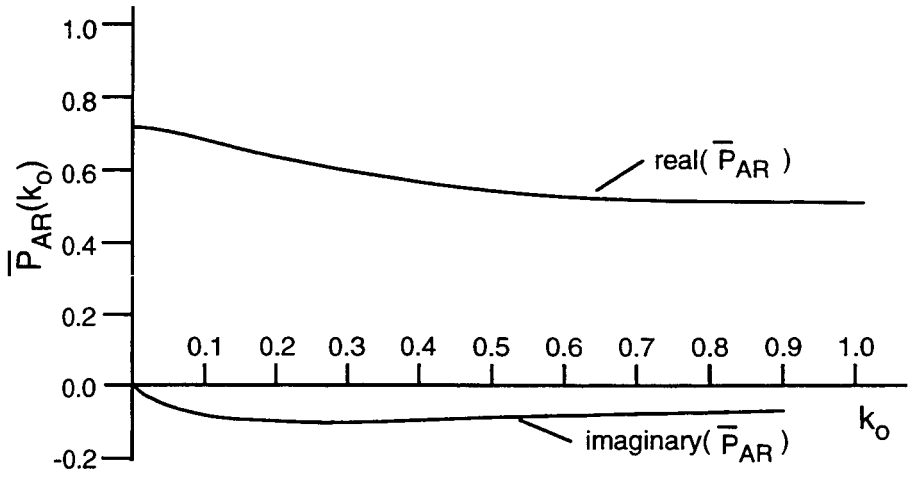

Figure 58. Unsteady lift response to plunging motion, from Reissner (ref.53).

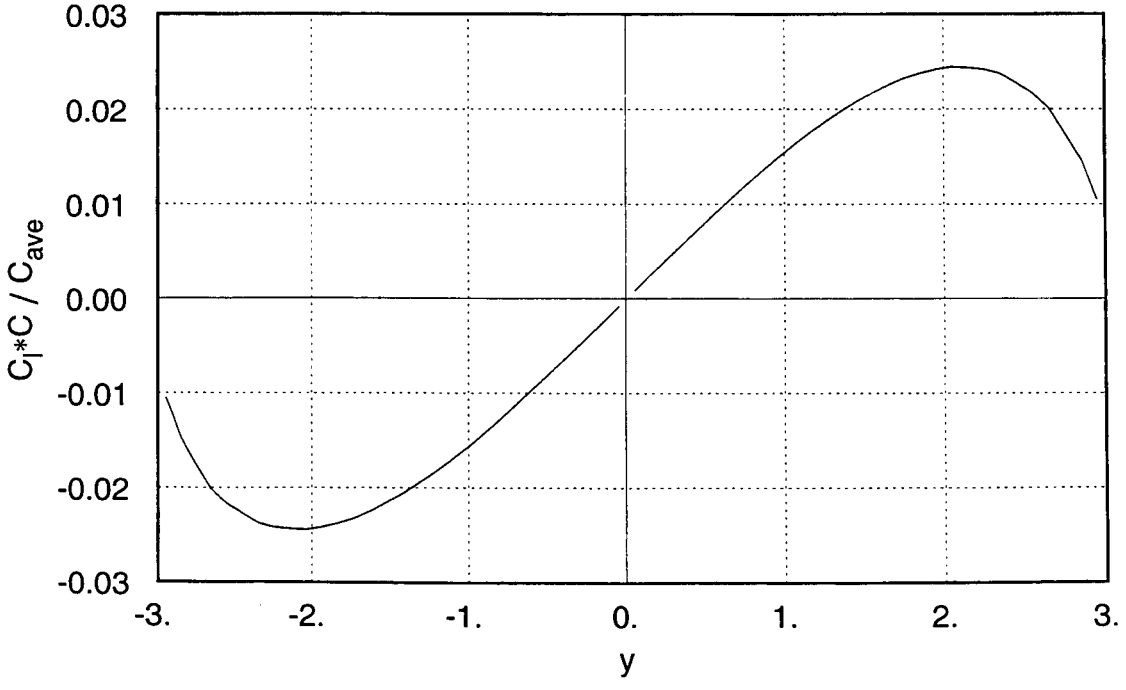

Figure 59. Spanwise lift distribution of elliptical wing from steady roll motion.

It should not be surprising that the induced drag resulting from the roll motion is negative; the effective upwash on the positively loaded wing "tips" the wing resultant force vector forward, and the resultant downwash on the negatively loaded wing also tips the resultant forward. This is, in effect, thrust due to flapping.

8.10 Stream Angle Correction

As shown in section 8.5, the resolution of the balance-measured normal and axial force into drag is extremely sensitive to errors in angle of attack. All angle measurements are made with respect to gravity, using bubble levels or pendulum inclinometers, with the assumption that the flow in the test section is nominally horizontal. The exact angle of the flow with respect to true horizontal, called the stream angle, must be determined to accurately resolve the balance forces into the wind axis forces lift and drag. The most common method of determining the stream angle is to mount the model inverted in the test section and take data at several angles of attack. The stream angle is found by forcing the lift curves from the right-side up and inverted data runs to match. Unfortunately, the model support system used for this experiment did not permit the model to be mounted inverted. However, both models were completely symmetrical to within machining accuracy. This allowed the stream angle to be determined by finding the angle of attack for zero lift. Many data points were taken at angles between $-2°$ and $4°$ for both wings. These data were fit with a line by the method of least-squares, and the stream angle was found by evaluating the line at zero lift. The stream angle for the elliptical wing was found to be $0.43°$ and the stream angle for the split-tip wing was found to be $0.285°$. The fact that the stream angles for the two wings are different was rather alarming at first, since there should be only one value of the stream angle at a given location in the wind tunnel test section. The angle of attack measurements are known to be considerably more accurate than the $0.145°$ difference between the two measured stream angles.

The source of the angle difference is in the orientation of the two models with respect to the balance. The same balance housing was used for both models, and the inclinometer was calibrated with respect to this balance housing. However, the balance housing was fit into a cavity in the underside of each wing. Small manufacturing errors in the orientation of this cavity with respect to the chord plane of each wing produced a slightly different angle of attack for each wing. When this was observed, the two wings were carefully measured on a 3-axis validator at the NASA Ames machine shop. The following process was carried out for each wing. The left- and right-side chord planes were computed from upper and lower surface measurements at three locations on each wing panel. The angular orientation of the balance cavity with respect to each plane was computed, and the two angles were averaged. For the split-tip wing, the average chord plane of the wing was inclined $-0.055°$ with respect to the balance cavity. For the elliptical wing, the inclination was $0.020°$. This accounts for a difference of $0.075°$ in apparent stream angle between the two wings, with the split-tip wing having a smaller stream angle.

This difference is about half the difference in stream angle observed in the experiment. It is likely that there are also small misalignments of the wingtip panels installed on the split-tip wing, although no measurements have been made to substantiate this. The angles involved here are quite small, even by precision machining standards. Any asymmetry in the models resulting from slight manufacturing errors would shift the angle for zero lift slightly, accounting for the remaining difference in stream angle.

For this experiment, the only means for establishing the true stream angle is the technique described above; to align the wings with the flow until there is zero lift, and measure the angle of the balance with respect to gravity. The measured misalignment of the balance cavity with respect to the wings, and other manufacturing asymmetries explain why the measured stream angle is slightly different for the two wings. The stream angles used to correct the data acquired during this experiment were 0.430° for the elliptical wing and 0.285° for the split-tip wing.

8.11 Buoyancy

A well-designed wind tunnel produces a uniform flow in the test section. The walls of the test section must be adjusted to compensate for the growth of boundary layer on the walls. If the walls are not adjusted perfectly, an axial variation of velocity and static pressure will exist in the test section. Wadcock (ref. 50) measured the gradient in static pressure coefficient in the Ames 7- by 10-Foot Wind Tunnel, shown in figure 60. The axial gradient of pressure coefficient is –0.001 ft at the model location. At a dynamic pressure of 45 psf, this corresponds to an axial pressure gradient of $-0.045 \mathrm{lb/ft^3}$.

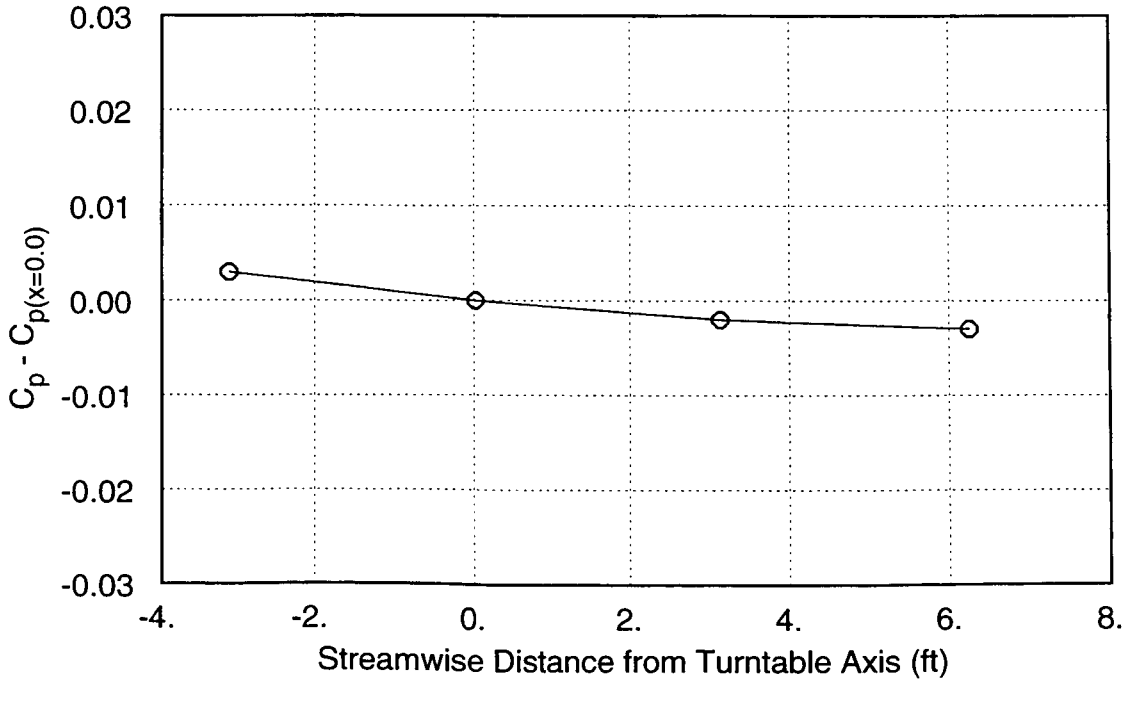

Figure 60. Axial variation of static pressure in Ames 7- by 10-Foot Wind Tunnel (ref. 50).

The axial pressure gradient produces a buoyancy force on the model, proportional to the volume of the model. The volume of the wind tunnel models may be determined from their weight and the known density of aluminum, 173 lb/ft^3. The weight of the elliptical wing is 82 lb, giving a volume of $82/173 = 0.47$ ft^3. The buoyancy force on this model is $0.47 \times 0.045 = 0.021$ lb, which is less than the resolution of the axial force gage of the balance through the analog-digital converter. The buoyancy force is therefore negligible for this experiment.

8.12 Flow Visualization

The split-tip wing has an unusual junction region where the tip surfaces intersect with the main wing surface. An attempt was made to design a junction region that would smoothly blend the surfaces together. However, the width of the zone available to achieve this blending was rather short and there was concern that there would be some degree of flow separation in this region. The oil flow visualization technique was used to study the flow character in this junction region, on the upper surface. Titanium dioxide pigment was added to SAE 30-weight motor oil, and applied to this portion of the upper surface of the wing. The split-tip wing was tested at 8° angle of attack at a dynamic pressure of 45 psf. A photo of the oil-flow pattern in the junction region of the split-tip wing is shown in figure 61.

A small region of flow separation was observed on the blended junction surface, ahead of the leading edge of the aft tip surface. Several other shapes of junction blending were tried, and the shape that seemed to produce the smallest separation region was chosen. Separation zones similar to this are commonly observed at wing-body junctions, where the adverse gradient along the streamlines approaching the leading-edge stagnation point causes the boundary layer on the surface of the body to separate. The separated flow rolls into a vortex which then trails along the upper and lower surface "corners" of the wing-body junction. This flow pattern is often referred to as a "necklace vortex."

8.13 Experimental Results Before Wall Corrections

The results of the testing of the two wings is presented in figures 62 and 63. The lift and drag data presented here were computed with the stream angle corrections applied, but no other corrections to the data were made. The reference quantities used to compute the nondimensional force coefficients are the planform area = 5.4 ft^2, and the corrected test-section dynamic pressure. Figure 62 presents plots of C_L vs α and C_D vs C_L for the elliptical wing. Figure 63 presents the same plots for the split-tip wing. Each plot shows results with free transition, and with transition fixed at 15 percent chord. The free-transition results for the split-tip wing were acquired with 20-sec sampling time, and the poor repeatability of this data is evident.

Also evident is the large increase in profile drag associated with the boundary layer trip. In particular, the drag increase associated with fixing transition on the elliptical wing appears much greater than the drag increase for the split-tip wing. Although it is not clear why this is, it may be

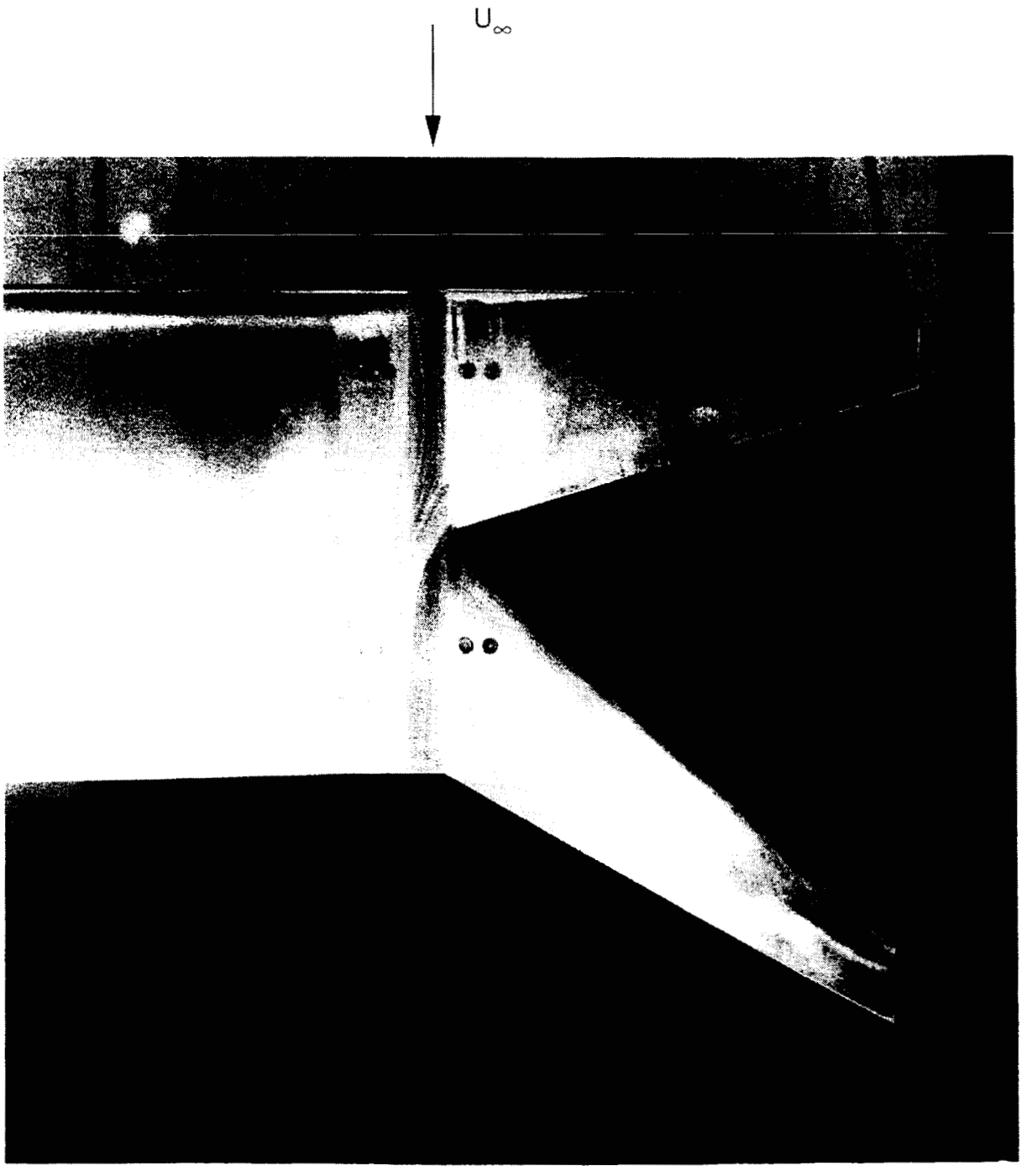

Figure 61. Oil flow visualization of split-tip junction.

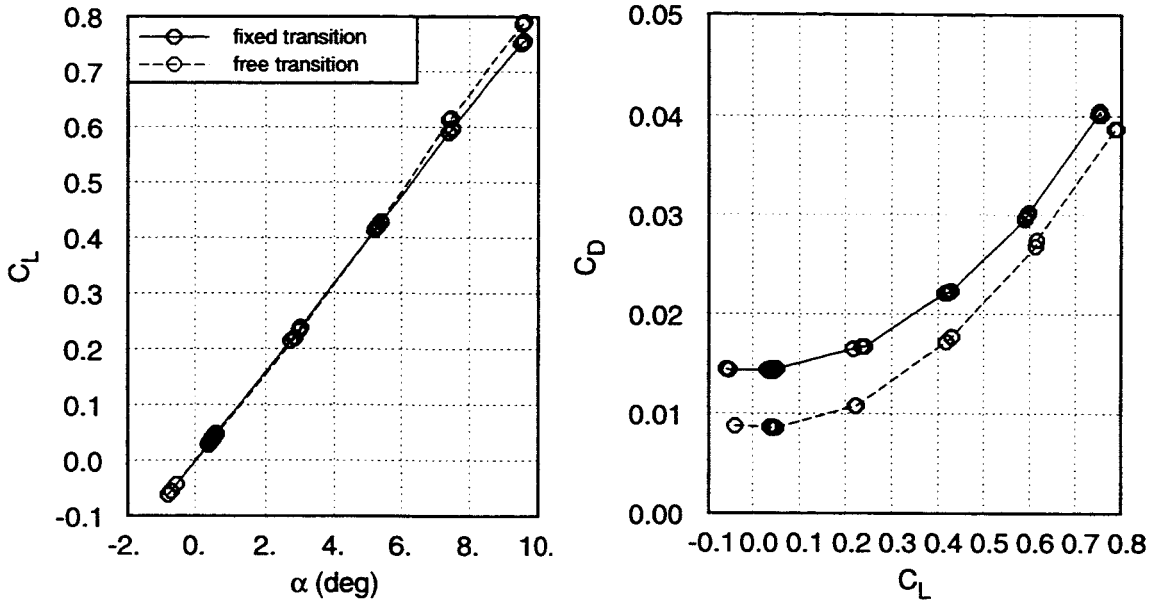

Figure 62. Aerodynamic characteristics of elliptical wing (before wall corrections).

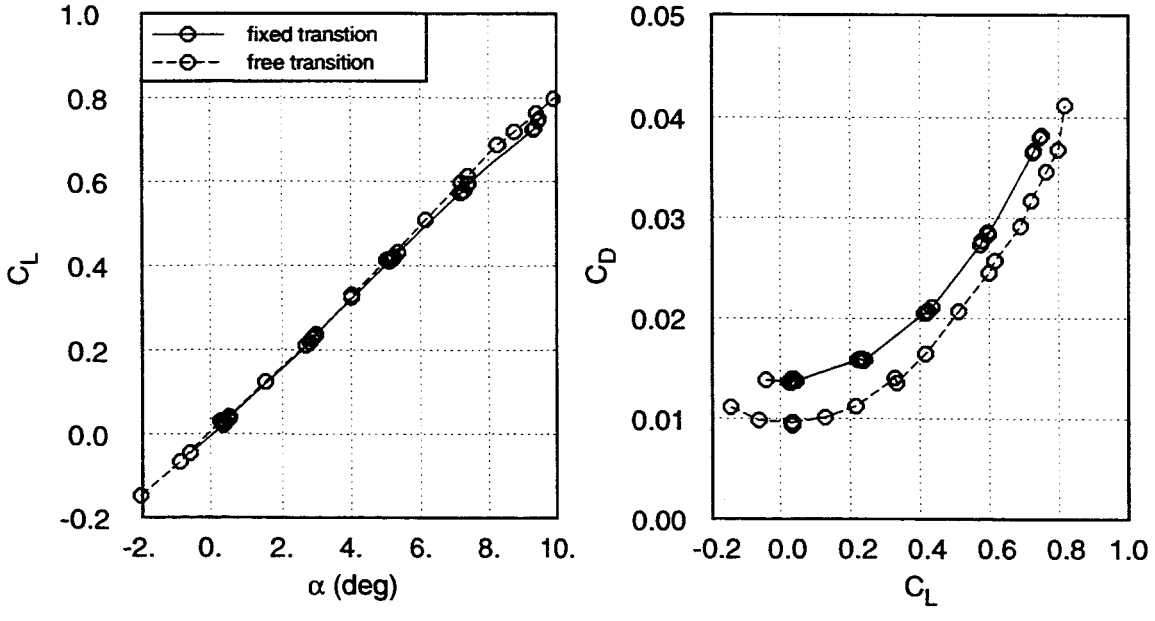

Figure 63. Aerodynamic characteristics of split-tip wing (before wall corrections).

that the split-tip wing with free transition already had areas where no laminar flow occurred because of disturbances at the junction region where the tip surfaces attached. The elliptical wing may have suffered more from the fixed transition because it supported more laminar flow initially.

8.14 Wall Corrections

The presence of the wind tunnel walls modifies the flow over a model compared with the flow that would exist if the model could be tested in free air. The influence of the walls may be visualized by representing the lifting wing model and its trailing wake as a horseshoe vortex, and the presence of the tunnel walls by an image vortex system. The image vortices on the left and right sides induce upwash on the wing, while the image vortices above and below the wing induce sidewash velocities that cancel. The induced upwash from the image vortex system increases the lift and reduces the drag at a fixed geometric angle of attack.

Wall-effects corrections have traditionally been computed directly from the image vortex model described above. Assuming the strength of the lifting vortex is fixed, an increment in induced drag is computed from the Kutta-Joukowski law; $\delta D = \rho \delta w \Gamma$, where δw is the increment in downwash from the image vortices. An adjustment to the angle of attack is computed as $\delta \alpha = \delta w / U_\infty$. In practice, these corrections are typically computed with vortex distributions that are representative of the wing spanload distribution.

With the development of panel methods to solve for the potential flow about arbitrary configurations, it is now possible to compute more precise wall corrections by modeling the wing in the wind tunnel. The A502 high-order panel code was used to compute wall corrections for this experiment. Computation of the wall corrections involves solutions for the lift and drag at several angles of attack, with and without the presence of the walls. The wind tunnel was modeled as a long tube with a 7 ft by 10 ft cross section, extending 6 wingspans upstream and 12 wingspans downstream. The tube was made long so that local inlet and exit flow conditions would not influence the test section flow. The model support strut was also modeled to include any interference effect of the support system on the model. Figure 64 shows the panel model of the elliptical wing in the wind tunnel.

The wind tunnel walls were modeled with doublet-only panels with a boundary condition of zero normal mass flux. The model support was modeled by source and doublet panels with the same implicit Morino boundary condition used to model the wings. With one exception for the split-tip wing, a streamwise wake model was used for the wing wakes. A wake was also attached to the downstream edge of the wind tunnel tube, although this had no influence on the computed results. As an expedience, the trailing wake from the forward tip surface of the split-tip wing was abutted directly to the leading edge of the aft tip surface, as shown in figure 65. This directs the vorticity shed from the forward tip to combine with the vorticity from the aft tip, so all the vorticity is shed into a single trailing wake, and results in a loss of the nonplanar character of the split-tip wake. The same wake model was used for

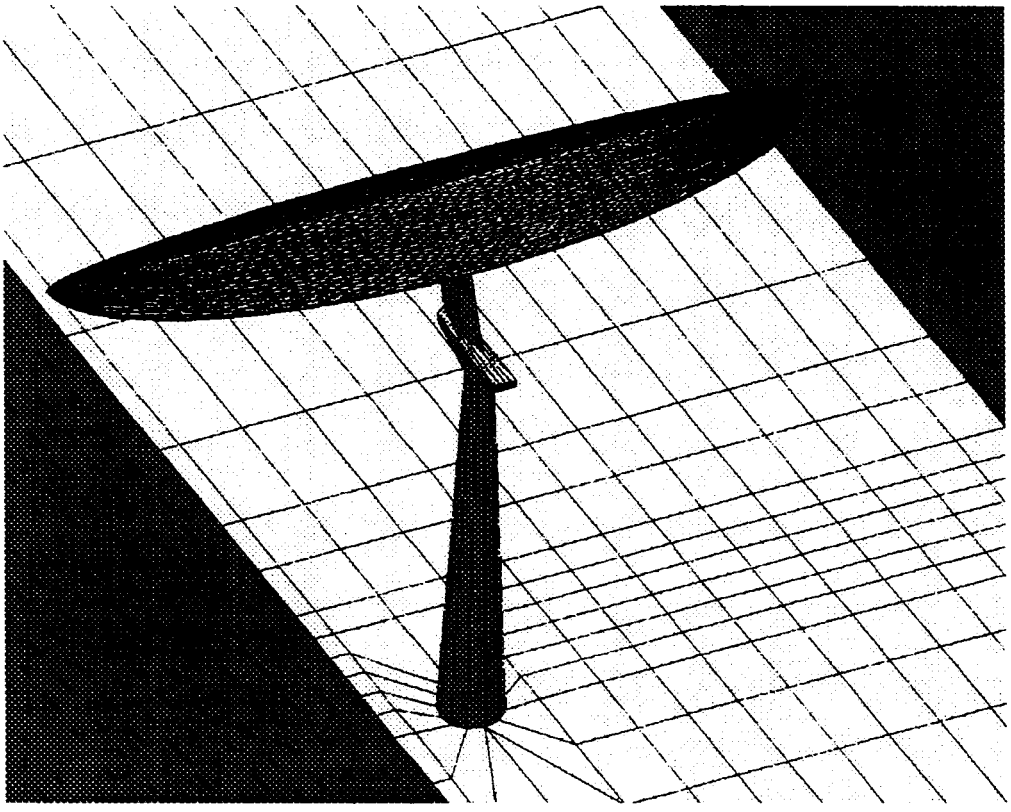

Figure 64. Panel model of elliptical wing on model support in Ames 7- by 10-Foot Wind Tunnel.

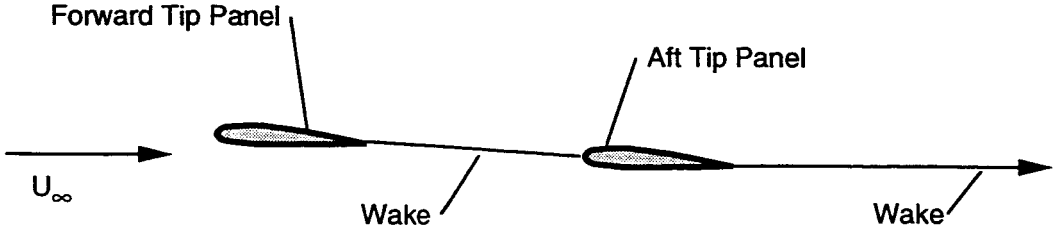

Figure 65. Wake model used for wall-effects computations on split-tip wing.

both the free-air and in-tunnel solutions. Computations on the split-tip wing in free air indicate that the span efficiency is reduced to 0.99 with this wake model, while the spanwise lift distribution is not affected significantly. As described in section 7, construction of a streamwise wake for the forward tip surface involves carefully deforming the wake to avoid impingement on the aft surface. This process would have to be repeated for each angle of attack. For the purposes of computing increments in lift and drag due to the presence of the walls, this change in wake shape was not considered significant; The upwash induced by the image vortex system would not be changed significantly by the small vertical displacement of the forward tip vortex.

A502 solutions for both wings, with and without the presence of the walls and model support, were obtained for $-2°, 0°, 2°, 4°, 6°, 8°$ angle of attack. The lift was determined by surface-pressure integration, while the drag was determined by Trefftz-plane integration, using the technique described in section 3. Additional solutions at 0° and 8° angle of attack was obtained with the tunnel walls, but without the model support strut. These results indicated that the model support interference produced a significant pitching moment influence, a small influence on the lift, and no influence on the induced drag. The wall effects corrections computed here and applied to the experimental results include the influence of the model support strut. A flow survey point was located in the computational model of the wind tunnel at the axial location where test section static pressure is measured in the real wind tunnel. The dynamic pressure at this point in the tunnel (in the computational model) matched the free-air dynamic pressure within 0.1 percent, so no correction to the force coefficients for "tunnel calibration" was made.

For each angle of attack, the increments in lift and drag between the free-air and in-tunnel solutions were determined. These results are shown in figure 66 for both the elliptical and split-tip wings. Second-order polynomials were fit to the C_L-increment data, and fourth-order polynomials were fit through the C_D-increment data. Wall-effects corrections were applied to the wind tunnel results by evaluating the polynomials at the the specific angle of attack for each data point. The resulting increments were added to the lift and drag coefficients to produce corrected coefficients equivalent to experimental measurements in free air. The wind tunnel data were taken at angles of attack up to about 9.5°, while the wall-effects computations were limited to 8°. Generally, it is a poor practice to rely on a polynomial-fit to extrapolate beyond the points used to create the fit, but in this case the trend in the wall corrections is well-behaved, as evident in figure 66, and this was considered an acceptable expedience.

The wingspan of these models is only 60 percent of the test section width, so tunnel wall effects were not expected to be large. However, examination of the increments shown in figure 66 indicate that the corrections are significant. For example, the elliptical wing at 8° angle of attack produced a C_L of 0.640 and a C_D of 0.0320. The wall correction for C_L is –0.04, or –6.25 percent, and the wall correction for C_D is 0.0020, also 6.25 percent. This results in a correction to L/D of 13 percent.

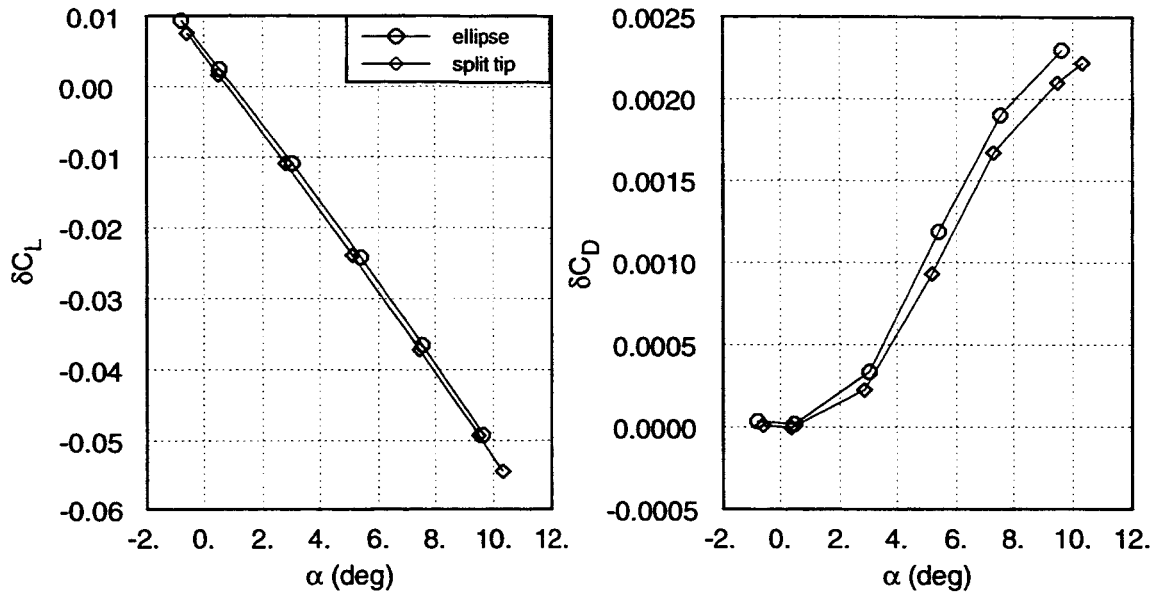

Figure 66. Wall-effects corrections for the elliptical and split-tip wings.

8.15 Experimental Results After Wall Corrections

The experimental results with the wall-effects corrections applied are presented in figures 67 through figure 70. The data are presented in the same format as the results presented in section 8.13. A comparison of the L/D of the elliptical and split-tip wings with fixed transition is shown in figure 71. These data indicate that the split-tip wing achieves an L/D almost 5 percent greater than the elliptical wing. This result is consistent with the difference in induced drag predicted in section 7 by computational methods, assuming that about half the total drag is induced drag and that the viscous drag is about the same for both wings. A more detailed decomposition of the experimentally measured drag is performed in the remaining sections of this section.

8.16 Estimation of Viscous Drag

In order to determine the induced drag from these experimental results, the viscous drag must be estimated. Assuming that the flow over the majority of the wing area is reasonably two-dimensional, it would seem straightforward to integrate the viscous drag predicted from two-dimensional airfoil section data. The spanwise distribution of lift coefficient can be predicted from the panel method, and the local Reynolds number at each span station is easily computed from the local chord and the test conditions. The wing planform may be divided into strips in the stream direction, and the viscous drag on each strip can be estimated from the two-dimensional section data at the appropriate lift coefficient and Reynolds number. The total viscous drag resulting from summing the contributions from all the strips is then nondimensionalized by the reference area.

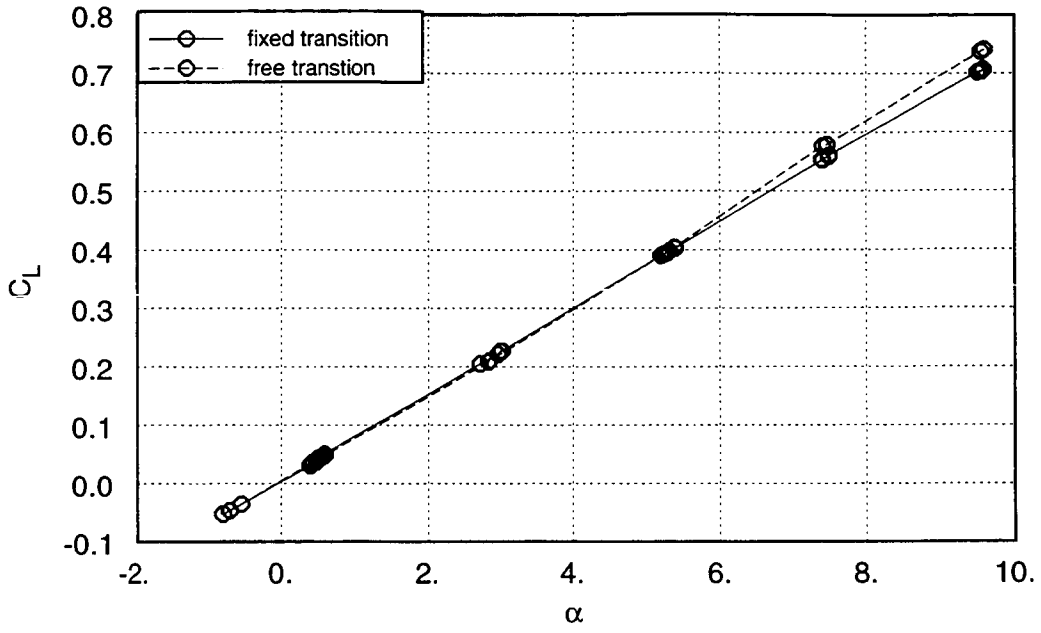

Figure 67. C_L versus α for the elliptical wing.

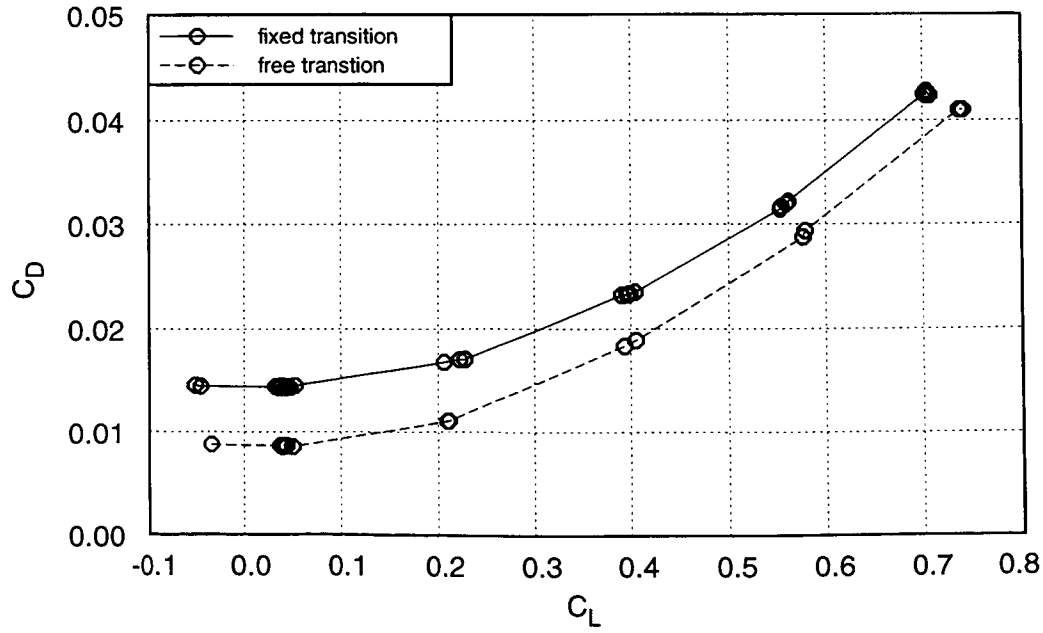

Figure 68. C_D versus C_L for the elliptical wing.

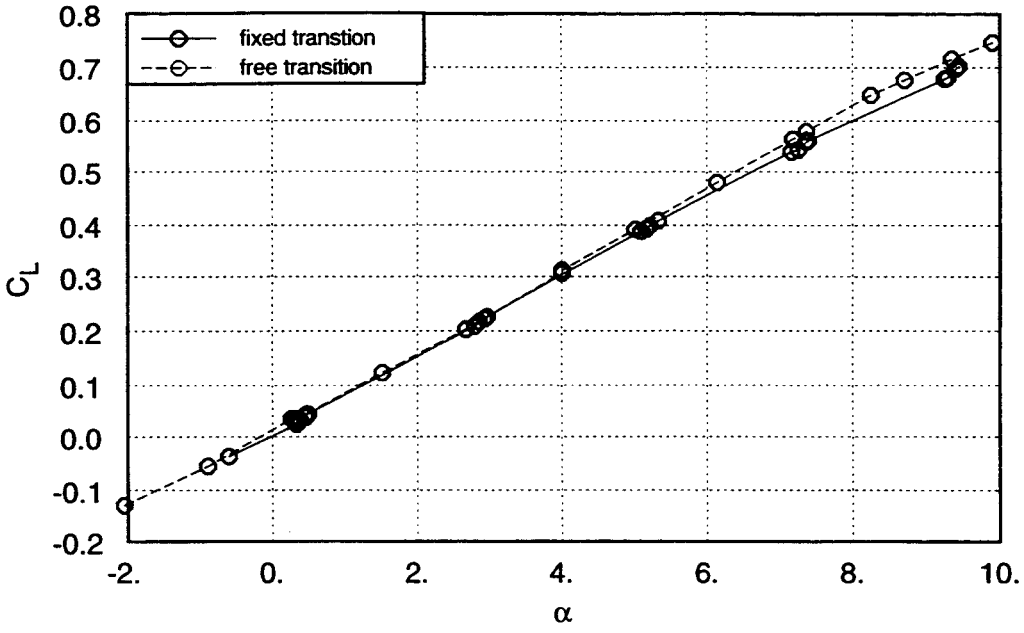

Figure 69. C_L versus α for the split-tip wing.

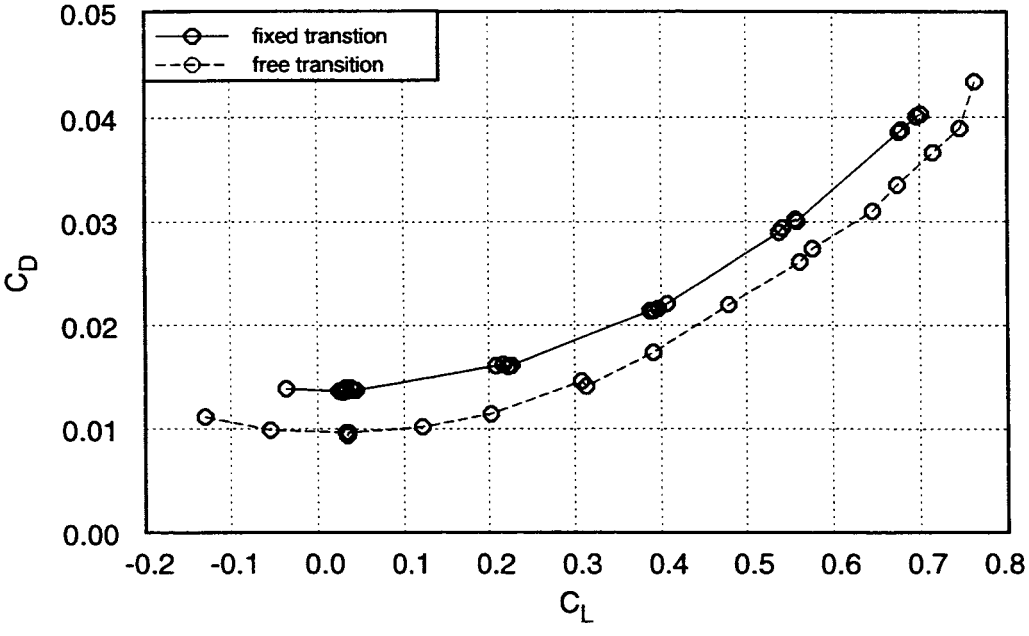

Figure 70. C_D versus C_L for the split-tip wing.

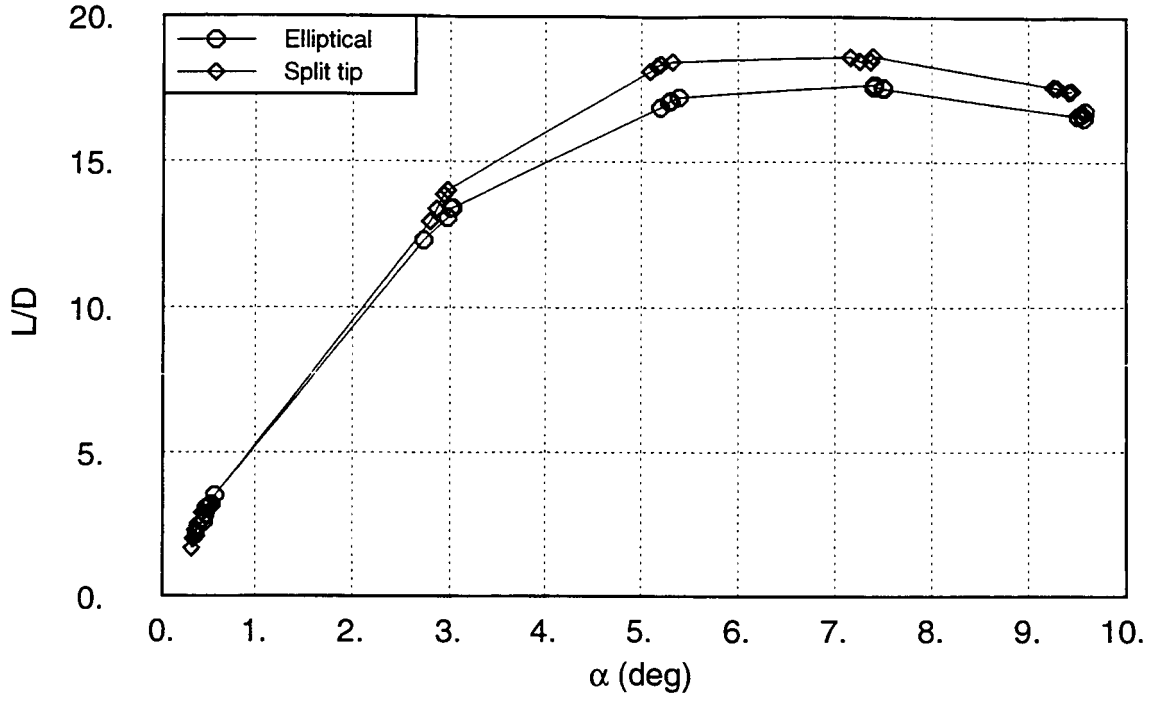

Figure 71. L/D versus α for the elliptical and split-tip wings.

A number of difficulties make this process less straightforward than it may seem. First, comprehensive two-dimensional experimental data for the NACA 0012 airfoil at Reynolds numbers below 1.0×10^6 are rather scarce. The only suitable source found is reported by Sheldahl and Klimas (ref. 54), for experiments performed to obtain data for wind turbines. Although the authors claim to have made stream-angle corrections, the drag polars published in reference 54 indicate the characteristic asymmetry of test results with substantial stream angle.

Second, the wind tunnels used for two-dimensional airfoil testing typically have excellent flow quality. Section data acquired with free boundary-layer transition often exhibit considerable extent of laminar flow. The same transition locations are not attainable in the Ames 7- by 10-Foot Wind Tunnel at the same test conditions, because of high turbulence intensity levels, as high as 1.0 percent (ref. 50).

Third, for the experimental data acquired with the boundary layer trip installed, there was significant drag associated with the trip itself, independent of the loss of laminar boundary layer. This "grit-drag" was especially large in this experiment because of the large grit-size required to cause transition at the wingtips, where the Reynolds number was very low. For the higher Reynolds number flow on the center area of the wing, this grit size was large enough to protrude well above the boundary layer.

The first of these problems was overcome by averaging the two-dimensional data from positive and negative angles of attack, approximately correcting the data for stream angle. Adjusted drag polars

for the NACA 0012 airfoil were extracted from reference 54 for lift coefficients from 0.0 to 1.0, over a range of Reynolds numbers from 2.0×10^5 to 1.75×10^6.

To resolve the second problem, a computational airfoil analysis program was used to estimate the effect of the tunnel turbulence on transition location. The program used, called PANDA (ref. 55), solves for the pressure distribution about an airfoil by a modified thin airfoil theory with second-order corrections. The boundary layer transition location is estimated by Michel's method. The boundary-layer properties are predicted by the integral methods of Thwaites and Head for the laminar and turbulent portions, respectively. The viscous drag is estimated from the Squire-Young formula. A complete discussion of the theory used by PANDA is presented by Kroo (ref. 55).

The NACA 0012 airfoil was first analyzed with PANDA over a range of lift coefficients from 0.0 to 1.0, at a Reynolds number of 4.0×10^6 to approximate the effect of the high turbulence intensity in promoting transition. The locations of transition on the upper and lower surface were noted for each case. Next, the airfoil was re-analyzed, at the same lift coefficients, over the same Reynolds numbers as the 2-D experimental data, but with transition fixed at the locations corresponding to the high Reynolds number. For ease of discussion, these results are referred to as early-transition results. Finally, PANDA was used to analyze the airfoil at the experimental Reynolds numbers allowing free transition. The drag increment between the free transition case and early-transition case was determined for each Reynolds number and lift coefficient, and this increment was added to the experimentally determined section properties from Sheldahl and Klimas (ref. 54). Through this process, an estimate of the free-transition viscous drag polars at several Reynolds numbers in the Ames 7- by 10-Foot Wind Tunnel was developed. These polars are shown in figure 72.

These polars were then used in the strip integration procedure described above to estimate the viscous drag polars of the elliptical and split-tip wings. The drag at zero lift estimated by this method was then compared with the drag at zero lift measured in the wind tunnel. For the elliptical wing, the increment in drag coefficient between the viscous drag estimate and the experiment was 0.00025. For the split-tip wing, the increment was 0.00079. The viscous drag prediction is expected to be somewhat low, due to additional sources of drag on the models such as surface roughness and viscous interference drag from the model support. On the split-tip wing, the transition area where the tip surfaces intersect the main wing surface is a region of highly three-dimensional flow, with a small region of flow separation. It is reasonable to expect that additional drag would be produced in this region that would not be predicted by the strip integration, so the under-prediction of drag would be greater for the split tip. These small drag increments were added to the viscous drag polars for the two wings, essentially shifting the viscous polars slightly to match the experimental measurements at zero lift. The estimated viscous drag polars for the elliptical and split-tip wings are shown in figure 73.

The procedure described above was repeated to account for the influence of fixed transition on the wings. PANDA was used to find the increments in drag between free transition and transition fixed at 0.15 percent chord over the same range of Reynolds numbers. These increments were added to the

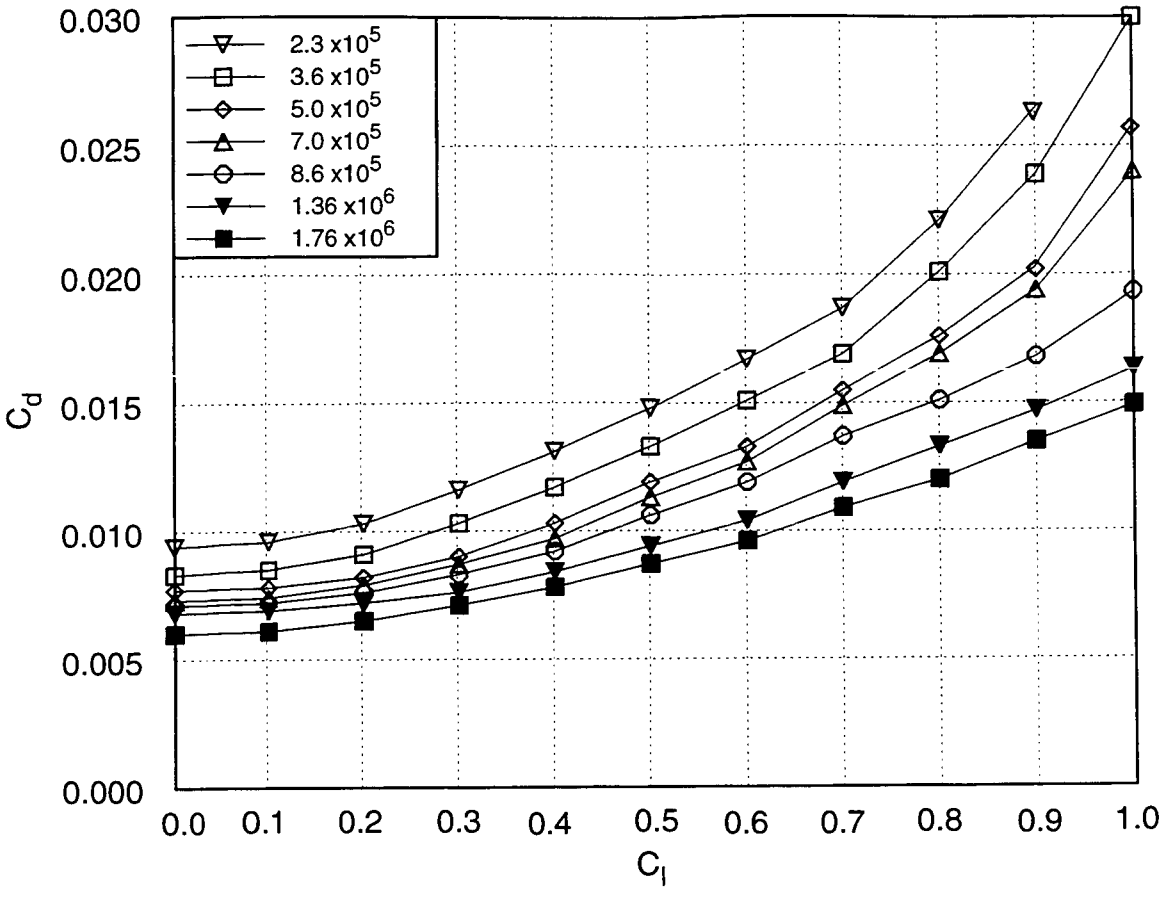

Figure 72. 2-D section polars for NACA 0012.

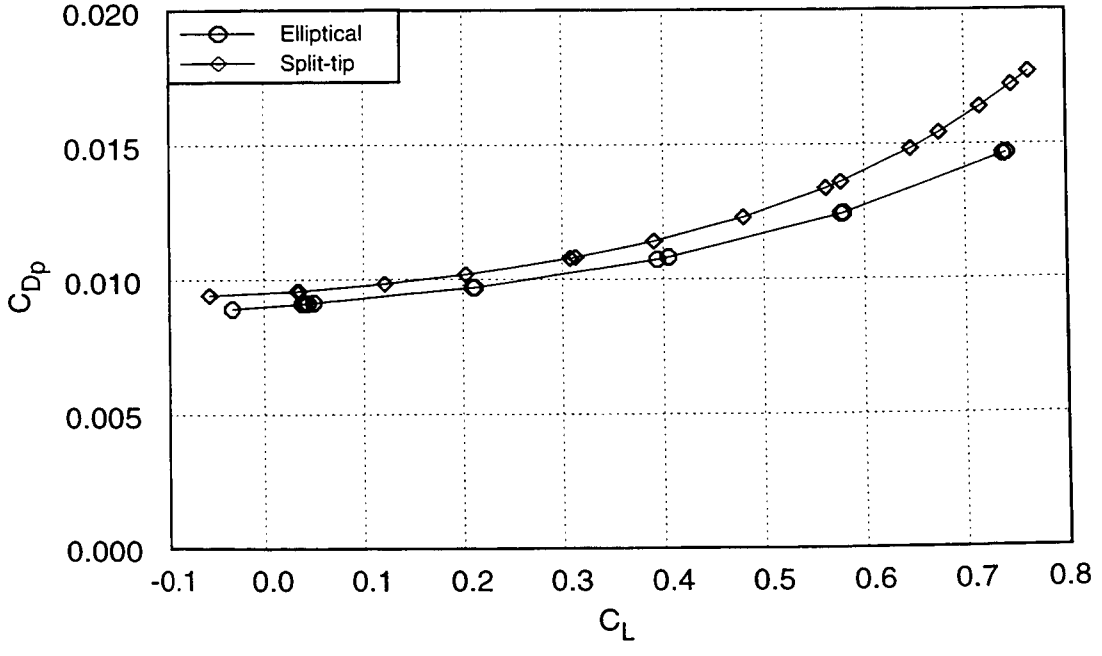

Figure 73. Viscous polars with free transition for the elliptical and split-tip wings.

airfoil polars to estimate the fixed-transition polars of the airfoil. The fixed-transition polars were used in the strip-integration process to estimate the viscous polars of the two wings. The drag at zero lift predicted by these polars was also compared with the drag at zero lift measured in the wind tunnel for the two wings. The resulting drag increments were significantly larger for these fixed-transition cases than was found for the free transition cases. This is at least partly due to the drag on the boundary-layer trip itself. For the elliptical wing, the increment in drag coefficient was 0.0039, and for the split-tip wing, the increment was 0.0029. It is not clear whether it is reasonable to add these large increments to the viscous polars, simply shifting the polars to match the experiment at zero lift, since it is not known how the drag from the boundary-layer trip or other sources would vary with lift coefficient. However, without additional evidence as a guide, the viscous polars were shifted to match the measured drag at zero lift. The estimated viscous drag polars for the elliptical and split-tip wings with fixed transition are shown in figure 74.

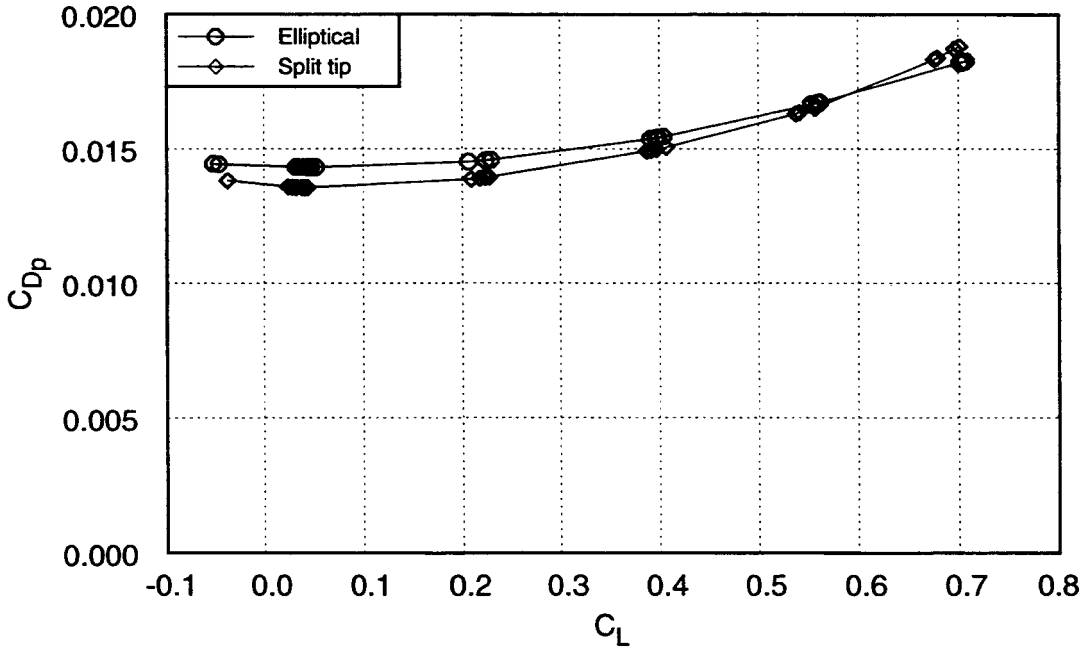

Figure 74. Viscous polars with fixed transition for the elliptical and split-tip wings.

Given the sequence of assumptions and approximations made to arrive at these viscous polars, they must be regarded as estimates. The estimate of viscous drag is clearly the least accurate element of determining span efficiency from experimental force data. Since the viscous polar was shifted to match the measured drag at zero lift, there is presumably no error at zero lift. At high lift coefficients, the estimated viscous drag could have considerable errors, accumulated from the adjustment to account for early or fixed transition, and from the applied shift in the polar to match the experiment. The error could conceivably be as large as the applied shift, about 20 percent of the estimate at $C_L = 0.7$. However, it should also be noted that whatever absolute (or bias) error exists in these viscous polars,

it is likely to be similar for both wings. Estimates of the increment in viscous drag between the two wings are likely to be much better. The difference in applied shifts of the polars for the two wings is one possible source of relative error between the two polars. This difference was about 5 percent of the estimated viscous drag at $C_L = 0.7$. Therefore, the uncertainty in the *relative* viscous drag between the two wings is estimated to be about 5 percent.

8.17 Span Efficiency

For each experimental data point, the induced drag was determined by subtracting the estimated viscous drag from the experimental drag coefficient (with wall-effects corrections). The span efficiency was then calculated from $e = C_L^2/\pi AR C_{D_i}$. The accumulation of uncertainties in the calculation of the span efficiency is illustrated by evaluating the differential of the span efficiency for a typical case. For $e = C_L^2/\pi AR(C_{D_{total}} - C_{D_p})$ the differential of the span efficiency is

$$\delta e = \frac{2C_L \delta C_L (C_{D_{total}} - C_{D_p}) - C_L^2(\delta C_{D_{total}} - \delta C_{D_p})}{\pi AR(C_{D_{total}} - C_{D_p})^2} \tag{61}$$

The absolute uncertainty in span efficiency is estimated by substituting estimates of the individual uncertainties. Assuming the uncertainty in C_L is 1 percent, the uncertainty in C_D is 2 percent, and the uncertainty in C_{D_p} is 10 percent, for typical values of $C_L = 0.7$, $C_D = 0.038$, $C_{D_p} = 0.015$, the differentials are $\delta C_L = 0.007$, $\delta C_D = 0.00076$, $\delta C_{D_p} = 0.0015$. Substituting these values into equation (61) gives $\delta e = 0.121$ or 12 percent of $e = 1.0$. Once again, this uncertainty is a measure of absolute accuracy—the uncertainty in the relative span efficiency is much better. The repeatability in C_L is 0.25 percent, and the repeatability in C_D is 0.5 percent. Assuming the relative uncertainty in C_{D_p} is 5 percent, then the relative uncertainty in the span efficiency from equation (61) becomes $\delta e = 0.06$ or 6 percent of $e = 1.0$. The estimated span efficiency is plotted in figure 75 versus angle of attack for both the elliptical and split-tip wings. The experimental uncertainty in determining span efficiency is evident in the large degree of scatter in the results in figure 75. The span efficiency of the elliptical wing is approximately 0.98 and the span efficiency of the split-tip wing is approximately 1.10. Despite the large experimental uncertainty in these results, the estimates agree remarkably well with the span efficiencies predicted computationally in sections 6 and 7.

8.18 A Wake Survey Method for Experimental Drag Decomposition

The method of Shoemaker (ref. 24) provides an alternative method of determining span efficiency of finite wings during wind tunnel tests. The foundation of this method is a control-volume energy balance similar to the momentum balance developed in section 3. A viscous flow is assumed, so that the skin-friction drag appears as a deficit in total pressure in the far-field wake. At the same time, the vorticity is computed from velocities in the wake region. A seven-hole cone probe is used to survey the total pressure and three components of velocity in the wake region downstream of a wind tunnel

model. High-resolution surveys of the wake downstream of both the elliptical and split-tip wings were made in a plane two chord lengths downstream of the wings as part of these wind tunnel experiments. A detailed description of these surveys and the data reduction procedure to determine the viscous drag and induced drag components is contained in reference 24. A summary of the results of the surveys performed at 9° angle of attack is provided in table 12. The values of span efficiency predicted from the wake surveys are plotted on figure 75 along with the results of the viscous-drag estimation. The experimental uncertainty of the induced drag and profile drag results were estimated by Shoemaker to be approximately 2 percent and 5 percent respectively. The computational and experimental predictions of span efficiency in this study agree with the wake survey predictions within Shoemaker's expected uncertainty.

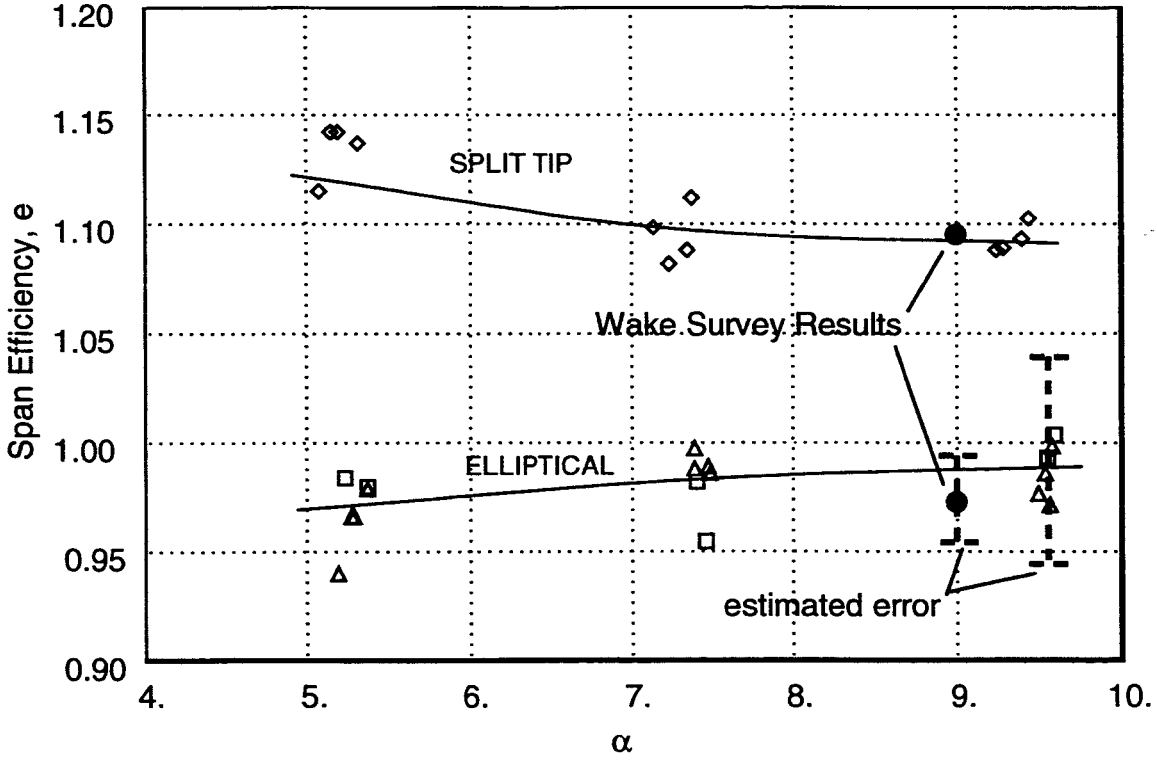

Figure 75. Experimental estimate of span efficiency for the elliptical and split-tip wings.

Table 12. Results of drag decomposition from experimental wake surveys (ref.24)

Wing	α	C_L	C_{D_i}	e	C_{D_p}	$C_{D_{total}}$
Elliptical	9°	0.714	0.02004	0.972	0.01876	0.0388
Split-tip	9°	0.726	0.01827	1.096	0.01965	0.0379

Figure 76 shows a comparison between the force-free wake model from section 7 and results from the experimental wake survey of the split-tip wing at 9° angle of attack. The experimental results are plotted in the form of contours of total pressure, indicating the loss of total pressure in the viscous wake. The small region of separated flow associated with the necklace vortex at the junction fairing (see section 8.12) is evident as a region of total pressure deficit. This separation appears to have some affect on the location and shape of the junction between the trailing wakes from the two tip panels. This effect was not modeled by the potential-flow wake relaxation. The model support also influenced the wake shape somewhat near plane of symmetry. A survey of wake velocities for the panel solution with the model support and tunnel walls modeled indicates that this small effect would be modeled if the wake shape had been computed in the presence of the strut. Other than these two discrepancies, the agreement between the computed and experimental wake shapes is quite good.

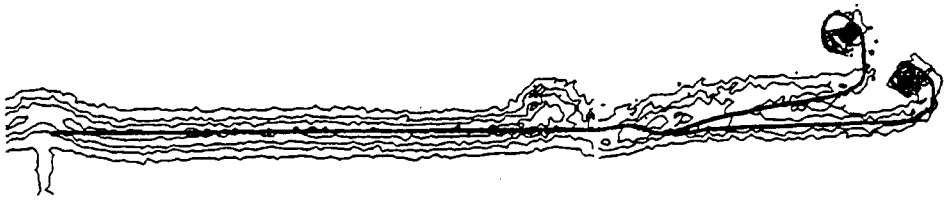

Figure 76. Computed and measured wake shape downstream of split-tip wing.

9 SUMMARY AND CONCLUSIONS

9.1 Summary

During the course of studying nonlinear aspects of induced drag, the induced drag characteristics of a variety of wing planforms have been determined computationally and experimentally. The computational results were obtained by Trefftz-plane integration of wake properties found by a high-order panel method. The influence of the force-free trailing wake compared with the more traditional model of a wake trailing straight in the freestream direction was studied for two elliptical wings. One wing has a straight 25 percent chordline, while the other has a straight trailing edge, referred to here as a crescent wing. The induced drag of the crescent wing was about 2 percent less than the elliptical wing, due to a more nearly elliptical spanwise lift distribution. For the crescent wing, the wake model had almost no effect, changing the predicted drag by less than 0.25 percent. When the effect of the force-free wake was ignored for the elliptical wing, the computed drag was reduced by 1.5 percent. The greater influence of the force-free wake on the elliptical wing is a nonlinear effect that occurs because the tip shape allows the initial roll-up potion of the wake to interact more closely with the bound vorticity on the wing. A planar split-tip wing was designed to exaggerate this nonlinear effect to produce significant drag savings. The planar split-tip wing produces a highly nonplanar wake as the angle of attack is increased. Even with the classical streamwise wake, the computed induced drag for the split-tip wing was 6 percent less than an elliptically loaded planar wing with the same span and total lift. When an accurate force-free wake was included, the computed drag was reduced by an additional 6 percent.

Experimental results were obtained for the split-tip wing and the elliptical wing from wind tunnel tests, by subtracting an estimate of the viscous drag from the total measured drag, and from a survey of wake properties downstream of the wing models. Although the experimental uncertainty of both techniques was rather high (about 5 percent), both techniques indicated approximately 12 percent lower induced drag for the split-tip, consistent with the computational results.

Many of the important numerical results presented in this paper are values of span efficiency measured or computed for specific configurations and flow conditions. These results are easily lost among the many pages of description of the methods used to obtain them. A summary is included in figure 77 to provide a useful reference of the major computational and experimental results of this work.

9.2 Conclusions

This work focused on two nonlinear aspects of induced drag of finite wings. The influence of correctly modeling the force-free wake on the predicted induced drag has been demonstrated computationally and experimentally. The influence of compressibility introduced by the full potential equations on the span loading and induced drag of a modern transport wing has also been studied. Analytical methods

Computational Results Summary–Effects of Wake Model
(Mach no.=0.01, A502 solutions)

Planform	Angle of Attack	Streamwise Wake C_L	Streamwise Wake e	Force-Free Wake C_L	Force-Free Wake e
X_t=0.25 Elliptical	4°	0.304	0.985	0.300	0.959
X_t=1.00 Crescent	4°	0.307	0.991	0.306	0.992
Split-Tip (AR=6.67)	9°	0.765	1.048	0.761	1.113

Computational Results Summary–Effects of Mach Number
(X_t=1.00 Crescent, Streamwise Wake, α=5.0°, Tranair solutions)

Mach no.	C_L	e
0.01	0.428	1.006
0.5	0.478	1.009
0.6	0.512	1.011
0.7	0.569	1.002

Experimental Results Summary
($\alpha \cong 9°$)

Planform (AR=6.67)	Force-Balance C_L	Force-Balance e	Wake Survey C_L	Wake Survey e
Xt=0.25 Elliptical	0.7	0.98	0.714	0.972
Split-Tip Wing	0.7	1.10	0.726	1.096

Figure 77. Summary of results.

and computational tools have been developed for accurate prediction of induced drag that account for these nonlinear effects. The most significant contributions of this work are summarized below.

A rigorous analytical framework has been established for determining the extent of force-free wake that must be modeled. The error associated with replacing the force-free wake with a streamwise wake downstream of a near-field partition is negligible provided the partition is oriented perpendicular to the freestream. The error associated with the traditional engineering approach, with complete substitution of a streamwise wake, is potentially an order of magnitude larger, depending on wing planform. Munk's stagger theorem, which states that the longitudinal arrangement of the bound vortex system does not affect the induced drag, relies on the streamwise wake model. This work has demonstrated that the longitudinal arrangement, coupled with the vertical displacement from the angle of attack, can affect the induced drag by promoting a high degree of nonplanar character in the near wake.

A novel method was developed for computing the force-free wake shape. This hybrid wake-relaxation scheme couples the well-behaved nature of the discrete vortex wake with viscous-core modeling and the high-accuracy velocity prediction of the high-order panel method. Trefftz-plane drag results were found to be highly sensitive to wake shape, and the hybrid scheme provided converged wake shapes that allowed accurate Trefftz-plane integration.

Two concepts were studied for exploiting nonlinear wake interaction to reduce induced drag. Both concepts involve the development of a highly nonplanar wake from a planar wing. The first concept relied on flow separation along the side edge of the wingtip to produce a highly nonplanar wake. Unfortunately, the induced velocities from the near wake made it difficult to achieve the optimal lift distribution, which required greater than elliptical loading on the tip region. The second concept used an unusual split-tip configuration to produce a highly nonplanar wake shape and promote significant interaction between the trailing and bound vortex systems. Although completely planar, this wing design produced significantly less induced drag than the classical elliptical wing. With a traditional streamwise wake model, the induced drag of the split-tip wing was predicted to be 6 percent less than the elliptical wing. With a force-free wake generated by the hybrid wake scheme, the predicted induced drag was 12 percent less than the elliptical wing. The performance of the split-tip wing was confirmed by experiment. Careful tests were performed on models of an elliptical wing and the split-tip wing with equal span and area. Induced drag was determined from the force measurements by subtracting an estimate of the viscous drag, and from an analytical drag- decomposition method using velocities measured by surveying the wake with a seven-hole cone probe. Although the experimental uncertainty of both experimental techniques was about 5 percent, the experimental results confirm the computational prediction—the split-tip wing has about 12 percent higher span efficiency than the elliptical wing at a lift coefficient of 0.7.

The practical use of Trefftz plane drag integration was extended to transonic flow with the Tranair full-potential code. The induced drag characteristics of a typical transonic transport wing were studied with both Tranair and A502, a high-order linear panel method. Changes in spanwise lift distribution

and span efficiency beyond those predicted by the Prandtl-Glauert equation were found to be significant enough to suggest that the wing spanwise lift distribution must be adjusted during design with the full-potential method, to assure that the desired span loading is obtained.

APPENDIX

2ND ORDER ACCURATE APPROXIMATION OF THE COMPRESSIBLE BERNOULLI EQUATION

From the First Law of Thermodynamics for steady flow of a calorically perfect gas,

$$C_pT + \frac{V^2}{2} = \text{constant} \tag{62}$$

or

$$\frac{\gamma}{\gamma-1}\frac{P}{\rho} + \frac{V^2}{2} = \text{constant} \tag{63}$$

Therefore,

$$\frac{\gamma}{\gamma-1}\frac{P}{\rho} + \frac{V^2}{2} = \frac{\gamma}{\gamma-1}\frac{P_\infty}{\rho_\infty} + \frac{{U_\infty}^2}{2} \tag{64}$$

or

$$\frac{\gamma}{\gamma-1}\left(\frac{P}{\rho} - \frac{P_\infty}{\rho_\infty}\right) = \left(\frac{{U_\infty}^2}{2} - \frac{V^2}{2}\right) \tag{65}$$

For isentropic flow,

$$\frac{1}{\rho_\infty}\left(\frac{P}{P_\infty}\right)^{-\frac{1}{\gamma}} = \frac{1}{\rho} \tag{66}$$

Substituting equation 66 into equation 65 and rearranging, and noting that $\frac{1}{2}\rho_\infty {U_\infty}^2 = \frac{1}{2}\gamma P_\infty {M_\infty}^2$,

$$\frac{P}{P_\infty} = \left[\frac{\gamma-1}{2}{M_\infty}^2\left(1 - \frac{V^2}{{U_\infty}^2}\right) + 1\right]^{\frac{\gamma}{\gamma-1}} \tag{67}$$

For small perturbations in velocity with respect to the freestream, a binomial expansion of $\frac{P}{P_\infty}$ may be written from

$$(1+\epsilon)^{\frac{\gamma}{\gamma-1}} = 1 + \frac{\gamma}{\gamma-1}\epsilon + \frac{1}{2}\frac{\gamma}{(\gamma-1)^2}\epsilon^2 + \text{higher order terms} \tag{68}$$

Substituting $\epsilon = \frac{\gamma-1}{2}{M_\infty}^2\left(1 - \frac{V^2}{{U_\infty}^2}\right) = \frac{\gamma-1}{2}\frac{{M_\infty}^2}{{U_\infty}^2}\Big(-(u^2+v^2+w^2) - 2uU_\infty\Big)$ and $\epsilon^2 = \frac{(\gamma-1)^2{M_\infty}^4}{4{U_\infty}^4}\Big(4u^2{U_\infty}^2 + \text{higher order terms}\Big)$,

$$\frac{P}{P_\infty} = 1 + \frac{\gamma}{2}\frac{{M_\infty}^2}{{U_\infty}^2}\Big(-2uU_\infty - ((1-{M_\infty}^2)u^2 + v^2 + w^2)\Big) \tag{69}$$

Finally, $P - P_\infty = P_\infty(\frac{P}{P_\infty} - 1)$ so

$$P - P_\infty = \frac{1}{2}\rho_\infty\Big(-2uU_\infty - ((1-{M_\infty}^2)u^2 + v^2 + w^2)\Big) \tag{70}$$

REFERENCES

1. Zimmer, H.: The Aerodynamic Optimization of Wings in the Subsonic Speed Range and the Influence of the Design of the Wingtips. Dr-ing. Dissertation, University of Stuttgart, Stuttgart, Germany, 1983.
2. Lowson, M. V.: Minimum Induced Drag for Wings with Spanwise Camber. J. Aircraft, vol. 27, July 1990, pp. 627–631.
3. Van Dam, C. P.:Induced-Drag Characteristics of Crescent-Moon-Shaped Wings. J. Aircraft, vol. 24, Feb. 1987, pp. 115–119.
4. Smith, S. C.; and Kroo, I. M.: A Closer Look at the Induced Drag of Crescent-Shaped Wings. AIAA Paper 90-3063, presented at AIAA 8th Applied Aerodynamics Conference, Portland, Oreg., Aug. 1990.
5. DeHaan, M. A.: Induced Drag of Wings with Highly Swept and Tapered Wing Tips. AIAA Paper 90-3062, presented at AIAA 8th Applied Aerodynamics Conference, Portland, Oreg., Aug. 1990.
6. Smith, S. C.; and Kroo, I. M.: Computation of Induced Drag for Elliptical and Crescent-Shaped Wing. J. Aircraft, vol. 30, July–Aug. 1993, pp. 446–452.
7. Kroo, I. M.; and Smith, S. C.: Computation of Induced Drag with Nonplanar and Deformed Wakes. SAE Paper 901933, SAE Transactions, presented at SAE Aerotech-90, Long Beach, Calif., Sept. 1990.
8. Cone, C. D.: The Theory of Induced Lift and Minimum Induced Drag of Nonplanar Lifting Systems. NASA TR 139, 1962.
9. Committee on Aeronautical Technologies, Aeronautics and Space Engineering Board, Commission on Engineering and Technical Systems, National Research Council. Aeronautical Technologies for the Twenty-First Century. National Academy Press, Washington D.C., 1992.
10. Wittenberg, K. R.; Reichenbach, S. H.; Kao, T. J.; and Tinoco, E. N.: CFD Wake and Flowfield Predictions. AIAA Paper 87-2618, presented at AIAA 5th Applied Aerodynamics Conference, Monterey, Calif., Aug. 1987.
11. Letcher, J. S., Jr.: Convergence of Lift and Drag Predictions by a Morino Panel Method (VSAERO). J. Aircraft, vol. 27, Aug. 1989, pp. 1019–1020.
12. Towne, M. C.; Strande, S. M.; Erickson, L. L.; Kroo, I. M.; Enomoto, F. Y.; Carmichael, R. L.; and McPherson, K. F.: Panair Modeling Studies. AIAA Paper 83-1830, presented at AIAA Applied Aerodynamics Conference, Danvers, Mass., July 1983.
13. Lanchester, F. W.: Aerodynamics. London: Constable and Co., Ltd., 1907.
14. Prandtl, L.: Tragflugeltheorie. Gottinger Nachrichten, Mathemisch—Physikalische Klasse, pp. 451–477, 1918.
15. Prandtl, L.: Application of Modern Hydrodynamics to Aeronautics. NACA Report 116, 1921.

16. Munk, M. M.: The Minimum Induced Drag of Aerofoils. NACA Report 121, 1921.
17. Trefftz, E.: Prandtlsche Tragflachen-und Propeller-Theorien. Z. Angew Math. Mech., vol. 1, 1921, p. 206.
18. Glauert, H.: Elements of Airfoil and Airscrew Theory. Cambridge: Cambridge Univ. Press, 1926.
19. Katz, J.; and Plotkin, A.: Low Speed Aerodynamics—From Wing Theory to Panel Methods. McGraw-Hill, 1991.
20. Karman, T.; and Burgers, J. M.: General Aerodynamic Theory—Perfect Fluids. in Aerodynamic Theory (Durand, W. F., ed.), vol. II, 1934.
21. Kuchemann, D.: The Aerodynamic Design of Aircraft. Pergamon Press, 1978.
22. Maskell, E. C.: Progress Towards a Method for the Measurement of the Components of the Drag of a Wing of Finite Span. RAE Technical Report 72232, Royal Aircraft Establishment, Farnborough, England, Jan. 1973.
23. Wu, J. C.; Hackett, J. E.; and Lilley, D. E.: A Generalized Wake-Integral Approach for Drag Decomposition in Three-Dimensional Flows. AIAA Paper 793-0279, presented at AIAA 17th Aerosciences Meeting, New Orleans, La., Jan. 1979.
24. Shoemaker, W. C.: A Wake Integral Method for Experimental Drag Measurement and Decomposition. Ph.D. Dissertation, Department of Aeronautics and Astronautics, Stanford University, Stanford, Calif., Aug. 1994.
25. Betz, A.: Behavior of Vortex Systems. NACA TM-713, 1932.
26. Spreiter, J. R.; and Sacks, A. H.: The Rolling Up of the Trailing Vortex Sheet and Its Effect on the Downwash Behind Wings. J. Aeronautical Sciences, vol. 18, Jan. 1951, pp. 21–32.
27. Mittelman, Z.: Prediction of Unsteady Aerodynamics and Control of Delta Wings with Tangential Leading Edge Blowing. Ph.D Dissertation, SUDDAR 580, Department of Aeronautics and Astronautics, Stanford University, 1989.
28. Quackenbush, T. R.; Bliss, D. B.; Wachspress, D. A.; and Ong, C. C.: Free Wake Analysis of Hover Performance Using a New Influence Coefficient Method. NASA CR-4150, 1988.
29. Lamb, H.: Hydrodynamics. Dover, 6th ed., 1945.
30. Ramachandran, K.; Tung, C.; and Caradonna, F. X.: The Free-Wake Prediction of Rotor Hover Performance Using a Vortex-Embedding Method. AIAA Paper 89-0638, presented at AIAA 27th Aerospace Sciences Meeting and Exhibit, Reno, Nev., Jan. 1989.
31. Nagati, M. G.; Iverson, J. D.; and Vogel, J. M.: Vortex Sheet Modeling with Curved Higher-Order Panels. J. Aircraft, vol. 24, Nov. 1987, pp. 776–781.
32. Ribeiro, R. S.: Analysis of Wing Wake Roll-Up Using a Vortex-In-Cell Method. Ph.D. Dissertation, Department of Aeronautics and Astronautics, Stanford University, Stanford, Calif., May 1992.
33. Lamar, J. E.: A Modified Multhopp Approach for Predicting Lifting Surface Pressures and Camber Shape for Composite Planforms in Subsonic Flow. NASA TN D-4427, July 1968.
34. Kroo, I. M.: Linair for the Macintosh. Stanford, Calif.: Desktop Aeronautics, 1987.

35. Maskew, B.: Prediction of Subsonic Aerodynamic Characteristics—A Case for Low-Order Panel Methods. J. Aircraft, vol. 19, Feb. 1982, pp. 157–163.

36. Ashby, D. L.; Dudley, M. R.; and Iguchi, S. K.: Development and Validation of an Advanced Low-Order Panel Method. NASA TM-101024, Oct. 1988.

37. Carmichael, R. L.; and Erickson, L. L.: PANAIR—A higher Order Panel Code for Predicting Subsonic or Supersonic Linear Potential Flows About Arbitrary Configurations. AIAA Paper 81-1255, presented at AIAA 14th Fluid and Plasma Dynamics Conference, Palo Alto, Calif., June 1981.

38. Epton, M. A.; and Magnus, A. E.: PANAIR—A Computer Program for Predicting Subsonic or Supersonic Linear Potential Flows About Arbitrary Configurations Using a Higher Order Panel Method—Theory Document. NASA CR-3251 (rev. 1), Mar. 1990.

39. Johnson, F. T.; Samant, S. S.; Bieterman, M. B.; Melvin, R. G.; Young, D.; Bussoletti, J. E.; and Hilmes, C. L.: Tranair: A Full-Potential, Solution-Adaptive, Rectangular Grid Code for Predicting Subsonic, Transonic, and Supersonic Flows About Arbitrary Configurations—Theory Document. NASA CR-4348, Dec. 1992.

40. Johnson, F. T.; Samant, S. S.; Bieterman, M. B.; Melvin, R. G.; Young, D.; Bussoletti, J. E.; and Hilmes, C. L.: Tranair: A Full-Potential, Solution-Adaptive, Rectangular Grid Code for Predicting Subsonic, Transonic, and Supersonic Flows About Arbitrary Configurations—User's Manual. NASA CR-4349, Dec. 1992.

41. Shevell, R. S.: Fundamentals of Flight. Prentice-Hall, 2nd ed., 1983.

42. Steger, J. L.; and Baldwin, B. S.: Shock Waves and Drag in the Numerical Calculation of Isentropic Transonic Flow. NASA TN-D-6997, Oct. 1972.

43. Henne, P. A.; and Hicks, R. M.: Wing Analysis Using a Transonic Potential Flow Computational Method. NASA TM-78464, 1978.

44. van der Vooren, J.; and Sloof, J. W.: CFD-Based Drag Prediction; State-of-the- Art, Theory, Prospects. TP-90247 L, NLR, 1990.

45. Burkett, C. W.: Reductions in Induced Drag of Wings with Highly Swept and Tapered Wing Tips. Aeronautical J., vol. 93, pp. 400–405, Dec. 1989.

46. Chow, J. S.; Zilliac, G. G.; and Bradshaw, P.: Measurements in the Near-Field of a Turbulent Wingtip Vortex. AIAA Paper 93-0551, presented at AIAA 31st Aerosciences Meeting and Exhibit, Reno, Nev., Jan. 1993.

47. Srinivasan, G. R.; McCroskey, W. J.; Bader, J. D.; and Edwards, T. A.: Numerical Simulation of Tip Vortices of Wings in Subsonic and Transonic Flows. J. Aircraft, vol. 26, Oct. 1988, pp. 1153–1162.

48. Ma, E.: Effect of Wing Tip Strakes on Wing Lift-Drag Ratio. J. Aircraft, vol. 26, May 1989, pp. 410–416.

49. Kroo, I. M.: A General Approach to Multiple Lifting Surface Design and Analysis. AIAA Paper 84-2507, presented at AIAA/AHS/ASEE Aircraft Design, Systems, and Operations Meeting, San Diego, Calif., Oct. 1984.

50. Wadcock, A.: The NASA Ames 7 Ft x 10 Ft Wind Tunnel—Present Flow Quality and Recommendations for Improvement. Analytical Methods Report 8705, Analytical Methods, Inc., Redmond, Wash., July 1987. Submitted to NASA Ames Research Center as final report under NAS2-11945.

51. Smith, S. C.; and Stonum, R. K.: Experimental Aerodynamic Characteristics of a Joined-Wing Research Aircraft Configuration. NASA TM-101083, Apr. 1989.

52. Braslow, A. L.; and Knox, E. C.: Simplified Method for Determination of Critical Height of Distributed Roughness Particles for Boundary Layer Transition at Mach Numbers from 0 to 5. NACA TN-4363, Aug. 1958.

53. Reissner, E.; and Stevens, J. E.: Effect of Finite Span on the Airload Distributions for Oscillating Wings II—Methods of Calculation and Examples of Application. NACA TN-1195, Oct. 1947.

54. Sheldahl, R. E.; and Klimas, P. C.: Aerodynamic Characteristics of Seven Symmetrical Airfoil Sections Through 180–Degree Angle of Attack for Use in Aerodynamic Analysis of Vertical Axis Wind Turbines. Sandia Laboratory Report SAND80-2114, Sandia National Laboratories, Albuquerque, N. Mex., Mar. 1981.

55. Kroo, I. M.: PANDA—A Program for Analysis and Design of Airfoils. Stanford, Calif.: Desktop Aeronautics, 1987.

REPORT DOCUMENTATION PAGE

Form Approved
OMB No. 0704-0188

1. AGENCY USE ONLY *(Leave blank)*	2. REPORT DATE	3. REPORT TYPE AND DATES COVERED
	February 1996	Technical Paper

4. TITLE AND SUBTITLE

A Computational and Experimental Study of Nonlinear Aspects of Induced Drag

5. FUNDING NUMBERS

505-59-10

6. AUTHOR(S)

Stephen C. Smith

7. PERFORMING ORGANIZATION NAME(S) AND ADDRESS(ES)

Ames Research Center
Moffett Field, CA 94035-1000

8. PERFORMING ORGANIZATION REPORT NUMBER

A-960804

9. SPONSORING/MONITORING AGENCY NAME(S) AND ADDRESS(ES)

National Aeronautics and Space Administration
Washington, DC 20546-0001

10. SPONSORING/MONITORING AGENCY REPORT NUMBER

NASA TP-3598

11. SUPPLEMENTARY NOTES

Point of Contact: Stephen C. Smith, Ames Research Center, MS 227-6, Moffett Field, CA 94035-1000; (415) 604-5856

12a. DISTRIBUTION/AVAILABILITY STATEMENT

Unclassified-Unlimited
Subject Category – 02

12b. DISTRIBUTION CODE

13. ABSTRACT *(Maximum 200 words)*

Despite the 80-year history of classical wing theory, considerable research has recently been directed toward planform and wake effects on induced drag. Nonlinear interactions between the trailing wake and the wing offer the possibility of reducing drag. The nonlinear effect of compressibility on induced drag characteristics may also influence wing design. This thesis deals with the prediction of these nonlinear aspects of induced drag and ways to exploit them. A potential benefit of only a few percent of the drag represents a large fuel savings for the world's commercial transport fleet.

Computational methods must be applied carefully to obtain accurate induced drag predictions. Trefftz-plane drag integration is far more reliable than surface pressure integration, but is very sensitive to the accuracy of the force-free wake model.

The practical use of Trefftz plane drag integration was extended to transonic flow with the Tranair full-potential code. The induced drag characteristics of a typical transport wing were studied with Tranair, a full-potential method, and A502, a high-order linear panel method to investigate changes in lift distribution and span efficiency due to compressibility.

Modeling the force-free wake is a nonlinear problem, even when the flow governing equation is linear. A novel method was developed for computing the force-free wake shape. This hybrid wake-relaxation scheme couples the well-behaved nature of the discrete vortex wake with viscous-core modeling and the high-accuracy velocity prediction of the high-order panel method. The hybrid scheme produced converged wake shapes that allowed accurate Trefftz-plane integration. An unusual split-tip wing concept was studied for exploiting nonlinear wake interaction to reduced induced drag. This design exhibits significant nonlinear interactions between the wing and wake that produced a 12% reduction in induced drag compared to an equivalent elliptical wing at a lift coefficient of 0.7.

The performance of the split-tip wing was also investigated by wing tunnel experiments. Induced drag was determined from force measurements by subtracting the estimated viscous drag, and from an analytical drag-decomposition method using a wake survey. The experimental results confirm the computational prediction.

14. SUBJECT TERMS	15. NUMBER OF PAGES
Induced drag, Wake roll-up, Wing tips	129
	16. PRICE CODE: A07

17. SECURITY CLASSIFICATION OF REPORT	18. SECURITY CLASSIFICATION OF THIS PAGE	19. SECURITY CLASSIFICATION OF ABSTRACT	20. LIMITATION OF ABSTRACT
Unclassified	Unclassified		